



Paolo Campiglio

Growth and Magnetism of Patterned Atomic and Molecular Nanostructures

School of Nanostructures and Nanotechnologies
Università degli Studi di Milano-Bicocca
School of Condensed Matter and Interfaces
Université Paris Diderot - Paris 7

Supervisors:
Adele Sassella
Sylvie Rousset

13 January 2011

Contents

Contents	3
General introduction	7
1 Engineering metallic and molecular nanostructures at surfaces	11
1.1 Top-down approaches	12
1.1.1 Photolithography and scanning beam lithography . . .	12
1.1.2 Molding, embossing and printing	13
1.1.3 Scanning probe lithography	14
1.2 Bottom-up approaches	15
1.2.1 Generality of nucleation and aggregation	16
1.2.2 Metal self-organization	18
1.2.2.1 Homogeneous growth on flat and anisotropic surfaces	18
1.2.2.2 Heterogeneous growth on template surfaces . .	20
1.2.3 Molecular self-organization	22
1.2.3.1 Supramolecular architectures	22
1.2.3.2 Self-assembled monolayers	23
1.3 Conclusions	24
2 Magnetism of metallic and molecular nanostructures	25
2.1 Introduction to nanomagnetism	25
2.1.1 Energetics of a ferromagnetic system	26
2.1.2 Low dimensionality effects	28
2.2 Magnetization reversal in nanoislands	31
2.2.1 The Stoner-Wohlfarth and the Néel-Brown models . . .	31
2.2.2 Dynamical susceptibility of a particle assembly	34
2.2.3 Beyond the macrospin model	36
2.3 Magnetism of hybrid and molecular systems	39
2.3.1 The impact of molecular adsorbates on nanomagnetism	39
2.3.2 Magnetism of metal-organic frameworks	41

2.3.3	Organic spintronics	43
3	Experimental Methods	45
3.1	UHV apparatus	45
3.1.1	Sample Preparation	47
3.1.2	Metal Deposition	47
3.1.3	Molecule Deposition	49
3.2	Scanning Probe Microscopies	50
3.2.1	Scanning Tunneling Microscopy	50
3.2.1.1	Principles of STM	50
3.2.1.2	Variable Temperature STM	52
3.2.2	Atomic Force Microscopy	53
3.2.2.1	Principles of AFM	53
3.2.2.2	Kelvin Probe Force Microscopy	55
3.3	Magneto-Optic Kerr Effect	56
3.3.1	Principles of MOKE	56
3.3.2	Experimental setup	58
4	Growth on linear Au(111) and magnetism of Co island arrays	61
4.1	Au(111) surface	62
4.1.1	Au(111) with herringbone reconstruction	62
4.1.2	Au(111) with unidirectional reconstruction	64
4.1.2.1	Description of the multilayer sample	65
4.1.2.2	STM study of Au(111) with linear reconstruction	66
4.2	Self organization of Co on Au(111)	68
4.2.1	Co nanoislands with increasing size	68
4.2.2	Co nanoislands with elongated shape	72
4.2.2.1	Growth at low temperatures	72
4.2.2.2	Growth on Au-Pt surface alloy	73
4.3	Magnetism of Co on Au(111)	75
4.3.1	Magnetism of Co nanoislands as a function of their size	76
4.3.2	From uniform rotation to spin-wave assisted reversal	78
4.3.3	Magnetism of Co nanoislands with elongated shape	84
4.4	Conclusions	85
5	Metallic and molecular capping of Co nanostructures	87
5.1	Capping with a metal: core-shell Co-Pt islands	88
5.1.1	STM study of Pt growth on Co islands	88
5.1.2	Magnetism of Co-Pt core-shell nanoislands	90
5.2	Capping with molecules: thiols on Co	95
5.2.1	STM study of thiols growth	95

5.2.1.1	Alkanethiols on Au(111)	96
5.2.1.2	Alkanethiols on Co(0001)	100
5.2.1.3	Growth of thiols on and around Co nanoislands	104
5.2.2	Effect of thiols on Co magnetic behavior	107
5.2.2.1	On the ferromagnetism of thin films	107
5.2.2.2	On the superparamagnetism of nanoislands .	114
5.3	Conclusions	116
6	Molecular patterning with AFM	117
6.1	Principles and procedures of Dip-Pen Nanolithography	118
6.2	Kelvin Probe characterization of nanopatterns	120
6.3	Study of the transfer function of KPFM	122
6.4	KPFM as diagnostic tool to study thiols structure	125
6.5	Conclusions	131
	General conclusions	133
	Bibliography	137

General introduction

The dawning era of nanotechnology promises to transform the world as we know it, by means of a complete control of the structure and properties of matter. Even if it is increasingly regarded as the next industrial revolution, nanotechnology is not just another step towards miniaturization. Indeed, it is based on a qualitatively new behavior of matter where unique properties, phenomena and processes, arise from quantum mechanics, material confinement and large interfacial-volume ratio. As such, it originates from the fundamental understanding of how nature works on the atomic scale, as in recent years addressed by nanoscience. Since nanoscience and nanotechnology approach the matter and nature in a completely new way, they require the convergence and synergy of different disciplines and do not simply range across different branches of science and engineering.

One of the first issues to be faced in order to exploit the potential of nanotechnologies is nanofabrication, i.e. the process of making functional structures with suitably designed patterns, having at least one dimension below 100 nm. In order to find a practical use, the fabrication techniques should be economically viable and capable to get a high throughput. Moreover, the nanofabrication techniques should be able to control precisely size and shape of nanostructures, which strongly influence their properties. The study of such an influence is particularly important, since it permits to get deeper insights into the phenomena which underlie a certain behavior. Apart from size and shape, also the surface (or interface) play a major role in nanostructures, due to their large surface-to-volume ratio with respect to bulk materials. For this reason it is possible to tailor a determined property simply by replacing an interface with a new one. Understanding the processes at the interface is particularly important if different materials are assembled to form more complex systems (and especially devices).

Despite being an emerging field, nanotechnology is already facing an important specific challenge, which consists in permitting the continuous miniaturization process in microelectronics and magnetic data storage. The increase in storage density implies naturally the downscaling of ferromagnetic

domains size. Unfortunately, this is accompanied by a decrease in the activation energy for magnetization reversal E_a , which prevents spontaneous changes in magnetization direction (with consequent information loss). This impose a minimum size of particles that can be used for magnetic recording and this restraint is known as superparamagnetic limit. To overcome this limit it is necessary to combine the understanding of the underlying basic phenomena with the search for new materials. Simultaneously, new approaches to bypass the problem have been proposed. The technological demand is therefore seen to boost the research in nanomagnetism, which is now among the most successful fields of nanoscience.

The present thesis work deals with the study of the growth and the magnetic properties of surface supported metallic, molecular and hybrid nanostructures. The fabrication of these nanostructures is made by following complementary approaches, namely self-organized growth of metal islands and dip-pen nanolithography. A common feature is to exploit the self-organization and self-assembly of metals and molecules on Au surfaces. However, in one case atoms spontaneously organize thanks to the Au surface reconstruction, while in the other one the pattern arises from a localized delivery of molecular components. The two techniques are fundamentally different and belong respectively to the bottom-up and top-down approaches to fabricate nanostructures. The substantial difference of these routes, together with their principles and the main techniques to follow them, will be briefly described in the first chapter of the manuscript.

The second chapter will be devoted to the magnetism in low dimensional systems. In the first part of the chapter we will highlight the main features arising if the size of a ferromagnetic system is reduced down to the nanoscale. If small, non-interacting nanoislands are considered, then it is possible to describe their magnetic behavior in the frame of the macrospin approximation. The concepts which underlie this model, their predictions and limitations will be illustrated. The last part of the chapter will provide a glimpse of relatively new trends in nanomagnetism, in particular we will deal with the influence of adsorbates on thin films magnetism, the behavior of molecular metal-organic systems and organic spintronics.

The third chapter will introduce the experimental techniques used. Firstly we will present the Ultra High Vacuum apparatus where a considerable part of the work has been realized. Then the physical principles and the capabilities of Scanning Probe Microscopies will be shortly described. Scanning Tunneling Microscopy (STM) and Atomic Force Microscopy (AFM) have become essential techniques in the study of surfaces and supported nanostructures. The magnetic behavior of the nanostructures has been studied with Magneto

Optical Kerr Effect (MOKE), the physics at the basis of this technique will be introduced in the last part.

Finally, the last three chapters are devoted to the presentation and the discussion of the original results obtained during this thesis work. The fourth chapter will be dedicated to cobalt on gold. The template capabilities of the gold surface have been developed to study the magnetism of nanoislands with different size and shape. To do so, two parallel routes will be developed along the chapter. The first one will exploit the so-called herringbone reconstruction, which easily allows to tune the size of the islands. The second one is more original, and is based on the Au(111) surface, where reconstruction is lifted and a suitable template to grow elongated nanoislands is obtained. Then, the magnetic behavior of the nanoislands will be studied in relation of their morphology.

In the fifth chapter the attention will be focused on the role of interface. A simple way to study this consists in capping the cobalt nanostructures with another given material. Its growth on the nanostructures can be followed with STM, while MOKE measurements permits to study the change in magnetic properties of cobalt. The chapter will be divided in two main parts since cobalt is covered with two completely different materials, a metal (platinum) and an organic molecule (an alkanethiol).

Finally, the last chapter of this manuscript will be also focused on the study of alkanethiols. Monolayers of these molecules will be disposed in patterns with a precise geometry by using an AFM tip. After a brief presentation of the technique employed, we will show how thiols modify the surface potential of gold. This will permit to study how their assembly change with the deposition conditions and how the structure adopted by thiols on the surface influences the layer properties.

Engineering metallic and molecular nanostructures at surfaces

In both academia and industry it is necessary to develop the ability to purpose-build nanoscale systems to capitalize on the full potential of nanostructured materials and their properties. The so-called conventional techniques, which are commercially available and widely implemented in manufacturing, face some difficulties in upholding the continued miniaturization trend. New methods for the controlled fabrication of functional atomic and molecular assemblies are thus needed, capable also to integrate these nanostructures into working macroscopic devices. For these reasons in the last decades a series of unconventional techniques to pattern nanostructures have been proposed, potential low-cost methods capable to achieve ultimate resolution.

The nanofabrication methods are divided into two main groups which follow two opposite approaches: top-down and bottom-up. Top-down techniques essentially impose a structure or pattern on the substrate being processed. In contrast, bottom-up methods aim to guide the assembly of atomic and molecular constituents into organized surface structures through processes inherent in the manipulated system. During these thesis work we have used techniques belonging to both these families to pattern surface supported nanostructures. In this chapter we will describe the principles underlying the two approaches and briefly review the most important methods with the aid of

some relevant examples.

1.1 Top-down approaches

Top-down approaches in nanotechnology may be seen as modern analogues of ancient methods such as lithography, writing or stamping, but capable of creating features down to the sub 100 nm range [Gates et al., 2005]. They include both serial and parallel techniques for patterning features over length scales approximately four orders of magnitude larger than an individual structure.

1.1.1 Photolithography and scanning beam lithography

Photolithographic methods all share the same operational principle: exposure of an appropriate material to electromagnetic radiation (visible, UV, or X-ray) introduces a latent image (usually a difference in solubility) into a resist material as a result of a set of chemical changes in its molecular structure; such a latent image is subsequently developed into relief structures through etching. Methods based on writing with particles (electrons or ions) usually accomplish the same task using energetic particles rather than photons. Exposure can be performed either by interposing a mask between the source of radiation (or particles) and the material or by scanning a focused spot of the source across the surface of the material. When masks are used, the lithographic process yields a replica (perhaps reduced in size) of the pattern on the mask, while the focused beam is scanned according to the desired pattern design. Thus, photolithography permits the parallel generate patterns whose shape is determining by the mask's one. The resolution of photolithography

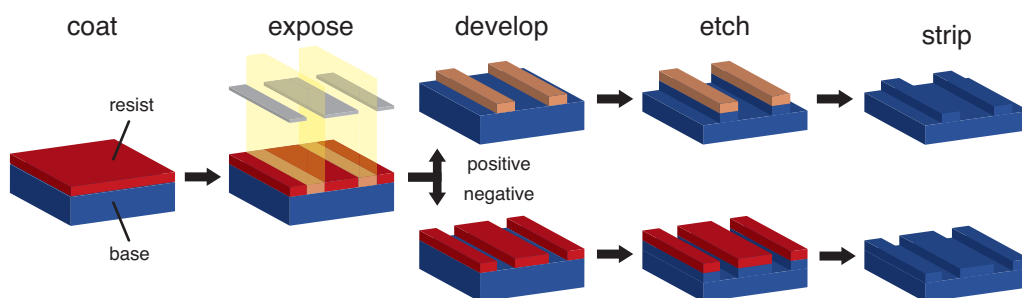


Figure 1.1: Schematic representation of photolithographic process sequences. For scanning beam techniques the exposure is performed by scanning a focalized beam.

is relatively low and is determined by the energy of radiation used. In particular, it increases as the wavelength of the light used decreases, as determined by the Rayleigh criterion [Ito and Okazaki, 2000]. This limit was overcome by using a photochromic layer as a resist: this permitted to fabricate pattern with a minimum lateral size around 30 nm with visible light [Andrew et al., 2009]. On the other hand, scanning beam lithography is more powerful, capable to fabricate patterns of arbitrary shape with features as small as 3 nm in lateral size [Cumming et al., 1996]. Nonetheless it is a complicated and expensive technique that suffers of time restriction due its serial character, thus it is often limited to small areas or low density of features.

1.1.2 Molding, embossing and printing

The common feature of molding, embossing and printing is the use of a template with the patterns envisaged, the master. The difference between them relies on the procedure followed to replicate the master's features. Molding and embossing are reshaping procedures, while printing requires a local transfer of material from a tool onto a substrate. In molding techniques a transparent master, that contains nanoscale surface-relief features, is pressed into a monomer or prepolymer layer which is solidified by UV curing [Haisma et al., 1996]. The procedure of embossing techniques is similar, but the polymer is already cured and mechanically deformed by heating it above the glass transition temperature [Chou et al., 1996]. The concept of microcontact printing is different. An elastomeric stamp is inked with a reactive molecule and printed onto a thin film where the molecules self-assemble. The self-assembled monolayer protects the thin film so that a selective etch can be performed [Kumar

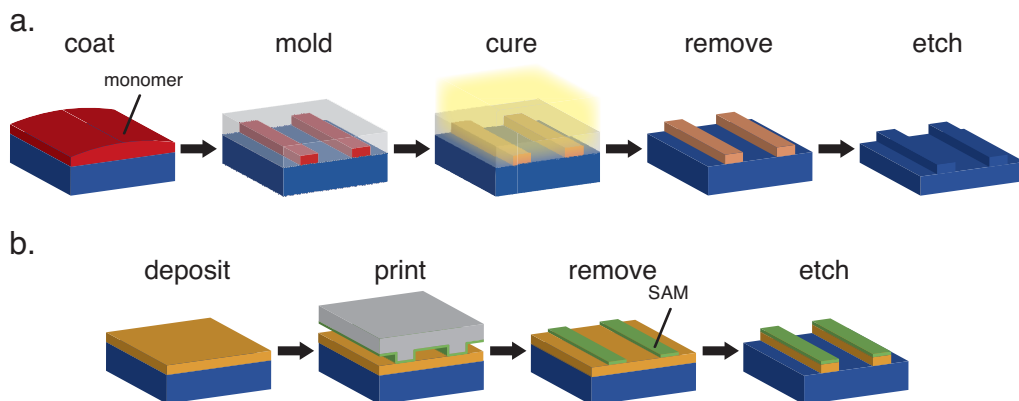


Figure 1.2: Schematic representations of molding (a) and microcontact printing (b) process sequences.

and Whitesides, 1993]. All these techniques present the advantages of the parallel nature of the process, the high throughput and the low system costs; moreover microcontact printing is suitable for nonflat surfaces. These techniques can also reach high resolution: indeed, by using carbon nanotubes as templates for mold-assisted lithography, features as small as 2 nm in lateral size were obtained [Hua et al., 2004].

1.1.3 Scanning probe lithography

Both STM and AFM are well-known techniques capable to image surfaces with high resolution (which will be described in more details in Sec. 3.2). Taking advantage of the tips sharpness and of strong by localized tip-surface interactions, these microscopies have also been used to manipulate matter and to fabricate nanopatterns and are now proven methods for the direct writing and positioning of individual atoms and molecules. Scanning probe lithography techniques are capable to reach ultimate resolution, but as a drawback they are cumbersome. In order to multiply the throughput, tip arrays have been proposed [Vettiger et al., 2002] but to achieve industrial applications major improvements are still needed. The most common way to pattern surfaces with these techniques is by mechanical modification, which can be performed both with STM and AFM. In AFM the most common procedure is scratching: a high applied load causes the tip to plow through the sample and the material on the sample surface is displaced. A different procedure is used with STM: if the tip is lowered close to the surface, adatoms can adhere to it, dragged across the substrate and then released in a new location [Eigler and Schweizer, 1990] (Fig. 1.3a,b). More recently, this atomic precision was reached also with AFM by interchanging atoms between the tip apex and a semiconductor surface [Sugimoto et al., 2008]. Scanning probe lithographies can also modify surfaces chemically. One example is the localized oxidation of a surface in a pattern scanned by a conductive AFM or STM tip. A local electric field between the tip and the surface induces oxidation of the surfaces [Dagata et al., 1990] (Fig. 1.3c,d). Also, AFM permits other thermal-based lithographic techniques that permits to locally indent a polymeric substrate [Mamin, 1996] or to locally desorb an organic glassy resist [Pires et al., 2010].

A series of scanning probe lithographies involving self-assembled monolayers (SAMs, see 1.2.3.2) have also been reported [Kr amer et al., 2003]. For example, in STM-based lithography the tunneling electrons are used to induce the evaporation of molecular constituents of SAM and thus to pattern features (Fig. 1.3e,f). On the other hand, with AFM the application of a high load causes the detachment of molecules (Fig. 1.3g,h). This elimination processes can be followed by a in-situ addition of a different molecule into the exposed

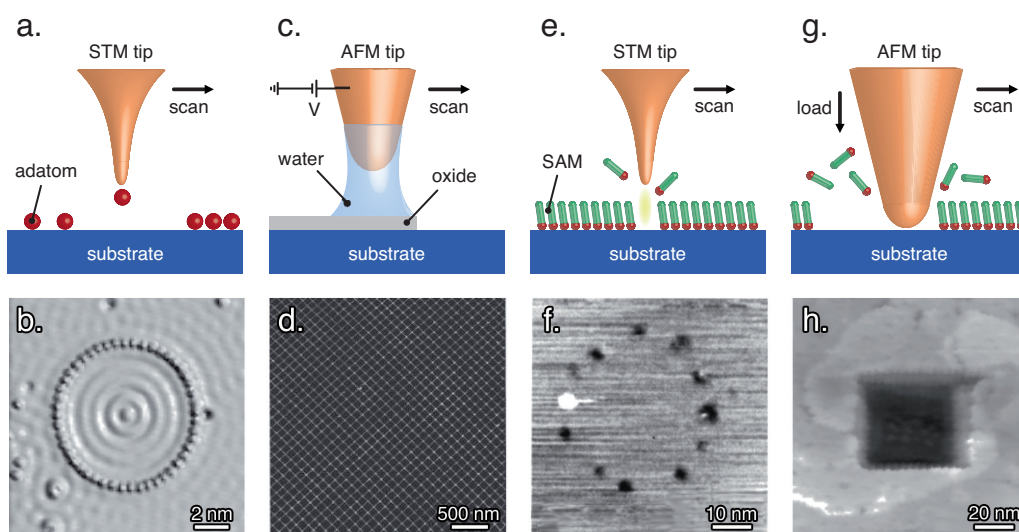


Figure 1.3: Schematic representation of some scanning probe lithographic techniques. a. STM can position atoms with high precision to generate patterns, such as a quantum corral of Fe atoms (b, figure extracted from [Eigler and Schweizer, 1990]). c. Scanning electrochemical oxidation with AFM can selectively oxidize a surface to pattern features such as d. (figure extracted from [Dai et al., 1998]). e. Tunnel electrons can induce the evaporation of molecular constituents of SAM and produce patterns like f. (figure extracted from [Mizutani et al., 1998]) g. Nanoshaving can remove regions of SAMs causing holes and trenches such as h. (figure extracted from [Liu et al., 2000]).

surface. Two molecules can be patterned on the surface also if the probing tip chemically transform the molecular headgroups into a new functionality. Finally, the tip can be used to deliver reactive molecules directly onto the substrate, where they auto-assemble forming the final pattern. This approach is used in Dip-Pen Nanolithography, a technique which will be described in more details in Chap. 6.

1.2 Bottom-up approaches

Bottom-up techniques utilize the spontaneous or direct assembly of nano-sized building blocks to form more complex structures. A common feature of all these strategies is that they are essentially based on growth phenomena. In the case of surface supported nanostructures, atoms or molecules are deposited on the substrate where nanostructures evolve as a result of different

processes [Barth et al., 2005]. We will briefly show here the concepts underlying the approach and how this might lead to the formation of useful nanostructures. A brief introduction to the elementary processes governing surface self-ordering provides the foundation for the subsequent discussion of how these processes can be tuned in metallic and molecular systems to obtain surface structures with desired geometric order and well-defined shapes.

1.2.1 Generality of nucleation and aggregation

Thin film growth is inherently a non-equilibrium phenomenon and thus it is governed by the competition between kinetics and thermodynamics. The first consequence of this competition concerns the terminology used to describe the growth of nanostructures. The term self-organized growth refers to phenomena mediated by mesoscopic force fields or kinetic limitations in growth processes, while in self-assembly the ordered state forms a system that approaches equilibrium, reducing its free energy. More importantly, the opposition of thermodynamic quantities (such as surface and interface free energies) and growth kinetics determines the film morphology, which changes with the degree to which growth proceeds away from equilibrium. Thin film growth can be discussed as a wetting problem if it occurs near thermal equilibrium, and structures emerge following surface free energies considerations, by calculating $\Delta\gamma = \gamma_f + \gamma_i - \gamma_s$, where the quantities γ_f , γ_i and γ_s are the surface free energies at the film-vacuum interface, the film-substrate interface and the substrate-vacuum interface. If $\Delta\gamma < 0$ the topmost layer is wetting the surface underneath and Frank-van der Merwe or layer-by-layer (2D) growth is expected. On the contrary if $\Delta\gamma > 0$ the adlayer material does not wet the substrate easily and Volmer-Weber growth or island (3D) growth is found. The Stranski-Krastanov mode is an intermediate case, where $\Delta\gamma$ changes sign at a critical layer thickness due to strain energy accumulation, causing a transition from 2D to 3D growth [Venables, 2000].

The thermodynamic limit is hardly reached and it is often necessary to work far away from equilibrium. Such a case is encountered in Molecular Beam Epitaxy (MBE) where a high supersaturation is needed to grow films rapidly from the vapor phase. For vapor deposition from an ideal gas phase at pressure p , the rate of arrival F at the substrate is $F = p / \sqrt{2\pi mk_B T}$ where m is the molecular weight and T is the source temperature. Upon deposition, single atoms (adatoms) or molecules are created on the substrate which are subject of several processes, schematically represented in Fig. 1.4 for a flat substrate terrace. Among them, the fundamental process is terrace migration. If we define a migration barrier E_m , the mean square displacement of one isolated random walker atom (or molecule) is determined by the diffusion coefficient

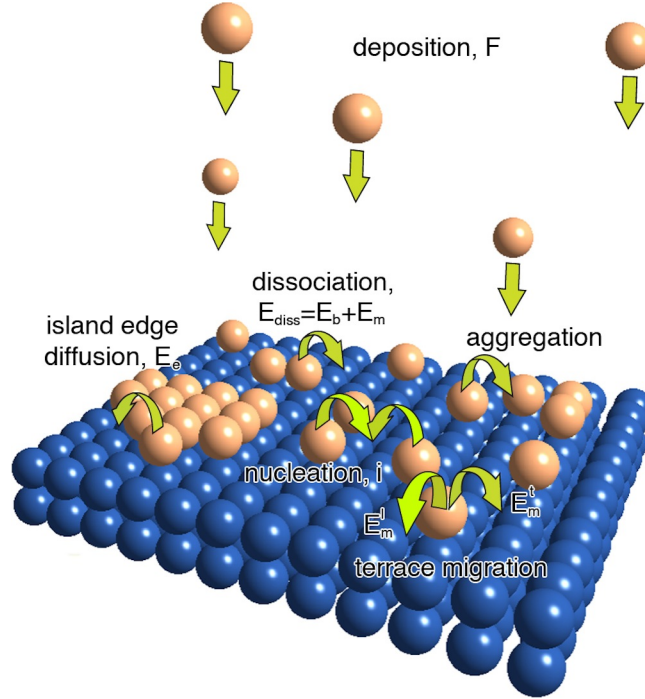


Figure 1.4: The elementary diffusion processes of molecular beam epitaxy growth on a flat terrace.

$D = D_0 \exp(-E_m/k_B T)$. In the nucleation regime, diffusion across the surface ends when two diffusion species collide forming a new stable nucleus. This process becomes less and less probable when deposition proceeds. A growth regime is established where diffusing adatoms exclusively attach to existing islands, contributing to their growth. As a consequence a so-called critical island density n_c is reached. By writing the rate equations for the density of monomers and stable islands, it is possible to find an analytical expression for n_c in the frame of the mean-field nucleation theory [Venables et al., 1984]:

$$n_c = \eta(\theta, i) \left(\frac{D}{F} \right)^{\frac{i}{i+2}} \exp\left(\frac{E_i}{(i+2)k_B T} \right), \quad (1.1)$$

where E_i is the cluster binding energy, i is the critical cluster size (upon which the cluster is stable) and η is a prefactor related to capture numbers. This expression is valid in the 2D case and in a complete condensation regime (where re-evaporation of adatoms from the substrate is absent). This equation highlights the key importance of the deposition rate of atoms and molecules F and the diffusion coefficient of atoms at the surface D . The ratio of these two parameters permits to control the density of islands (and thus the size, at a given

submonolayer coverage) on the surface. It is important to highlight that this is another manifestation of the contraposition of thermodynamics and kinetics. If D/F is large the adsorbed species have enough time to explore the potential energy surface so that the system can reach a minimum energy configuration; on the other hand if D/F is small the pattern of growth is determined by kinetics and metastable structures are obtained.

1.2.2 Metal self-organization

1.2.2.1 Homogeneous growth on flat and anisotropic surfaces

We concentrate here on the case metals, whose bonding have essentially no directionality so that it is possible to guide their arrangement only by exercising a kinetic control on their growth [Brune, 1998]. In the previous section we saw the importance of the parameters D and F in determining the density of nanoislands. However, their size and shape is determined mainly by the details of adatoms diffusion, and in particular by the competition between the different movements atoms can effectuate on the surface. Each one of these movements has a characteristic energy barrier, which makes it possible to control the shape of nanoislands by selective activation or suppression of particular diffusion processes in the hierarchy of diffusion barriers.

The importance of this selective activation is clear even on flat and highly symmetric surface. For example, if edge diffusion is frozen, atoms are not transported away sufficiently fast, leading to the formation of branches. Thus, the shape of the islands can be changed from dendritic to compact only by increasing the deposition temperature. Typical example are the growth of Au on Ru(0001) [Hwang et al., 1991] or Pt homoepitaxy [Bott et al., 1992]. Surface with a lower symmetry are characterized by diffusion barriers which are more orientation dependent. A typical example of these anisotropic substrates is the (110) surface of fcc metals, which presents atomic channels in the $[1\bar{1}0]$ direction. The diffusion along the channel is favored with respect to that along the orthogonal direction. Thus, by freezing the cross-channel diffusion in favorable temperature conditions it is possible to obtain a unidirectional diffusion of adatoms and monodimensional chains. The feasibility of this route was firstly demonstrated for Cu on Pd(110) [Röder et al., 1993].

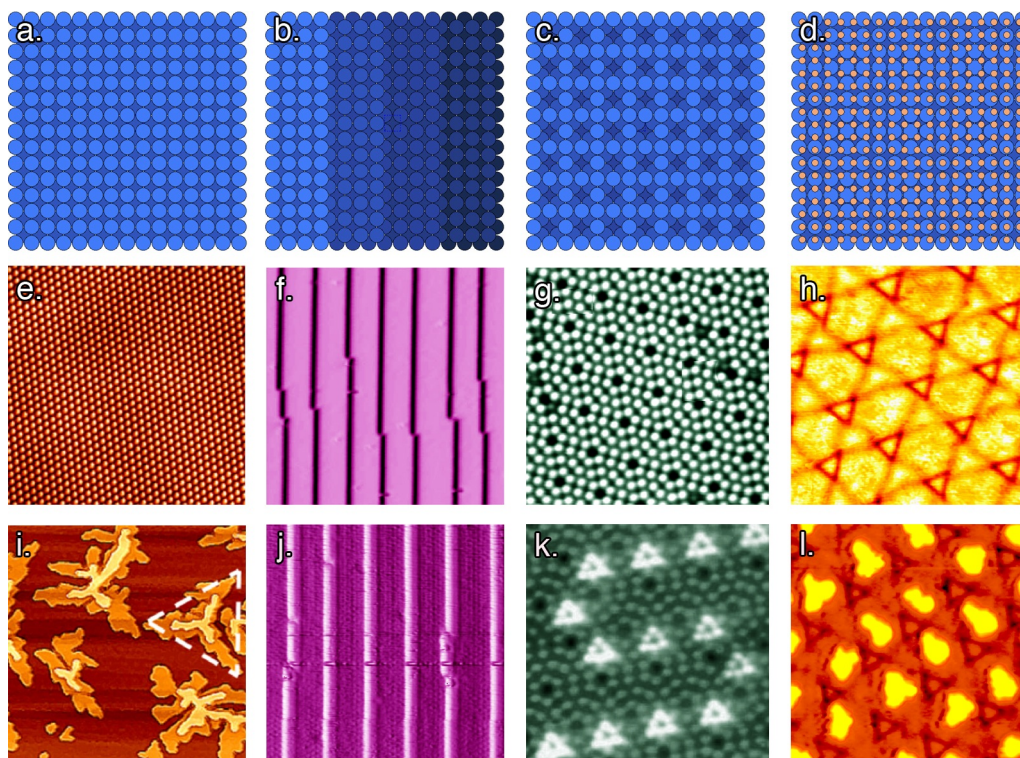


Figure 1.5: Schematic representation of different template surfaces (a-d), STM images of corresponding typical cases (e-h) and deposition on these surfaces (i-l).

- a. Original surface with 2D lattice.
- b. Vicinal surface.
- c. Reconstructed surface.
- d. Strain-relief epitaxial layer.
- e. Ag(111) surface ($8 \times 8 \text{ nm}^2$)
(image taken from <http://ipn.epfl.ch/page47585.html>).
- f. Vicinal Pt(997) surface ($17 \times 17 \text{ nm}^2$) [Gambardella et al., 2006].
- g. Si(111)- 7×7 surface reconstruction ($20 \times 20 \text{ nm}^2$) (image taken from <http://www.chem.uic.edu/mtrenary/STM%20gallery.html>).
- h. 2 ML Ag/Pt(111) strain-relief pattern dislocation ($25 \times 25 \text{ nm}^2$) [Ait-Mansour et al., 2009].
- i. Ag dendritic islands on Ag(111) ($90 \times 90 \text{ nm}^2$) [Li et al., 2009].
- j. Single monoatomic Ag wires decorating Pt step edges ($13 \times 13 \text{ nm}^2$) [Gambardella et al., 2000].
- k. In nanocluster on Si(111)- 7×7 [Li et al., 2002].
- l. Ag nanoislands on Ag/Pt(111) ($30 \times 30 \text{ nm}^2$) [Brune et al., 1998].

1.2.2.2 Heterogeneous growth on template surfaces

So far we have considered a deposition on surfaces where all the sites are equivalent. As a consequence, we were in the frame of homogeneous nucleation and growth. The aleatory character intrinsic to these processes makes it hard to control the arrangement of the nanostructures on the surface. This drawback can be overcome by using template surfaces, i.e. nanostructured substrates with inequivalent atomic sites. In particular, some of them can act as preferential nucleation sites and can be regarded as traps for diffusing species, leading to heterogeneous nucleation and growth. In this way the substrate structure can guide different metals towards the same precise arrangement. In figure 1.5 some relevant examples of these patterned surfaces are shown, together with typical metal deposition on these templates. We will here briefly report some important examples of surfaces exhibiting spontaneous nanoscale order and discuss to which extent they can guide metal growth.

Vicinal surfaces can be obtained by cutting the crystal at a small angle with respect to high-symmetry plane to create a surface that consists of flat terraces separated by atomic step edges. The elastic repulsion between the step edges induces a regular spacing of the steps. Moreover, the size of the terraces is tunable since it can be varied with the miscut angle. The nucleation of adatoms at step edges is favored by a higher coordination number. In this way it is possible to grow nanowires of various width only by changing the metal coverage, like shown on Pt(997) [Gambardella et al., 2000]. Vicinal surfaces can be exploited also to build bidimensional arrays of nanoparticles. Au vicinal surfaces are an important example, since Au reconstruction is superimposed to the stepped template, creating a 2D network of preferred nucleation sites [Rousset et al., 2003]. Indeed, reconstructed surfaces constitute another important class of template substrates. Reconstruction is due to the undercoordination of surface atoms which reorganize in order to achieve an equilibrium state with lower free energy. Within the surface supercell the sites are not energetically equivalent giving rise to preferred nucleation sites. Surface reconstructions can occur both on clean surfaces or upon adsorption. In the former cases the most famous examples are the Si(111)- 7×7 and Au(111) surfaces. Au(111) reconstruction will be described in detail in Sec. 4.1 due to its importance in the present thesis work. Here, it is important to anticipate that a dislocation network is formed to release the strain in the topmost layer. For this reason it is often associated with strain-relief patterns. These are more commonly observed in epitaxial thin films whose unit cell size mismatches with the cell size of the substrate. The strain imposed on the thin films by substrate lattice is then released by reconstruction of the film. A representa-

tive example is constituted by 2 ML of Ag on Pt(111) where silver atoms alternate in fcc and hcp stacking forming a hexagonal pattern [Brune et al., 1994]. Cu on Ru(0001) represents another interesting example, since the first four monolayers of copper shows pronounced variations in morphology [Günther et al., 1995].

All these patterned surfaces show a regular two-dimensional strain relief patterns or reconstruction patterns with feature size in the nanometer scale, which can serve as template to control the growth of metals towards the formation of ordered nanoislands arrays. The regime of self-organized growth is attained only in a relatively wide temperature range included between the temperature to which the diffusion is large enough to reach the nucleation sites and the temperature to which the trap energy is sufficient to stabilize the diffusing adatoms [Rousset et al., 2005; Repain et al., 2006]. In this self-organization regime the islands density is fixed and corresponds to the density of nucleation sites, as shown in Fig. 1.6a for Co on Au(788). Moreover, since the nucleation sites are periodically arranged the capture areas are similar and this leads to regular islands with a size distribution significantly nar-

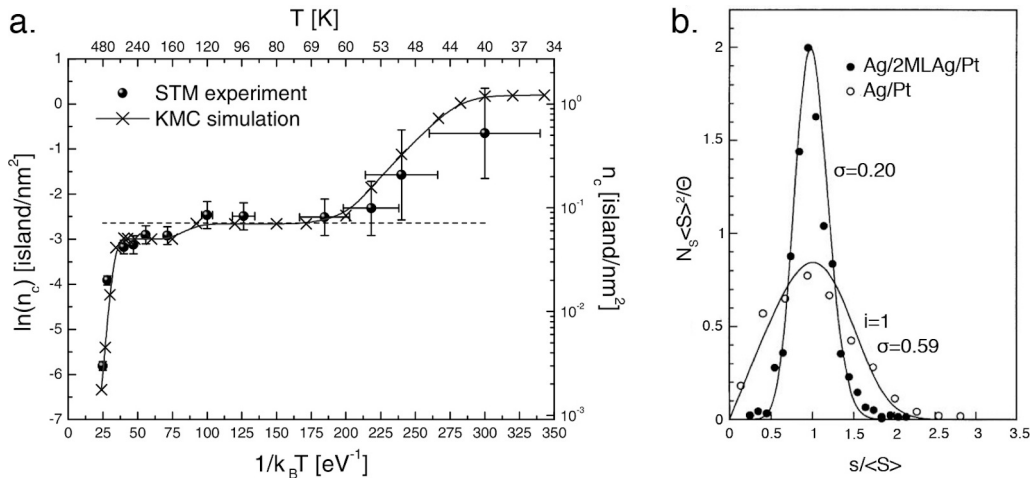


Figure 1.6: a. Critical island density n_c as a function of the deposition temperature for Co on Au(788), according to STM experiments (full symbols) and Kinetic Monte Carlo simulation (crossed symbols). The dotted line indicates the density of nucleation sites (figure extracted from [Rohart et al., 2004]). b. Island size distributions for random (Ag on Pt) and ordered nucleation (Ag on Ag/Pt dislocation network). In the first case the theoretical curves (full line) is obtained from scaling theory for random nucleation [Amar and Family, 1995], in the second is a binomial fit (figure extracted from [Brune et al., 1998]).

rower than that formed on a homogeneous substrate. The different islands size distributions is evident if comparing the size distribution of Ag islands if they are deposited on Pt at 95 K and if they are deposited on the strain-relief pattern 2 ML Ag/Pt at 110 K [Brune et al., 1998], as shown in Fig. 1.6b.

1.2.3 Molecular self-organization

1.2.3.1 Supramolecular architectures

Differently from metals, molecules can exhibit weak and directional non-covalent bond, which may be engineered to form desired supramolecular structures in a condition close to thermodynamical equilibrium. Chemical synthesis can provide a virtually unlimited collection of molecular building blocks (the so-called tectons) which can assembly in the desired fashion by exploiting different intermolecular bondings and interactions with the substrate. The way in which molecules interact with each other and how non covalent interactions can be exploited to create order assembly is the subject of supramolecular chemistry, for which Cram, Lehn and Pederson were awarded with the Nobel prize in 1987 [Lehn, 1995]. The extreme versatility of this approach could lead to two-dimensional crystal engineering [Elemans et al., 2009].

Among the above mentioned interactions, hydrogen bonding is one of most frequently exploited, because it is relatively strong and highly directional. When exploited to guide supramolecular assembly this interaction permits to obtain a rich variety of molecular motifs. To this purpose carboxylic acid groups are particularly useful, since they are at the same time H-bond donors and acceptors. By changing the position and the number of these substituents on the same benzene core it is possible to obtain linear arrays, zig-zag patterns or honeycomb networks [Lackinger et al., 2004; Dmitriev et al., 2002]. These same tectons (benzenecarboxylic acids) can also adopt different structures by changing the coverage [Ye et al., 2007]. Dipole-dipole interactions can also be exploited, which arises for example between neighbouring cyanophenyl substituents. This group dominates hydrogen bonding and permits to control the assembly of aggregates with different size and shapes, depending on the position of the cyanophenyl groups [Yokoyama et al., 2001].

Well-defined surface patterns can also be based on metal-ligand coordination interactions, generally stronger than hydrogen bonding but with the same properties in terms of specificity and directionality. More importantly, the incorporation of metal centers can introduce new functionalities in the metal-organic framework. As a complication, metal atoms tend to strongly interact with the substrate. The architectural motif of these networks are de-

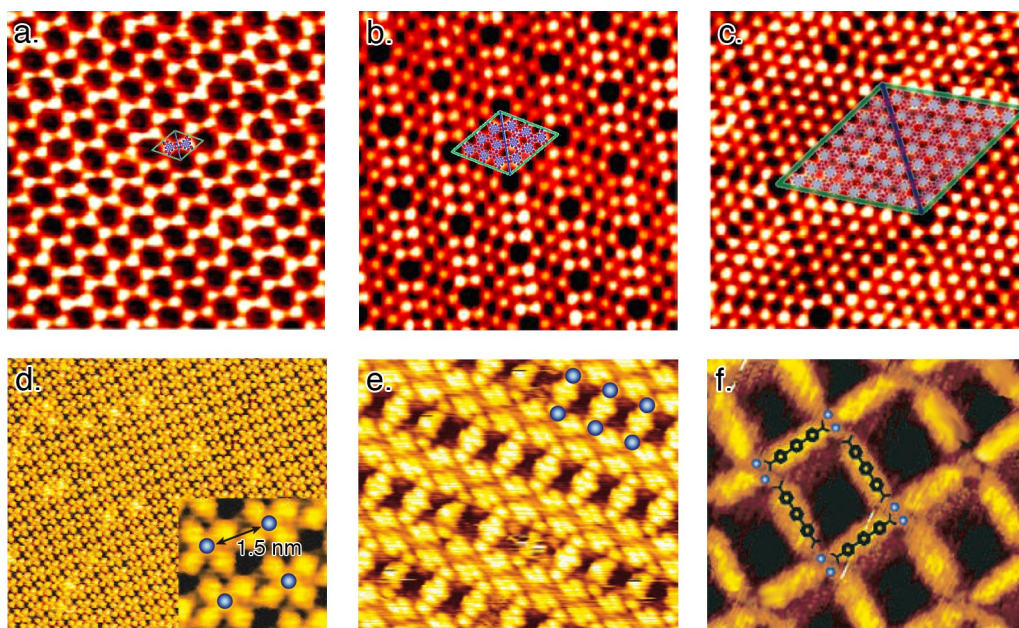


Figure 1.7: a-c STM images ($16.5 \times 16.5 \text{ nm}^2$) of coverage-induced evolution of benzene-tricarboxylic acid, corresponding unit cells have been superposed (figures redrawn from [Ye et al., 2007]). d-f STM images of different Fe-carboxylate coordination systems on Cu(100) substrate: 0D clusters ($30 \times 26 \text{ nm}^2$), 1D carboxylate-bridged Fe chain ($8 \times 7 \text{ nm}^2$), 2D reticulated coordination networks ($8 \times 7 \text{ nm}^2$) (figures extracted from [Barth et al., 2005]).

terminated not only by the number and arrangement of the ligand groups (typically carboxylic acids and porphyrins) but also by the relative concentrations of metal atoms and ligand molecules. By controlling their ratio it is possible to pass from 0D isolated clusters to fully connected 2D networks [Barth et al., 2005].

1.2.3.2 Self-assembled monolayers

So far we have considered physisorbed molecules, whose organization is dictated by intermolecular bonding in the frame of supramolecular chemistry. However when dealing with molecular self-assembly at surfaces, one often refers to chemisorbed molecules. In this category self-assembled monolayers are fundamental [Ulman, 1996; Love et al., 2005]. These are made of molecular components which show a special affinity for a substrate thanks to their head group, in addition, they have a tail with a functional group at the termi-

nal end. SAMs are created by the chemical bonding between the head group and the substrate, which is followed by a two-dimensional organization of tail groups. The monolayers adopt a compact, often crystalline structure due to van der Waals interaction. Strictly speaking, SAMs usually do not naturally pattern surfaces, but are commonly used as resist in lithographic techniques as discussed in Sec. 1.1. However, the fact that they easily form robust and stable structures makes them well-suited in various applications. As for supramolecular assembly, a wide variety of molecules capable to form SAMs can be prepared by exploiting the possibilities offered by chemical synthesis. Indeed, both the tails and terminal groups can be tailored for specific applications and, to a lower extent, to guide the arrangement on surfaces. Within the possible combinations of molecules and substrates, thiols (R-SH) on Au and silane-based systems on silica were identified as model systems.

1.3 Conclusions

In this chapter we get only a partial view on the variety of techniques which can be employed nowadays to create low dimensional nanostructures. However, it should be clear that to this purpose both top-down and bottom-up techniques offer efficient and versatile tools. Bottom-up approaches are promising since they can produce high-density structure with lateral size of few nanometers in a fast and parallel fashion. In general top-down techniques are limited in resolution and slower, but are currently the only techniques capable to allow the integration of nanostructures into larger systems and functional devices. For this reason, in the nearest future a combination of top-down and bottom-up methods would probably offer the most feasible route to new devices.

Due to their importance in this thesis work, some of the concepts introduced in this chapter will be discussed in more details in the following of the manuscript. In Chap. 4 the Au(111) reconstruction will be presented, and its ability to guide the growth of metals (Co in particular) towards the formation of ordered nanoisland arrays will be shown. In Sec. 5.2.1.1 a more detailed description about the growth and structure of alkanethiols SAMs on Au. Finally, in Chap. 6 will be introduced the Dip-Pen Nanolithography, a technique capable to pattern SAMs through a localized delivery of the molecular constituents.

Magnetism of metallic and molecular nanostructures

The reduced dimensionality that comes with nanoscale magnetic structures introduces abundant novel phenomena interesting on both a fundamental and an applied level. So far, it has been possible to gain deeper insights into the underlying physics thanks to the progresses in the fabrication and in the magnetic characterization techniques. At the same time, the search for materials with new or improved properties has created a synergy that has now put the basis to modify the magnetic behavior of nanostructures in a controllable and desired way. With this capability, nanomagnetism finds at the frontier between modern science and technology.

This chapter is devoted to the magnetic properties of metallic, hybrid, and molecular nanostructures. In the first section we will shortly explain why the behavior of a ferromagnetic sample changes by going from the macroscopic to the nanoscopic scale. Then we will focus on the models describing the behavior of ferromagnetic nanoparticles which are ideal systems for studying the effect of dimensionality lowering. In the last section the magnetic properties of hybrid and molecular systems will be introduced.

2.1 Introduction to nanomagnetism

Nanomagnetism qualitatively differs from the magnetism encountered in bulk materials. In this section, the origin of this difference is briefly explained, with

particular attention to the case of transition metal nanostructures.

2.1.1 Energetics of a ferromagnetic system

From a general point of view, the magnetic energy of a system is determined by the balance of different terms. Here we focalize on a uniaxial magnet of volume V , whose magnetization vector \mathbf{M} has a saturation value M_S . In a continuum theory, the total magnetic energy can be written as following [Skomski, 2008]:

$$E = \int \left(A \left(\nabla \left(\frac{\mathbf{M}}{M_S} \right) \right)^2 - K_1 \frac{(\mathbf{n} \cdot \mathbf{M})^2}{M_S^2} - \frac{\mu_0}{2} \mathbf{M} \cdot \mathbf{H}_D - \mu_0 \mathbf{M} \cdot \mathbf{H} \right) dV. \quad (2.1)$$

The first term accounts for the exchange energy which is at the origin of magnetic order. It favors parallel alignment of spins in the case of ferromagnetism. This is a continuum form of the Heisenberg Hamiltonian $E_{\text{ex}} = -1/2 \sum_{ij} J_{ij} \mathbf{s}_i \cdot \mathbf{s}_j$, where the ferromagnetic exchange is replaced by the so-called exchange stiffness $A \approx J/a$, a being the atomic distance. In the exchange term only relative angles between neighboring spins matter, this term is thus isotropic.

However, the energy of a magnet does depend on the direction of the magnetization with respect to the crystal axes. This important property, known as magnetic anisotropy, is the origin of hysteresis and coercivity affects the second term. Magnetic anisotropy is usually expressed with the simpler expression $E_a = K_1 V \sin^2 \theta$. In uniaxial system, if the second-order anisotropy constant K_1 is positive, the energy has minima at $\theta = 0$ and $\theta = \pi$ which describes an easy axis anisotropy (\mathbf{n} is the unit vector of the direction of this easy-axis). The main source of anisotropy is magnetocrystalline anisotropy that is due to the combined effect of electrostatic crystal-field and relativistic spin-orbit interactions. Briefly, the rotation on the spins creates orbital currents (via the spin-orbit coupling) which interact with the anisotropic crystalline environment.

The third term is the magnetostatic self-interaction energy induced by dipolar interactions. This describes the interaction of every magnetic moment with the magnetic field created by its environment. \mathbf{H}_D is called demagnetizing or self-interaction field. In the case of a thin film uniformly magnetized, the magnetostatic self-interaction appears like an anisotropic term characterized by a constant K_D . It is thus convenient to incorporate this term into the anisotropic one by defining $K_V = K_1 + K_D$. Finally, the last term describes the Zeeman energy of the system if an external magnetic field \mathbf{H} is also applied. The three basic quantities (namely the exchange stiffness A , the anisotropy constant K_1 and the magnetostatic self-energy $\mu_0 M_S^2$) define two important

lengths. These are the wall-width parameter δ and the exchange length Λ :

$$\delta = \sqrt{\frac{A}{K_1}} \quad \text{and} \quad \Lambda = \sqrt{\frac{A}{\mu_0 M_S^2}}. \quad (2.2)$$

δ determines the width of the domain wall separating magnetic domains with different magnetization directions. It shows that the anisotropy energy favors a thin wall while the exchange energy favors a thick wall. δ varies from about 1 nm in extremely hard materials to several hundreds nanometers in very soft materials. Λ measures the particle size below which the magnetostatic energy associated with an uniform magnetization is smaller than the exchange cost required to demagnetize the particle. Therefore a magnetic particle is expected to be a single domain if its size is well below Λ , while if it is larger the decomposition in domains becomes energetically favorable. In the case of bulk hcp cobalt, the exchange length is around 3 nm Rohart et al. [2007]; Šipr et al. [2007].

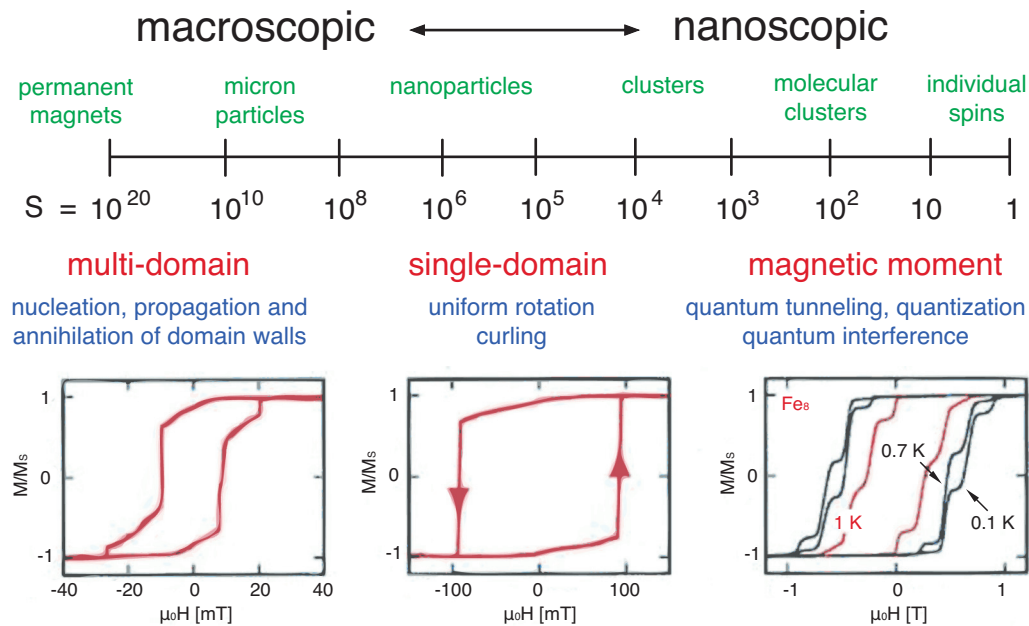


Figure 2.1: Typical hysteresis loops when the size of the systems changes from macroscopic down to nanoscopic dimension. According to the size, the magnetization reversal behavior shows some peculiar characteristics, here schematically summarized (figure extracted from [Wernsdorfer, 2001]).

2.1.2 Low dimensionality effects

Due to the competition between the several contributions to its energy, a ferromagnetic system exhibits different behavior depending on its size, as seen in the previous section. By changing the size of the system, ground state spin configurations and magnetization reversal modes show peculiar characteristics. This is schematically shown in Fig. 2.1 which presents a scale of size, from macroscopic down to nanoscopic systems, and the related characteristic behavior. A macroscopic system is described by magnetic domains and the magnetization reversal occurs via nucleation, propagation, and annihilation of domain walls. At the opposite extreme of the scale there are either free clusters made of several atoms or molecules containing magnetic atoms. The magnetic behavior of these systems can show some new quantum features, like magnetization reversal by tunneling, a mechanism that will be explained briefly in Sec. 2.3.2.

If the size of the system is of the same order of magnitude of δ or Λ , the interplay between the exchange, anisotropy and magnetostatic self-energy is more delicate. If the particle size is below these lengths, the formation of domain walls requires too much energy, so that the magnetization remains in a single-domain state and reverses coherently by uniform rotation. Typically, this behavior is encountered when the nanoparticle is few nanometers in diameter and thus it is in the range of interest of this work; the models describ-

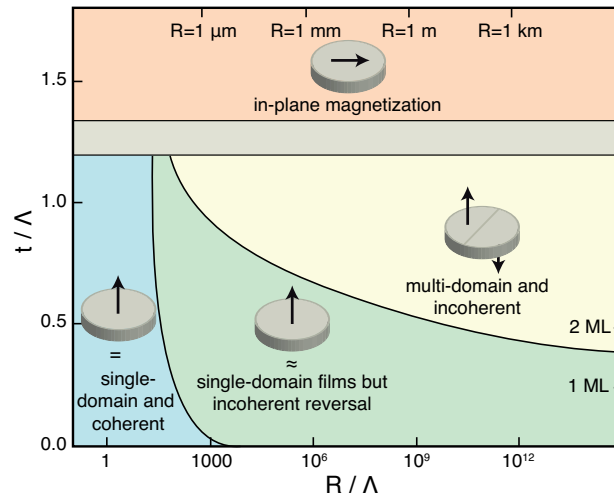


Figure 2.2: Magnetic phase diagram for magnetic nanoparticles with perpendicular anisotropy as a function of the ratio between their radius R and their thickness t and the exchange length Λ . In this case $\Lambda = 2$ nm and $K_S = 0,5$ mJ/m² (figure redrawn from [Skomski et al., 1998]).

ing the magnetic behavior of a single domain nanoparticle are reported in details in Sec. 2.2.1. If the size of the particle is somewhat increased, the particle remains in a single domain ground state, but incoherent reversal modes are more likely, for example by curling or by nucleation and annihilation of domain walls. If the size of the particle is larger of δ or Λ , the particle assumes a bulk-like behavior. This trend was confirmed also by micromagnetic calculations, schematically summarized by Fig. 2.2 [Skomski et al., 1998].

The fact that the dimension of the system is comparable to characteristic magnetic lengths is the first essential reason for the emergence of new phenomena in nanomagnetism. Another important reason comes from the breaking of translation symmetry, which results in sites with reduced coordination number, broken bonds, and frustration. In general, the reduction in the coordination number of surface atoms with respect to the bulk results in different electronic structures and in particular in a narrower density of states. This fact has far-reaching consequences. Here it is important to highlight that the narrowing of the $3d$ band induces an enhancement of the magnetic moments. This effect is generally weak for the spin moment μ_S while it is more pronounced for the orbital moment μ_L , that exhibits significantly increased values [van der Laan et al., 1992]. Indeed, in a bulk transition metal, the orbital momentum is nearly zero, since the crystal field interaction favors quenched orbitals. At the surface the crystal symmetry is broken and this decreases the degree of quenching.

In conjunction with its increase in magnitude, the orbital momentum undergoes a change of anisotropy due to the reduced symmetry. Indeed, by reducing the dimensionality of the system, there is a redistribution of the charge along the different symmetry axis of the structure that, in the case of a transition metal ultra-thin film, causes different bandwidth W for the in-plane and out-of-plane $3d$ orbitals. This gives rise to an anisotropy of the orbital momentum, since $\mu_L \propto \xi/W$, where ξ is the spin-orbit coupling constant. Based

Table 2.1: Experimental values for the orbital momentum and magnetic anisotropy constant of Co atoms on Pt as a function of coordination. (table taken from [Fruchart and Thiaville, 2005]).

	bulk	monolayer	biatomic wire	monoatomic wire	two atoms	single atom
μ_L [μ_B /at.]	0.14	0.31	0.37	0.68	0.78	1.13
K [meV/at.]	0.04	0.14	0.34	2.0	3.4	9.2

on a tight binding approach, it was shown that this causes an additional magnetic anisotropy [Bruno, 1989]:

$$\Delta E_s = E_s^\perp - E_s^\parallel = -\frac{\xi}{4\mu_B}(\mu_L^\perp - \mu_L^\parallel) \quad (2.3)$$

The existence of this important surface anisotropy was firstly foreseen by Néel, long before the first studies in nanomagnetism [Néel, 1954]. The surface anisotropy contributions are limited to surface and subsurface atoms, with very small contributions for atoms deeper in the bulk. Applied to thin films of thickness t , this gives rise to the phenomenological anisotropy expression $K = K_S/t + K_V$. As a consequence, the competition of bulk and surfaces anisotropies may give rise to spin reorientation transitions as a function of t or temperature. The surface anisotropy permits to dramatically influence the magnetic properties by modifying or replacing the film-vacuum interface. This can be easily done by adsorbing molecules on the surface, as shown in Sec. 2.3.1.

If the 2D dimensionality of a thin film is further decreased, the atoms of the system are subject to a more severe loss of coordination. The increase of the orbital contribution to magnetic moment and of the anisotropy constant with decreasing dimensionality is shown in Table 2.1 as observed for the system Co/Pt. The increase of both these values is clear by passing from 2D to 1D and is much more marked if we reach the 0D case. In fact, X-Ray Magnetic Circular Dichroism (XMCD) studies on small Co clusters have shown a spectacular increase of orbital and magnetic anisotropy if the number of atoms is reduced from to 40 to one [Gambardella et al., 2003]. For a Pt-supported Co

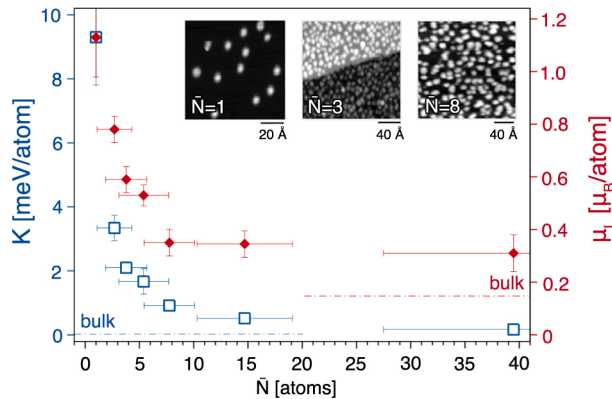


Figure 2.3: Magnetic anisotropy constant and orbital magnetic moment of Co clusters at the Pt(111) surface as a function of the mean number of atoms per island. In inset the corresponding STM images are also reported (figure adapted from [Gambardella et al., 2003])

adatoms the μ_L is eight times higher than the bulk value, while K is two order of magnitude larger. These values are significantly larger than the ones found in typical magnetic recording materials, such as Co/Pt multilayers and even larger of the permanent magnet SmCo₅ ($K \approx 0.3$ meV/at. and $K \approx 1.8$ meV/at. respectively).

The detailed understanding of the effects of coordination on the orbital momentum and the magnetic anisotropy will open new avenues for the design of nanostructures with promising magnetic properties.

2.2 Magnetization reversal in nanoislands

As discussed in the previous section, a sufficiently small magnetic island behaves as a single magnetic domain and the magnetization reversal proceeds by uniform rotation. In this case the magnetic behavior is usually described with the Stoner-Wohlfarth model. This model was also developed to depict the thermal activated reversal in a theory known as Néel-Brown model. Both these models are discussed in the first part of this section, then we will see how, on this basis, it is possible to describe the dynamical susceptibility of a particle assembly. In the last part, I will show some recent examples where the predictions of these models were not fulfilled. This highlights the need of a different approach to correctly describe magnetization reversal phenomena in nanometer size clusters.

2.2.1 The Stoner-Wohlfarth and the Néel-Brown models

The Stoner-Wohlfarth model is the simplest classical description of magnetization reversal [Stoner and Wohlfarth, 1948]. The basic assumption of this model is that the exchange energy holds all atomic spins parallel to each other, so that the magnetization magnitude does not vary inside the particle during the reversal. The dominance of exchange fixes the magnetization projections and the energy of the system can be treated by rotating the spin system as a whole. Thus, the N individual magnetic moments can be grouped together to build a giant magnetic moment called macrospin $\boldsymbol{\mu} = N\boldsymbol{\mu}_{\text{at}}$. Since the exchange energy remains unchanged, the competition in the energy of the system is limited to anisotropic and magnetostatic effects only. In the case of uniaxial anisotropy, where the easy axis is parallel to the external field $\mathbf{H} = H\hat{\mathbf{z}}$ (as in Fig. 2.4a), the magnetic energy is:

$$E = NK \sin^2\theta - N\mu_{\text{at}}H \cos\theta \quad (2.4)$$

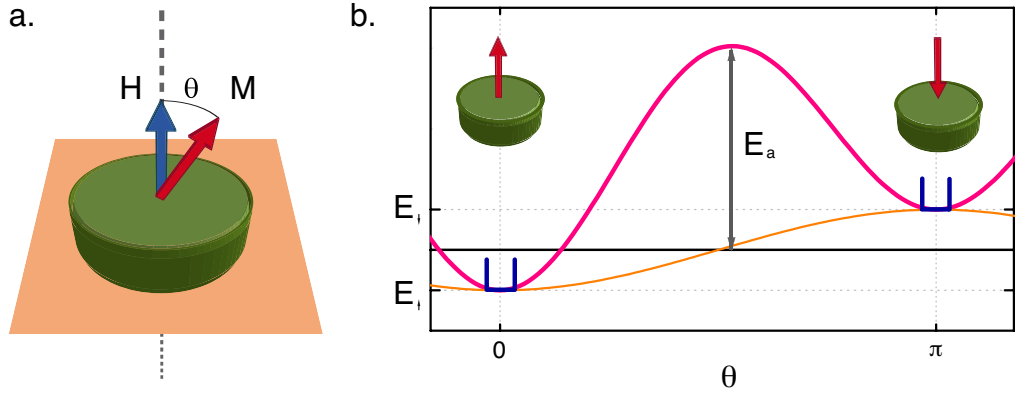


Figure 2.4: a. Schematic representation of a magnetic island on a surface island. This is characterized by uniaxial anisotropy ($K > 0$) with a out-of-plane easy axis. b. Representation of the total energy of the island according to the Eq. 2.4 together with its two limit cases: the Ising (blue) and Langevin (orange) model

where θ is the angle between $\boldsymbol{\mu}$ and $\hat{\mathbf{z}}$. K is an effective anisotropy constant that incorporates the contributions from magnetocrystalline, surface, magnetoelastic, and shape anisotropies. Fig. 2.4b shows the energy landscape for small H : two minima are presents at $\theta = 0$ and $\theta = \pi$, corresponding to the two possible magnetization states along the easy axis. When $T = 0$ K, depending on the sample history, the magnetization remains in the \uparrow state ($\theta = 0$ with energy E_{\uparrow}) or in the \downarrow state ($\theta = \pi$ with energy E_{\downarrow}). This causes hysteresis in the magnetization cycles. At the absolute zero, the magnetization reversal can be only field-induced. Indeed, by increasing H one of the two minima becomes shallow and vanishes when the applied field is opposite to the so-called anisotropic field:

$$H_{\text{an}} = \frac{2K}{\mu_{\text{at}}}. \quad (2.5)$$

A completely different process occurs if the system is heated up at finite temperature $T \neq 0$ K, since magnetization reversal can be thermally activated. The energy $k_B T$ should be sufficient to cross the barriers

$$E_{\uparrow\downarrow} = E_a - E_{\uparrow} = NK \left(1 + \frac{H^2}{H_{\text{an}}^2} \right) \quad \text{and} \quad E_{\downarrow\uparrow} = E_a - E_{\downarrow} = NK \left(1 - \frac{H^2}{H_{\text{an}}^2} \right). \quad (2.6)$$

where the energy barrier for $H = 0$ is:

$$E_a = N \cdot K. \quad (2.7)$$

To understand the magnetic behavior of the particle, we have now to properly describe the thermal fluctuations of its magnetic moment and how it decays

towards equilibrium. First of all, depending on the magnitude of $k_B T$ with respect to E_a , we can identify two limit cases. If $k_B T \gg E_a$ all the macrospin orientations are equiprobable (Langevin model), the magnetic behavior is like that of an ensemble of paramagnetic atoms but with macrospin, for this reason is called superparamagnetism. If $k_B T \ll E_a$ the macrospin has only two possible orientations: $\theta = 0$ and $\theta = \pi$ (Ising model). In this discrete orientation context, Néel could describe how the system can escape from one state to the other by thermal activation over the barrier [Néel, 1949]. The switching rate ν follows an Arrhenius law:

$$\nu = \nu_0 e^{-\frac{E_a}{k_B T}}. \quad (2.8)$$

where ν_0 is an attempt frequency of the order of 10^{+10} Hz [Wernsdorfer et al., 1997]. Equivalently, the lifetime between switching events is $\tau = \tau_0 \exp(E_a/k_B T)$. The problem was then reexamined more rigorously by Brown who treated the system as a gyromagnetic one [Brown, 1963]. He considered that the macrospin $\boldsymbol{\mu}$ (or the magnetization vector \mathbf{M}) of a particle wiggles around an energy minimum, then jumps to the vicinity of the other minimum and then wiggles around there before jumping again. The natural starting point for a formal description of the relaxation dynamics of a gyromagnetic system is the Landau-Lifshitz-Gilbert equation:

$$\frac{d\boldsymbol{\mu}}{dt} = \gamma_0 \mathbf{H}^{\text{eff}} \times \boldsymbol{\mu} - \alpha \boldsymbol{\mu} \times \frac{d\boldsymbol{\mu}}{dt} \quad (2.9)$$

where γ_0 is the gyromagnetic ratio and α is the Gilbert damping factor. The effective field $\mathbf{H}^{\text{eff}} = \partial E / \partial \mathbf{M}$ includes the influence of exchange, anisotropy and dipolar fields. If we consider a single particle we must add an additional term $\mathbf{h}(t)$ that describes rapidly fluctuating random forces and whose statistical average is zero. Since the spectrum of these forces can be regarded as white up to frequency of the order of 10^{-13} s (orders of magnitude lower than the response time of a single particle, that is of the order of 10^{-10} s), the effect of temperature can be considered as a purely random process. The components of the random field $h_i(t)$ are characterized by the correlation functions:

$$\langle h_i(t) \rangle = 0, \quad \langle h_i(t) h_j(t+t') \rangle = (2k_B T \alpha / \gamma_0 \mu_0 \mu_{\text{at}}) \delta_{ij} \delta(t') \quad (2.10)$$

where V is the volume of the particle. The assumption that noise is uncorrelated in time permitted to Brown to obtain a Fokker-Planck equation to describe the distribution of magnetization orientations. Unfortunately, this does not have an analytical general solution. Nonetheless, if the particle has an axial symmetry, within the high-energy barrier approximation ($k_B T \ll E_a$) it is

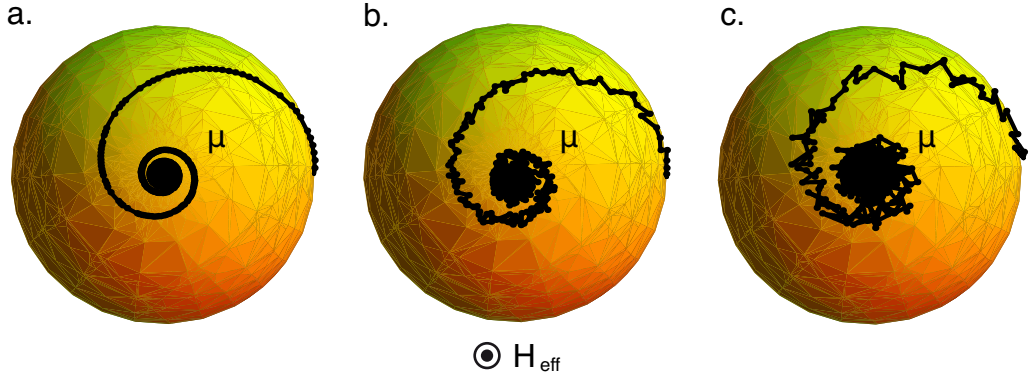


Figure 2.5: Schematical illustration of the relaxation dynamics of the magnetic moment according to the Landau-Lifshitz-Gilbert equation where the effect of the temperature is included by adding a random field. The temperature is gradually increased from a. (T) to b. ($2T$) to c. ($4T$).

possible to find an exact analytical solution:

$$v = \frac{\alpha\gamma_0}{1 + \alpha^2} \sqrt{\frac{N\mu_{\text{at}}H_{\text{an}}^3}{2\pi k_{\text{B}}T}} e^{-\frac{E_{\text{a}}}{k_{\text{B}}T}} = v_0 e^{-\frac{E_{\text{a}}}{k_{\text{B}}T}}. \quad (2.11)$$

As can be seen, Eq. 2.8 is recovered and thus we referred to this equation as Néel-Brown law.

2.2.2 Dynamical susceptibility of a particle assembly

The Néel-Brown law is in every respect a transition state theory. If we are at the thermodynamical equilibrium the Boltzmann distribution $\exp(-E/k_{\text{B}}T)$ describes the occupation probability of the states, that is to say, the probability for a single macrospin to be oriented in a certain direction. By using Eq. 2.4, we can thus write the partition function of the system and finding an analytical expression for the equilibrium susceptibility of a single nanoparticle [Fruchart et al., 2002]:

$$\chi_{\text{SW}}^{\text{eq}} = \left(\frac{\partial \mu_z}{\partial H} \right)_{H=0} = N^2 \mu_{\text{at}}^2 \left[-\frac{1}{2K} + \frac{e^{\frac{E_{\text{a}}}{k_{\text{B}}T}}}{\sqrt{\pi} E_{\text{a}} k_{\text{B}} T \text{Erfi}(\sqrt{\frac{E_{\text{a}}}{k_{\text{B}}T})}} \right]. \quad (2.12)$$

In the limit cases of Langevin and Ising models, the equilibrium susceptibility follows simpler expressions [Rusponi et al., 2003]:

$$\chi_{\text{iso}}^{\text{eq}} = \frac{N^2 \mu_{\text{at}}^2}{3k_{\text{B}}T}, \quad (2.13)$$

$$\chi_{2L}^{\text{eq}} = \frac{N^2 \mu_{\text{at}}^2}{k_B T}. \quad (2.14)$$

The decay of $\chi_{\text{SW}}^{\text{eq}}$ is slightly steeper than $1/T$ and with increasing temperature it goes from the Ising susceptibility to the Langevin one, in accordance with the validity of the two limit cases.

Up to now we have considered a particle in thermodynamical equilibrium. However, we have to take into account that the time needed by a particle to reach equilibrium is of the same order of magnitude than the period of the oscillating magnetic field in a typical magnetic measurements. This non-equilibrium situation can be described in the frame of the Linear Response Theory [Zagoskin, 1998]:

$$\chi = \chi^{\text{eq}} f(\omega\tau) = \chi^{\text{eq}} \frac{1}{1 - i\omega\tau}. \quad (2.15)$$

The dynamical susceptibility can thus be expressed in terms of the equilibrium susceptibility χ^{eq} , by taking into account the kinetic pathway to cross the anisotropy barrier with the factor $f(\omega\tau)$. In this way we have defined a complex dynamical susceptibility: $\chi(T) = \chi'(T) + i\chi''(T)$, where the imaginary part χ'' is associated to dissipative processes that arise when the system is out of equilibrium. The real part represents the magnetic susceptibility defined as $(dM/dH)_{H=0}$. In the Stoner-Wohlfarth and in the Ising models the real part of the dynamical susceptibility takes the form, respectively:

$$\chi'_{\text{SW}} = \left(\frac{\partial \mu_z}{\partial H} \right)_{H=0} = N^2 \mu_{\text{at}}^2 \left[-\frac{1}{2K} + \frac{e^{\frac{E_a}{k_B T}}}{\sqrt{\pi} E_a k_B T \text{Erfi}\left(\sqrt{\frac{E_a}{k_B T}}\right)} \right] \frac{1}{1 + \omega^2 \tau^2}, \quad (2.16)$$

$$\chi'_{2L} = \frac{N^2 \mu_{\text{at}}^2}{k_B T} \frac{1}{1 + \omega^2 \tau^2}. \quad (2.17)$$

In Fig. 2.6a the temperature behavior of the equilibrium and dynamical susceptibilities according to the different models is shown.

According to the value of $f(\omega\tau)$, the particle is in a blocked state or in a superparamagnetic state. It is practical to define a blocking temperature T_B where the transition between these two behaviors occurs. This happens when $f(\omega\tau)_{T=T_B} = 1/2$, i.e. $\omega\tau = 1$:

$$T_B = \frac{E_a}{k_B \ln(v_0/\omega)}. \quad (2.18)$$

Until now we considered a single particle. In the case of an assembly of particles we have to take into account the fact the activation energy for thermal reversal can change from a particle to another, due to their different size,

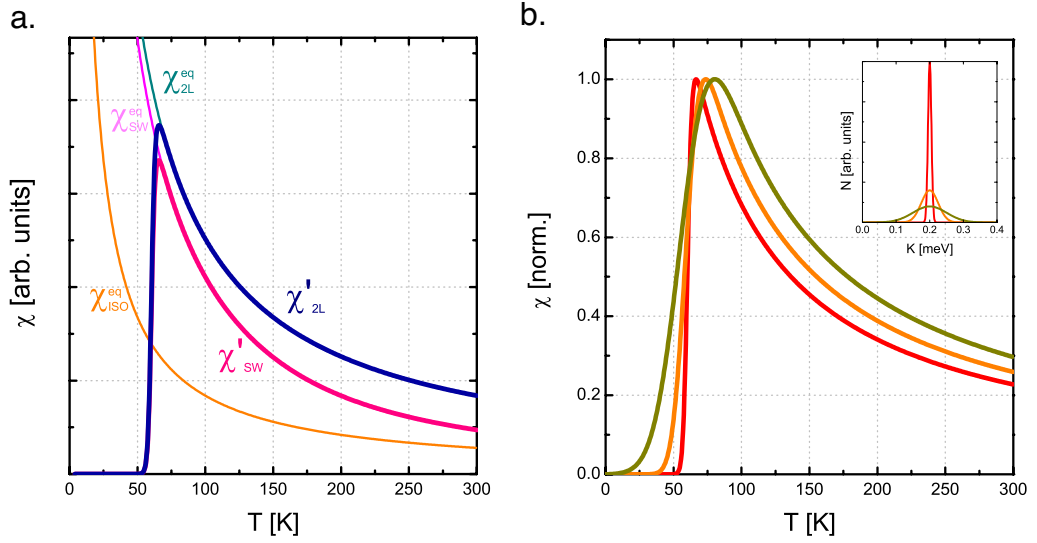


Figure 2.6: a. Different models for equilibrium and dynamical susceptibilities of a single magnetic nanoparticle. b. Dynamical susceptibilities of a particle assembly with different magnetic anisotropy distribution: $\sigma/\bar{K}=0.025$, 0.125 and 0.25 . The following parameters were used: $\bar{K}=0.2$ meV/at. $N=300$, $\mu_{\text{at}}=1.9 \mu_{\text{B}}$, $\omega=1$ Hz and $\tau_0 = 10^{-10}$ s.

shape, orientation, etc. To take into account this statistical distribution over $E_a = NK$, we have considered the case of an assembly of particles monodispersed in size ($N = \text{cst}$) but characterized by a gaussian distribution of magnetic anisotropy K (with mean \bar{K} and standard deviation σ). The total susceptibility is then:

$$\chi_{\text{tot}} = \sum_K \chi(K) \frac{e^{-\frac{(K-\bar{K})^2}{2\sigma^2}}}{\sqrt{2\pi}\sigma} \quad (2.19)$$

Evidently, the most adequate description of the distribution of the activation energy would include also a gaussian distribution over N . However, since it is impossible to correlate properly the distributions of K and N , we are obliged to limit our modelization to the presented case. The effect of an increasing anisotropy distribution is shown in Fig. 2.6b.

2.2.3 Beyond the macrospin model

The macrospin model is appealing due to its simplicity and for this reason most experiments are discussed through it. The predictions of this model were confirmed for individual ferromagnetic nanoparticles ($d = 15 \div 30$ nm) of Ni, Co, and Dy at very low temperatures ($T = 0.1 \div 6$ K) where waiting time,

switching field and telegraph noise measurements were all coherent with the Néel-Brown model [Wernsdorfer et al., 1997]. However it remains an ideal model for the majority of nanostructures, and many measurements are not consistent with its predictions. As we have seen in Sec. 2.2.1, the small size is the main criterion of validity of the macrospin model: this assures that all spins are held tightly parallel to each other, leading to a monodomain configuration at zero temperature (Stoner-Wohlfarth model) and to a magnetization reversal by uniform rotation when the temperature is increased (Néel-Brown model).

Even in a particle whose size is few nanometers in diameter, the dominant role of surfaces can cause deviation from the Stoner-Wohlfarth model. For example, in small clusters ($d = 2 \div 8$ nm) of ferrimagnetic oxides like $\gamma - \text{Fe}_2\text{O}_3$ surface spin frustration induces some important deviation to the macrospin model, such as the absence of magnetization saturation at low temperature in high magnetic fields [Tronc et al., 2003]. The magnetic properties are in this case dictated by the competition between the surface and the core atoms. Also in the case of metallic nanoparticles, the large increase of magnetic anisotropy observed when the clusters are made up only of few atoms [Gambardella et al., 2003] demands to take in a deeper account the consequences of symmetry breaking at the surface. The surface seems to play a fundamental role even when the number of atoms inside the particles a few order of magnitude larger than surface atoms. For example, micro-SQUID measurements on a single Co nanoparticle (composed of more than 1000 atoms, $d = 3$ nm) have shown that by following the Stoner-Wohlfarth model the magnetic anisotropy can be ascribed only to the interface term [Jamet et al., 2001]. A even more spectacular example of inhomogeneous anisotropy distribution was reported by Rusponi *et al.* in the case of Co nanoparticles with different shapes grown on Pt(111) [Rusponi et al., 2003]. Assuming a coherent reversal of magnetization, the fits of MOKE measurements induced the authors to confine the magnetic anisotropy mainly to perimeter atoms (enhanced edge anisotropy). All those experiments raises a question: it is rightful to build a macrospin if we are in presence of such inhomogeneous anisotropy distributions? In the case of enhanced edge anisotropy the answer to this question came from atomic scale micromagnetic calculations of the magnetic configurations on Co nanoparticles at zero temperature [Rohart et al., 2007]. The results show that the macrospin model is oversimplified for particles with diameter as low as 2 nm, since inhomogeneous (twisted) magnetic configurations arise that cause significant reductions to the switching field.

If the nanoparticle is heated up to finite temperature and even if the ground state configuration is homogeneous, magnetization can reverse with non-uniform modes (for example by curling or by nucleation and propagation of domain

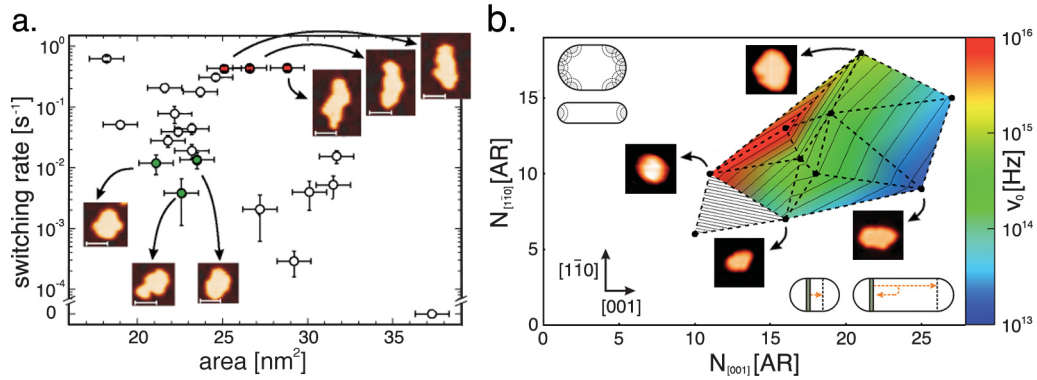


Figure 2.7: a. Plot of the switching rate versus the area of individual particles of Fe on Mo(110), showing a shape-dependent crossover attributed to domain-wall assisted reversal (figure extracted from [Bode et al., 2004]). b. Arrhenius prefactor ν_0 as a function of Fe island length on W(110), nearly all data points lie on a plane (colored part). In the insets a schematic interpretation for this trend is shown (figure adapted from [Krause et al., 2009]).

walls [Wernsdorfer, 2001]). Thus, the limitations of the Néel-Brown model are even tighter than those of Stoner-Wohlfarth model. For particles with a reduced size but with a higher aspect ratio, the magnetization reversal could not be explained with a coherent rotation model. Indeed, the Hall magnetometry measurements of switching fields of elongated Fe nanoparticles ($d = 9 \div 20$ nm, $h = 50 \div 250$ nm) gave values smaller with respect to the predictions of the Néel-Brown model [Wirth et al., 2000]. The authors proposed also that the magnetization reversal is nonuniform and is thermally activated within a nucleus of critical volume.

Further insights into the comprehension of magnetization reversal has been made thanks to Spin-Polarized STM studies, since the measurements can be performed on single nanoparticles. The results of these SP-STM measurements showed that even for very small magnetic nanoparticles the magnetization reversal can be rationalized only by overcoming the Néel-Brown model. For example, in the case of Fe monolayer islands consisting of $200 \div 600$ atoms ($d = 4 \div 7$ nm) deposited on Mo(110) substrate, the switching behavior was found to critically depend on the shape and the size of the particles [Bode et al., 2004]. In particular, slightly elongated (aspect ratio lower than 1:4) Fe nanoparticles switch around two order of magnitude more rapidly than compact islands of the same volume (Fig. 2.7a). This result was explained by assuming two different reversal modes in the two cases: coherent switching for compact islands and domain wall formation for elongated islands. A succes-

sive more detailed study of a slightly different system (Fe nanoparticles on W(110), $d = 4 \div 7$ nm) combined with Monte-Carlo simulations strengthened this hypothesis [Krause et al., 2009]. The advantage of this system consists in the fact that the direction of Fe magnetization easy axis is well defined and lies along the $[1\bar{1}0]$ direction of the W substrate. The linear scaling of E_a with the number of atoms in the easy axis direction could indicate that the reversal takes place via nucleation and propagation of domain walls. Moreover it should be pointed out that even the dependence of the attempt frequency ν_0 on the island shape seems to confirm that reversal proceed via domain-wall motion. Indeed, when the particles are elongated along the hard axis the probability for the domain wall to successfully propagate decreases, since it is more likely that the domain wall returns to its nucleation sites and annihilates there with no net magnetization reversal. On the other hand, if the particles are elongated along the easy axis the number of domain-wall nucleation sites augments, increasing the probability of magnetization reversal (Fig. 2.7b). In conclusion, it is not straightforward to build a consistent picture of the macrospin limit. It is necessary to establish under which conditions the macrospin model can be applied and to adopt a new approach to consider reversal modes more complicated than coherent rotation. Only in this way the contradictory experimental observations reported here can be really understood: this knowledge is of fundamental importance to overcome the superparamagnetic limit.

2.3 Magnetism of hybrid and molecular systems

Nanomagnetism is a rich field that opens many new opportunities. However the electronic and magnetic properties of nanostructures can be additionally tuned by exploiting the infinite possibilities offered by chemical routes. Hybrid and molecular systems could thus show new peculiar phenomena together with opening new perspectives to understand the underlying physics. These systems are already proposed as promising candidates to substitute inorganic materials in specific applications.

2.3.1 The impact of molecular adsorbates on nanomagnetism

In Sec. 2.1.2 we recalled the decisive importance of the surface in determining the magnetic behavior of ultra-thin films. Thus, one can foresee that a con-

control over the surface would permit to artificially tune the magnetic properties of nanostructures to obtain the desired behavior. The feasibility of this route was shown by controlling the magnetization direction of thin films with small gas molecules. Upon adsorption, the balance of the different anisotropy contributions is perturbed and a Spin-Reorientation Transition (SRT) is induced. In this field Ni/Cu(001) can be considered a prototype system that exhibit a so-called reverse spin-reorientation transition: magnetization passes from in-plane to out-of-plane at a critical thickness ($d_C \approx 10 \div 11$ ML). Upon H₂ adsorption this reorientation occurs at a lower thickness, implying a reduction of the absolute value of the surface anisotropy [Vollmer et al., 1999]. In a successive study, the reorientation was demonstrated to be reversible, and this leads to an oscillatory sequence of in-plane and perpendicular magnetization when hydrogen coverage is made oscillate (Fig. 2.8a). Moreover, the observed dilatation of the top-most layer upon H adsorption permitted to explain the reduction of the magnetic surface anisotropy, since the uniaxial distortion that favors out-of-plane magnetization is reduced [Sander et al., 2004]. The proposed connection between surface relaxation and magnetic anisotropy is expected to be of general validity, as partially confirmed by an O₂ adsorption study. In this case, first principles calculations reveal that the change of magnetic anisotropy is due to lattice relaxation, together with the appearance of an O-induced surface state [Hong et al., 2004]. Conversely, in another XMCD study, the reduction of surface anisotropy is ascribed to the quenching of orbital moments induced by the molecular adsorption, according with a simple model that permits to explain the difference in the ratio orbital/spin moment in the cases of H and CO adsorption [Matsumura et al., 2002]. The adsorption of O₂ and CO lowers the critical thickness for SRT to occur also on Fe and Co thin films [Peterka et al., 2002; Matsumura et al., 2002].

The physisorption of small gas molecules has thus a marked impact on the magnetism of thin films, and the chemisorption of reactive species is expected to alter even more profoundly their electronic and magnetic properties. However, only few studies have been reported so far about the changes in the properties of ferromagnetic thin films induced by molecular chemisorption. For example, the theoretical and experimental studies of the adsorption of sulfur on Co and Fe surfaces were mainly intended to understand issues like the reduction of adhesive strength [Nelson et al., 2005] or the poisoning of catalytic activity [Lahtinen et al., 2005]. Nonetheless, the influence on the magnetic properties is clear already from these results: in the case of Co surface, *ab initio* calculations show that the magnetic moment of the nearest atoms is significantly decreased, while the one of the next nearest atoms are slightly increased. Moreover a little magnetic moment is induced on S atoms, that ferromagnetically couples with the substrate [Lahtinen et al., 2005; Ma et al.,

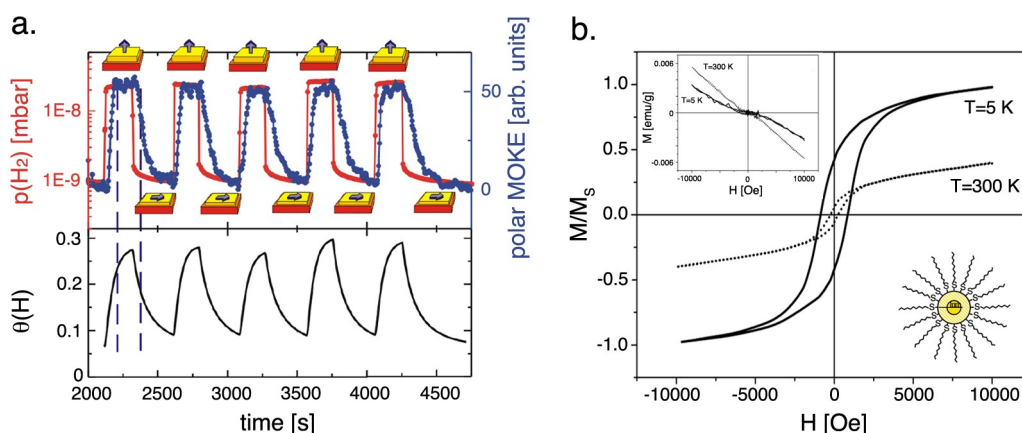


Figure 2.8: a. H induced variation of the polar MOKE signal of 8 ML Ni film, together with the hydrogen partial pressure and adsorption, calculated by taking into accounts the dynamics of the process (figure adapted from [Sander et al., 2004]). b. Hysteresis loops corresponding to the gold thiol-capped nanoparticles. For a comparison, in the inset are shown hysteresis loops for thiol-free nanoparticles (figure adapted from [Crespo et al., 2004]).

2008]. Similar results are obtained also if methanethiol is adsorbed on Co surface.

The effect of molecular adsorption on the properties of the dilute magnetic semiconductor (Ga,Mn)As has also been object of study. In this case depending on the organic molecules adsorbed on the surface different changes in magnetism were observed. Indeed, a phosphate-bound molecules were found to suppress ferromagnetism [Kreutz et al., 2006] while, in contrast, carboxyl- and sulfur-bound molecules enhanced magnetization [Carmeli et al., 2006]. The most extensive studies of the effects of chemically adsorbed molecules on magnetism has been carried out so far on diamagnetic substrates. In this field, the research was boosted by the apparition of magnetism ex-nihilo when thiols are assembled around gold nanoparticles, which then show hysteresis up to room temperature and an enormous value of magnetic anisotropy (Fig. 2.8b) [Crespo et al., 2004].

2.3.2 Magnetism of metal-organic frameworks

The use of chemical bondings to modify and control magnetic properties motivates also a wide spread research about the magnetism of metal-organic frameworks. In this case the approach is slightly different, since each single atom is surrounded with molecular ligands to build structures that can reach

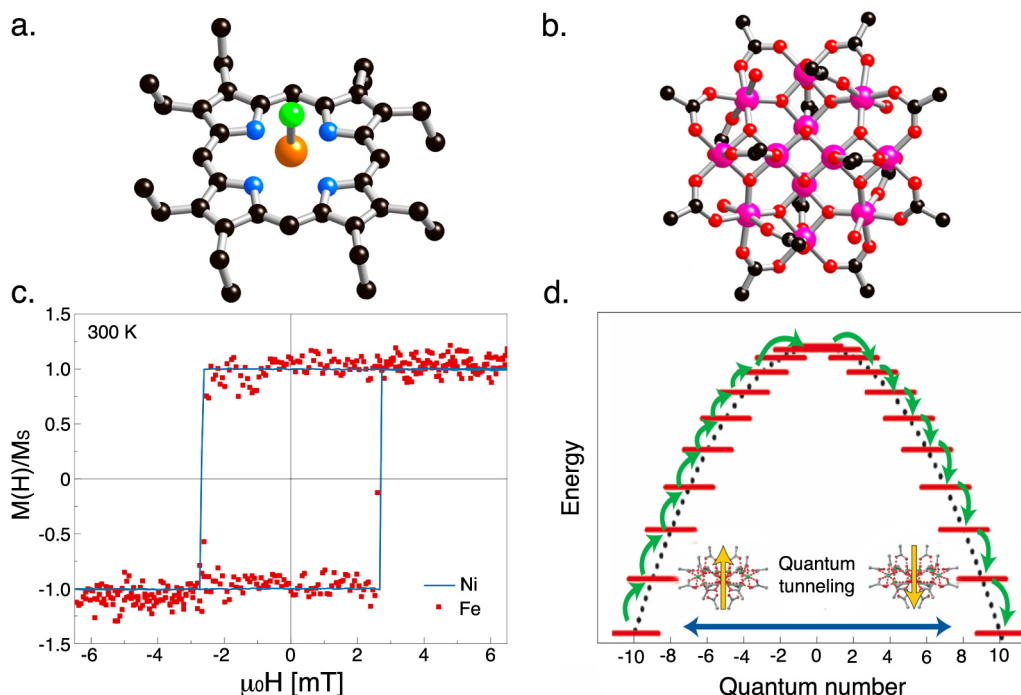


Figure 2.9: Some example of metal-organic frameworks: a. octaethylporphyrin Fe(III) chloride and b. molecular magnet Mn_{12} acetate. c. Element specific hysteresis loops of the porphyrin iron ion when this is deposited on Ni; the coincidence of the two loops indicates that Fe is ferromagnetically coupled with the substrate (figure extracted from [Wende et al., 2007]). d. Schematic representation of the energy landscape of a molecular nanomagnet with a spin ground state $S=10$ (figure extracted from [Bogani and Wernsdorfer, 2008])

high complexity. In the simplest case each molecule carries a single metal ion, like for porphyrin or phtalocyanine (Fig. 2.9a): this can be considered as archetypal metallorganic complexes thanks to their activity in many biochemical processes. The organic coordination changes completely the properties of the ion. This was clearly shown in the case of Co phalocyanine on Au(111) [Zhao et al., 2005]. In this case the Co ion does not interact with conduction electrons and exhibit no Kondo effect. However, after dehydrogenation of the ligand by voltage pulses from a STM tip, the Kondo effect is recovered. Interestingly, when porphyrins are deposited on Ni or Co a substantial ferromagnetic exchange couples the magnetic moment of the metal ion (Mn or Fe) with the substrate, and the molecular layer orders ferromagnetically (Fig. 2.9b) [Scheybal et al., 2005; Wende et al., 2007]. Molecular ligands can also be used to build supramolecular assembly in which the atomic spins

can be regularly ordered in a 2D array. Moreover, the direction of magnetic anisotropy of the Fe atoms in the array can be controlled, since it can be oriented from in-plane to out-of-plane upon O₂ adsorption [Gambardella et al., 2009].

If the complexity of the framework is increased, within the same molecule several metal centers can be bound together. In this way, a so-called single-molecule magnet or molecular nanomagnet is obtained. The most prominent example is a dodecanuclear manganese-oxo cluster with acetate ligands, shortly called Mn₁₂ acetate (Fig. 2.9c). Molecular nanomagnets display a variety of shapes and sizes. By selective substitutions of the ligands it is possible to alter the coupling with the environment. As cited at the beginning of the chapter, the magnetic behavior of this system shows some new quantum features. For example, the energy of the spin levels shows a double well shape and in order to reverse the magnetization it is necessary to overcome the energy barrier by climbing up and down all the energy levels (Fig. 2.9d). However, at certain resonance fields, levels of positive and negative spin quantum numbers are degenerate and quantum tunnel can occur [Bogani and Wernsdorfer, 2008]. This is at the origin of the steps in the hysteresis loops.

2.3.3 Organic spintronics

The interest in molecular materials is nowadays increasing since they are particularly attracting for building spintronic devices. As in the wider field of molecular-electronics, replacing inorganic materials with molecular ones opens the way to cheap, low-weight, mechanically flexible, and chemically interactive electronics. Moreover, the endless possibilities of chemical synthesis and end-groups engineering give good expectations for new concept devices. The entry of the spin in the realm of molecular electronics is more recent and has an additional fundamental reason. Light elements, like carbon, have a very low atomic numbers (Z) and thus a weak spin-orbit interaction (proportional to Z^4). Therefore, in organic semiconductors the spin-scattering mechanism is very weak and the spin polarization of the charge carriers can be maintained for a very long time (called spin relaxation time τ_S). In inorganic materials $\tau_S \approx 10^{-13} \div 10^{-8}$ s while for organic materials $\tau_S \approx 10^{-6} \div 10^{-1}$ s [Szulczewski et al., 2009]. The fervor of research in organic spintronics is essentially due to this reason [Naber et al., 2007; Dediu et al., 2009].

The pioneering spin valve effect in molecular materials was demonstrated for the first time in multi-walled carbon nanotubes [Tsukagoshi et al., 1999] and then in the organic semiconductor sexithiophene [Dediu et al., 2002]. The large spin diffusion length observed (a few hundreds nm) suggested immediately a potential application in devices and encouraged further research in

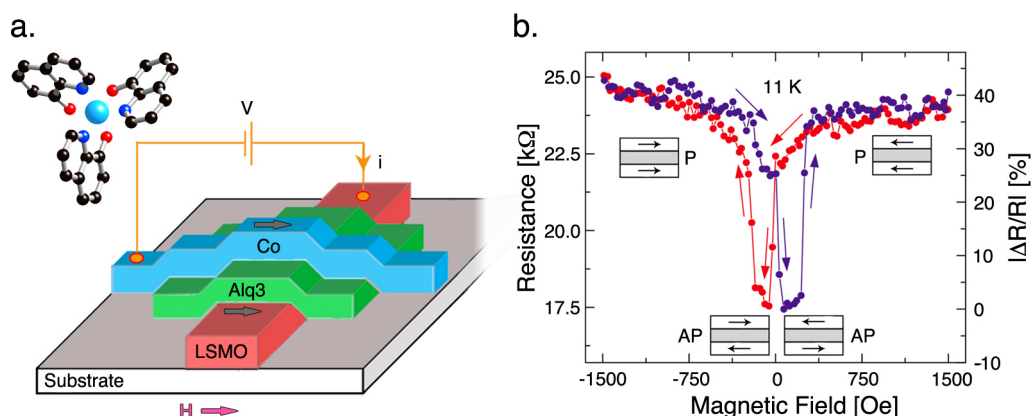


Figure 2.10: a. Representation of the vertical spin-valve device with Alq₃. b. Magneto-resistance loops showing the inverse spin valve effect.

this field Hueso et al. [2007]. Ever since, most of the studies have been focused on Alq₃ (*tris* [8-hydroxyquinoline] aluminium) motivated by the achievement of a sizeable inverse spin valve effect [Xiong et al., 2004]. While the interest in spin injection and long-distance spin transport was growing, several groups also started to explore the possibilities of using these materials as spin-tunnel barriers. For example, in Ni/octanethiol/Ti/Ni tunnel junction the observation of spin-polarized tunnelling is peculiar to the presence of the monolayer barrier [Petta et al., 2004]. More recently, very large (up to 300%) tunnel magneto-resistance was detected at low temperature in a La_{0.7}Sr_{0.3}MnO₃/Alq₃/Co nanosized tunnel devices where only few molecules cover the interface with the electrodes [Barraud et al., 2010]. The results of this study highlight the dominant role of the metal/organic interface. In particular, the metal induces in the first molecular layer localized polarized states that can change completely the magnetoresistance of the organic spin valve. By adequately combining ferromagnetic metals and molecules, one could use the metal/molecule coupling to tailor the properties of spintronics devices, opening the doors of a field futuristically called spinterface [Sanvito, 2010]. The work of Barraud et al. is the first one that tries to explain some of the discrepancies emerged in organic spintronics (like the inverse magnetoresistance in Alq₃), that still remains a poorly understood phenomenon. Only a deeper understanding of the magnetic properties of the organic/inorganic interface will permit to engineer more performant spintronic devices.

Experimental Methods

The present chapter focuses on the experimental techniques used in this work. The ultra high vacuum apparatus is briefly described in the first section, with a particular attention to the sample preparation and the growth of thin films. In the second section, scanning probe microscopies techniques are presented; the physical principles and the capabilities of STM and AFM are briefly discussed. Finally, the last section is devoted to the basics of MOKE and the experimental setup used to study the magnetism of ultra-thin films and nanoparticles.

3.1 UHV apparatus

Ultra High Vacuum is a prerequisite for the most of the surface preparation procedures, for surface analysis techniques and thin film growth. The main reason is the need for maintaining a surface clean over several hours. During this period, surfaces and thin films are free of defects and contamination, well ordered and their properties can be well characterized. The UHV apparatus used during this thesis work is shown in Fig. 3.1. Two turbo-molecular pumps and their respective backing rotary vane pumps allow to pump the chamber from atmospheric pressure down to high vacuum (10^{-7} mbar). Three ion sputter pumps and two titanium sublimation pumps permit then to achieve the UHV regime. This vacuum pumping system assures a base pressure inside the apparatus lower than 10^{-10} mbar. It is worth to point out that after air exposure it is necessary to bake-out the whole system (typically at 140 °C for 16

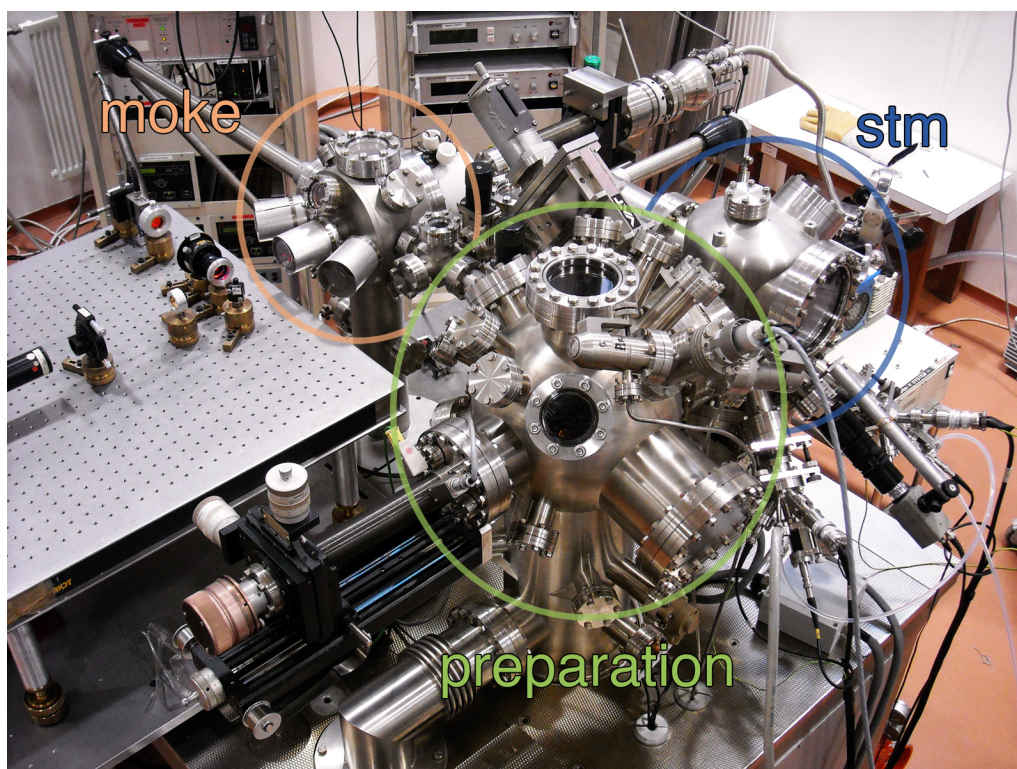


Figure 3.1: Picture of the UHV experimental apparatus used during this thesis work. The three main chambers are highlighted.

h) in order to achieve such a base pressure.

As highlighted in the figure, the apparatus is made up of three different chambers plus a smaller fast entry lock chamber for sample introduction. The first chamber is dedicated to the preparation of the sample. To this purpose, it is equipped with a sputter ion source for crystal surface cleaning (in the energy range from 300 to 5 keV) and a resistive pyrolytic boron nitride (PBN) heater for sample annealing at temperatures up to 900 °C. STM is housed in its own chamber, bolted directly onto the preparation chamber; this is also equipped with two electron beam evaporators (for cobalt and platinum) that allow to grow nanoparticles thin films directly on the STM stage. Finally, the third chamber is designed for the study of the sample magnetic properties by MOKE.

3.1.1 Sample Preparation

The principal substrate used during this thesis work is Au(111) single-crystal. High purity (99.999%) gold single crystals are commercially available and were purchased from MaTecK¹ or Surface Preparation Laboratory². They look like small disks with a typical surface of 1 cm². Au single crystals are grown by Czochralski method and subsequently cut to specific orientations and shapes. X-ray diffraction, combined with several cycles of mechanical lapping and polishing of the surface, permits to obtain a precise sample orientation. The sample are fixed on molybdenum sample holder with spot-welded tantalum foils.

Once the sample is introduced in the UHV apparatus, an atomically clean surface can be obtained with several cycles of ion bombardment followed by annealing. The cleaning procedure starts by admitting a noble gas, in our case Ar, into the preparation chamber to reach a pressure of 2×10^{-6} mbar. A discharge of the ion sputter gun produces electrons that ionize Ar atoms. The ions are then accelerated by a voltage of 900 V towards the sample surface, creating a current of few $\mu\text{A}/\text{cm}^2$. Here, contaminants (and usually the top-most atomic layers of the crystals as well) are sputtered off by the impact with Ar ions. The duration of the bombardment depends on the history of the sample, but it is usually between 10 and 30 min. A subsequent annealing is necessary to remove the embedded and absorbed Ar atoms and to recover the surface crystallography. Typically, this is done by resistive heating at 450 °C for 15 min. It is possible that during this heat treatment further impurities from the bulk diffuse to the surface, so that ion bombardment/annealing cycle has to be repeated several times.

In this work it has been necessary also to clean films only few nanometers thick (as described in Sec. 4.1.2.1). In this case the ion bombardment has to be leaded with care to preserve the topmost layer as long as possible. In this case short bombardment time at grazing incidence have been used (typically for 30 s with an incidence angle $\alpha = 45^\circ$). Moreover, the annealing requires a higher temperature (around 650 °C) to be effective.

3.1.2 Metal Deposition

The deposition of metals has been realized by thermal evaporation. This consists in heating the source above the melting point to reach a vapor pressure sufficient to obtain a vapor beam. This is then spread into the vacuum chamber towards the substrate surface. Regarding the metal sources, resistance

¹<http://www.mateck.de>

²<http://www.spl.eu>

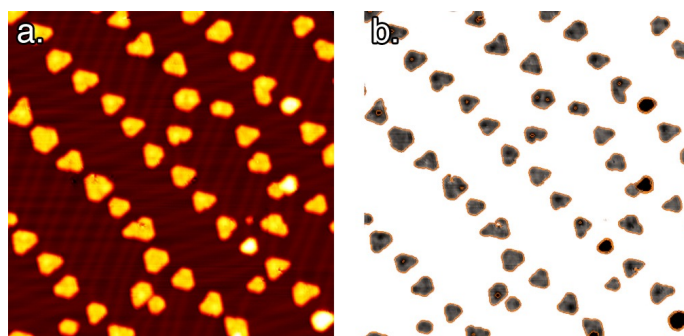


Figure 3.2: Procedure used to evaluate the covered area. a. STM image of a submonolayer deposit. b. Threshold filtering was performed using the WSxM flooding routine.

heated ones are restricted to materials with moderate melting points because of possible reactions between the melt and the resistance carrier and its temperature limitations. This disadvantage can be avoided by using an e-beam evaporator, where the temperature rise is induced by a bombarding electron beam. In this way the evaporation is characterized by a high degree of cleanliness with only slight increases of the background pressure. To this purpose, the evaporation cell is also enclosed in a water-cooled copper cylinder. With this technique a wide variety of materials (including refractory metals) can be evaporated with thickness from sub-monolayer up to multilayers, controlling the deposition time with a manual shutter placed between the sample and the source. A high precision over the final film thickness is possible thanks to a flux monitor that enables a real time control over the deposition rate. This is precalibrated on the basis of STM images of sub-monolayer deposition. By using the flooding routine implemented in the WSxM software [Horcas et al., 2007], it is determined the percentage of area above a selected threshold for a given STM image. The threshold was chosen just below the nanoislands height to reduce tip convolution artefacts (as shown in Fig. 3.2). On this basis the coverage is determined, assuming a pseudomorphic growth with the substrate and no intermixing. As mentioned, the main problem in such a procedure comes from tip convolution that induces an overestimation of the coverage, the error in this procedure is around 20%. It has to be remarked that even if the absolute error is significant, the relative one is less important. The error in determining the coverage can thus be minimized by repeating the calibration with several deposition times.

Cobalt and platinum are evaporated from high purity (99.999%) rods (2 mm

diameter) commercially available from Goodfellow³. Typical flux rates are 0.2 ML/min and 0.02 ML/min for Co and Pt respectively.

3.1.3 Molecule Deposition

In principle the deposition of molecules does not require UHV like for metals. However, for fundamental purposes the growth of thin molecular film is often studied in UHV which guarantees a high chemical and structural control. An important exception is represented by self-assembled monolayers, that are commonly prepared by immersing a freshly prepared or clean substrate into a dilute solution. Even if the formation of monolayers in vacuum from the gas phase has proven to be useful for studying the early stage dynamics of self assembly, UHV constitute a necessary environment only in special circumstances, such as, for example, if we want to deposit monolayer on Co islands or thin films, since cobalt is readily oxidized when exposed to air.

In the literature, the growth of SAMs in vacuum is usually carried out by introducing molecular vapors into the pumped chamber through a leak valve. As a result of the exposure, also the chamber interior surfaces are contaminated with molecules and must be cleaned with oxygen plasma [Poirier et al., 2001]. To avoid this disadvantage we have developed a new simple and small molecular evaporator, shown in Fig. 3.3a. It consists of a molybdenum sample plate, where we mechanically fixed a wrapped thoriated tungsten filament and a stainless steel electrical contact, that permits to connect the filament with the direct current heating facility of the sample heater. The molecules

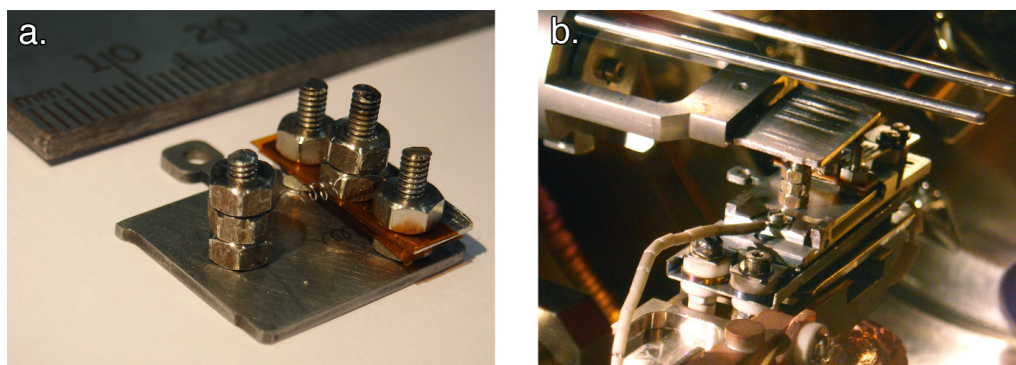


Figure 3.3: a. Picture of the molecular evaporator developed during this thesis work. b. Picture of the setup when molecules are evaporated on the sample.

³<http://www.goodfellow.com>

(in our case 1-dodecanethiol: $C_{12}H_{25}SH$) were absorbed on the filament by dipping it into the pure thiols that once in UHV are desorbed by heating the filament with a 0.3 A current, corresponding to a temperature of about 300 °C. During the evaporation the sample surface is put in proximity of the filament, as shown in Fig. 3.3b.

This technique permits to limit the contamination and the increase in the background pressure. Moreover the evaporant molecules can be changed or recharged rapidly. On the other hand, the main limitation of this method consists in the difficulty to control the deposition rate and hence the final molecular coverage.

3.2 Scanning Probe Microscopies

Scanning Probe Microscopies (SPMs) are a class of tools that scan a sharp probe tip across a sample and, by controlling the interaction between the two, are capable to provide information concerning the sample. The difference between the various techniques relies on the physical origin of this interaction. The versatility of scanning probe microscopies has permitted their use in many different scientific disciplines ranging from materials science to biology. Due to the ability to image and manipulate the surface down to the atomic level, SPMs constitute an essential tool for the age of nanotechnology. Basically, two kinds of SPMs were first invented: Scanning Tunnel Microscopy and Atomic Force Microscopy. The principles and the capabilities of these two techniques are presented in the next sections.

3.2.1 Scanning Tunneling Microscopy

Scanning Tunneling Microscopy (STM) was invented in 1982 by G. Binnig and H. Rohrer [Binnig et al., 1982b,a], who were awarded the Nobel prize for physics in 1986. The emergence of STM has made possible to observe the arrangement of individual atoms on materials surfaces, and physical and chemical properties related to the behavior of surface electrons in real space. In STM, surface imaging exploits the electron quantum tunneling between probe and sample.

3.2.1.1 Principles of STM

A schematic diagram of STM is reported in Fig. 3.4a. A sharp metallic tip is brought into close proximity with the sample. Since the distance between tip and sample is only few angstroms, their respective wave functions overlap due

to their "leaking out" into vacuum. A bias voltage permits then to electrons to tunnel through the barrier, as schematically represented in Fig. 3.4b for the one dimensional case. For low bias voltages and at low temperatures, the current of tunneling electrons follows the expression [Besenbacher, 1996]:

$$I(V, r_0) \approx \int_{E_F}^{E_F+eV} \rho_S(E, r_0) \rho_T(E - eV) e^{-2d\sqrt{\frac{2m_e\bar{\Phi}+eV/2-E}{\hbar^2}}} dE \quad (3.1)$$

where V is applied voltage, d is the distance between sample and tip, ρ_S and ρ_T are the surface and tip density of states, respectively, and $\bar{\Phi}$ their average work function.

The exponential dependence on d is the key for the ultimate resolution of the technique. Due to the fact that wave functions overlap is relevant only over atomic-scale distances, the tunneling current changes typically one order of magnitude while the gap distance changes only by 1 Å. Thus, the vertical resolution of STM is around 0.001 nm while the lateral one is about 0.05 nm. To achieve these high resolutions, it is mandatory to control precisely the motion of the tip across the surface. To do so, the tip is moved by means of a piezoelectric scanner controlling the position of the tip along the three dimensions.

Eq. 3.1 shows that in addition to the distance-dependence of the tunneling current there is also a bias-dependence. This implies that by varying the polarity and the amount of the applied bias voltage, one can select the electronic

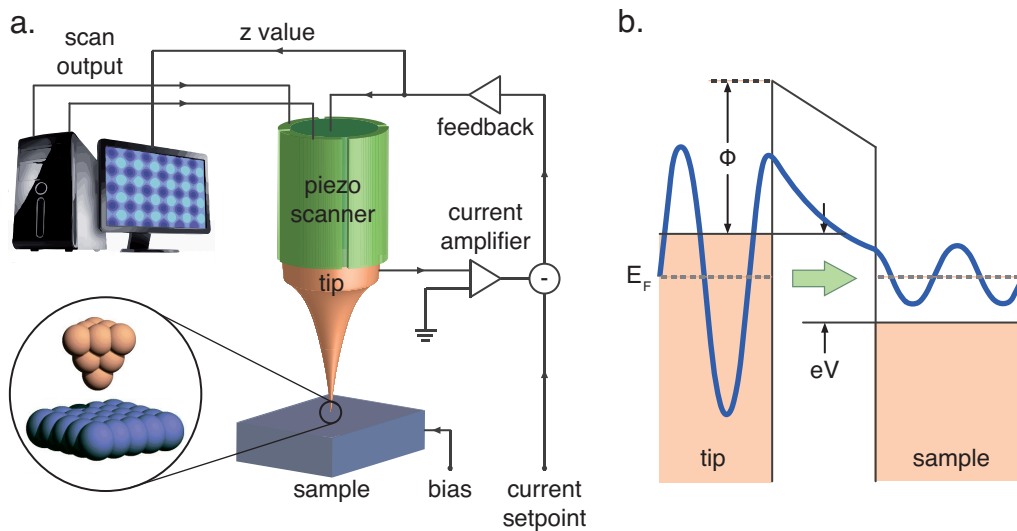


Figure 3.4: a. Schematic diagram of the scanning tunneling microscope. b. One-dimensional tunnelling junction.

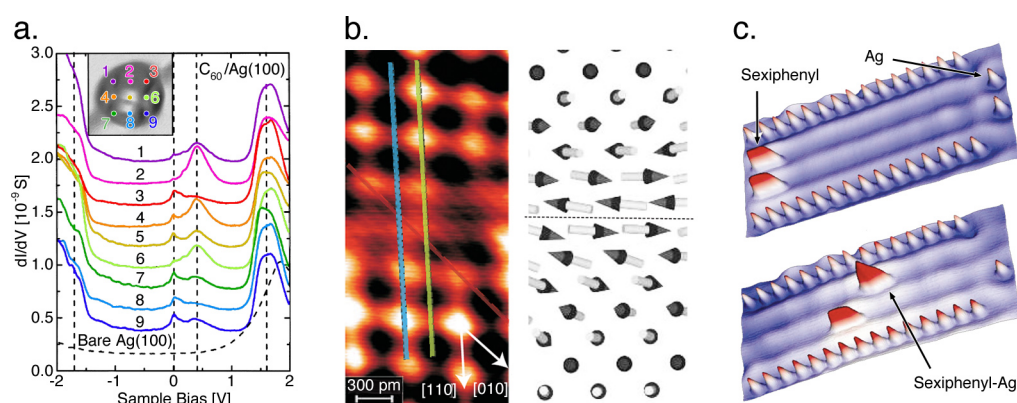


Figure 3.5: Some examples of the capabilities of STM. a. dI/dV spectra of a single C_{60} on Ag(100), showing the spatial distribution of the density of states inside an individual molecule (figure extracted from [Lu et al., 2003]). b. Domain wall in the antiferromagnetic Fe monolayer: on the left, spin-polarized STM image and theoretical spin structure, on the right (figure extracted from [Bode et al., 2006]). c. Molecular "shooting" of the upper sexyphenyl towards an Ag atom. Below, the complex formed and the bare sexyphenyl are moved in the middle for a comparison. (figure extracted from [Hla et al., 2004])

states that contribute to the tunneling current. If the tip density of states is constant in the considered voltage range, the first derivative $dI/dV(V)$ reflects the sample electronic density of states. This spectroscopic capability combined with the high spatial resolution is perhaps the most important feature of STM and has been applied widely (Fig. 3.5a). More recently, the use of magnetic tip introduced a spin-dependency in the tunneling current that has permitted to investigate also the magnetic structure with atomic resolution [Wiesendanger et al., 1990] (Fig. 3.5b).

Finally, new possibilities are offered by the use of local probes to manipulate single atoms or molecules and hence to form artificial structure on the atomic scale [Eigler and Schweizer, 1990] (Fig. 3.5c).

3.2.1.2 Variable Temperature STM

In this thesis work we employed a Variable Temperature STM (VT STM XA) commercially available from Omicron⁴ and shown in Fig. 3.6. With this instrument, it is possible to image the sample in a wide temperature range from 50 K up to 650 K. For temperatures above 300 K, an element embedded in

⁴<http://www.omicron.de>

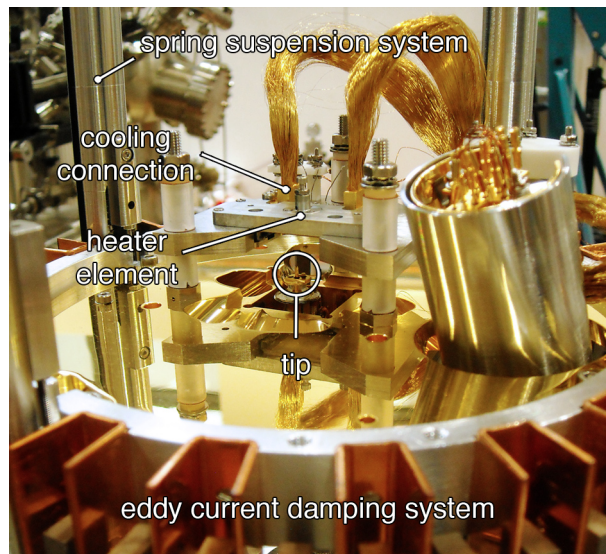


Figure 3.6: Picture of the VT STM XA used during this thesis. Some relevant parts of the microscope are highlighted.

the stage permits a resistive heating of the sample. Under 300 K, the sample is cooled with a continuous flow of liquid nitrogen or helium in the cryostat, that is connected to the stage thanks to copper connections. The sample is also thermally isolated to minimize thermal drift. The temperature is checked with a Si-diode placed in the proximity of the sample plate. Finally, the spring suspension and an eddy current damping allows a good vibration isolation of the microscope. The STM images are analyzed with the WsxM software [Horcas et al., 2007].

3.2.2 Atomic Force Microscopy

Atomic Force Microscopy (AFM) was developed in 1986 by Binnig, Quate and Gerber [Binnig et al., 1986], who developed the concept behind that microscope to overcome its main limitation, namely the capability of investigating insulator surfaces. In AFM, mechanical force interactions acting between a probe and a sample are used for surface imaging.

3.2.2.1 Principles of AFM

A schematic diagram of AFM is reported in Fig. 3.7a. The tip, a micromachined cantilever with a sharp tip at one end, is brought into interaction with the sample surface. The interaction level between the tip apex and the sam-

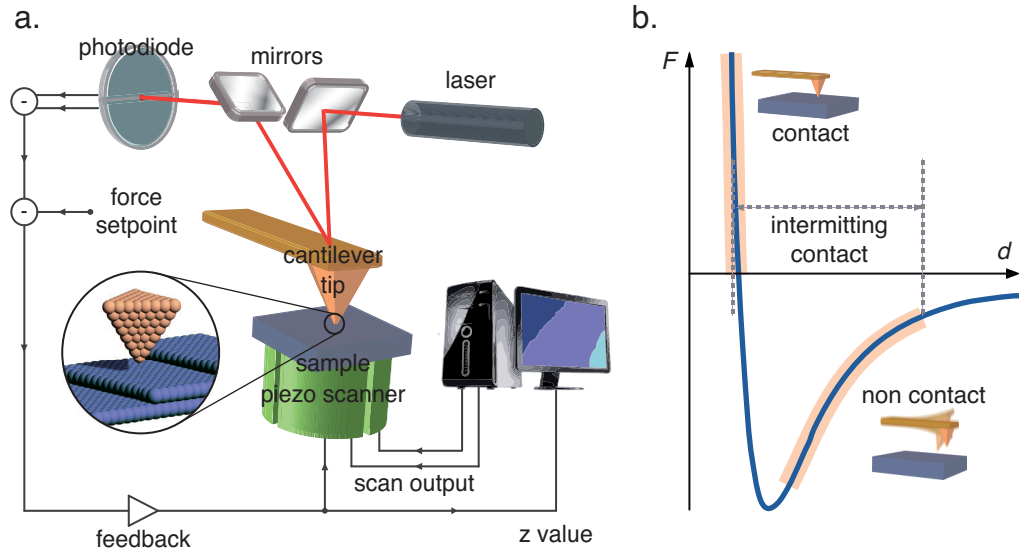


Figure 3.7: a. Schematic diagram of the atomic force microscope. b. Lennard-Jones potential.

ple is determined through a precise measurement of the cantilever displacements. This is done with an optical level detection: a laser beam is deflected on the backside of the cantilever and then is directed to a 4-segment photodetector that measures vertical and lateral deflections of the cantilever. Like for STM, the motion of the tip with respect of the sample is controlled by means of a piezoelectric scanner. Several forces contribute to the deflection of the cantilever, the most important arises from van der Waals interaction, that can be described empirically with the Lennard-Jones potential:

$$V_{LJ} = -3\epsilon \left[\left(\frac{\sigma}{d} \right)^{12} - \left(\frac{\sigma}{d} \right)^6 \right] \quad (3.2)$$

where ϵ represents the depth of the well and σ the distance where the potential is zero. The r^{-12} term describes Pauli repulsion, while the r^{-6} describes London dispersion forces. As shown in Fig. 3.7b, according to the distance between the tip and the sample, the AFM can operate in different regimes: contact, non contact and an intermediate contact (or tapping) mode. Briefly, in the contact mode the tip is pressed to the surface down to less than 1 nm in distance and the repulsive force causes the cantilever to bend to accommodate changes in topography. Conversely, in the non contact mode the cantilever is vibrating at a certain frequency at tens of nm above the surface and the tip-surface interactions produces a change in the frequency of the cantilever, providing a measurable signal. With respect to STM, the AFM reso-

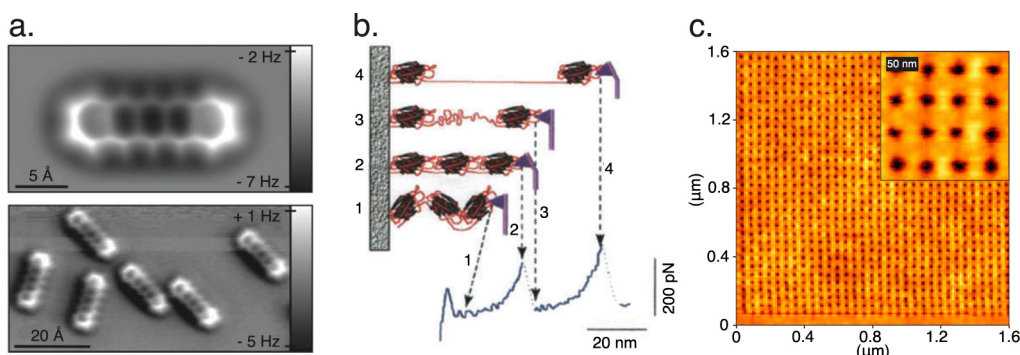


Figure 3.8: Some examples of the capabilities of AFM. a. Atomic resolution of pentacene on Cu(111) achieved by functionalizing the tip with a CO molecule (figure extracted from [Gross et al., 2009]). b. Domain deformation and unfolding of a multidomain protein with AFM (figure extracted from [Bao and Suresh, 2003]). c. Patterning of a polymeric surface generated by indentation of an AFM tip (figure extracted from [Jo et al., 2009]).

lution is generally lower due to the smoother distance dependence of the interaction that causes a distribution of the force over many atoms on the tip and the sample surface. Typically the vertical resolution is 0.01 nm while the lateral one is determined by the size of the tip (reaching around 1 nm for the sharpest tips commercially available). Nonetheless, it is to point out that AFM can achieve true atomic resolution under UHV in non contact mode [Giessibl, 1995] (Fig. 3.8a). The manipulation capabilities of AFM are exploitable in a wide range of fields: from fundamental studies on protein folding (Fig. 3.8b) to applications in high density data storage devices (Fig. 3.8c).

Other microscopies have been derived from AFM, with the aim to detect only a specific interaction among the several forces that act on the tip. In this way it's possible to spatially map different physical properties of the sample. Near-field Scanning Optical Microscope (SNOM), Lateral Force Microscopy (LFM), Electrical Force Microscopy (EFM), Magnetic Force Microscopy (MFM) and Kelvin Probe Force Microscopy (KPFM) are the principal ones.

3.2.2.2 Kelvin Probe Force Microscopy

Kelvin Probe Force Microscopy is a variant of AFM invented in 1991, capable of mapping local changes in the sample work function [Nonnenmacher et al., 1991]. To this purpose a conducting tip is brought in contact with the sample and as a consequence of the difference in their work functions $\Delta\Phi$ (that include also changes due to adsorption layers on the surface), a contact poten-

tial $V_{cp} = \Delta\Phi/e$ arises to align the Fermi levels. In KPFM this contact potential is measured with the following procedure. During the scan, the tip acquires the surface topography of a single line using standard tapping mode. In the second trace this topography is retraced at a set lift height from the sample surface and the cantilever is no longer excited mechanically but electrically by applying an ac voltage with adjustable dc offset $V_{dc} + V_{ac}\sin(\omega t)$ to the tip. A resulting electrostatic force acts on the tip which, assuming a parallel-plate-geometry, has the following expression:

$$F_{\omega} = \frac{\partial C}{\partial z} [(V_{dc} - V_{cp})V_{ac}\sin(\omega t)] \quad (3.3)$$

where C is the local capacitance between the tip and the sample. This force is detected by an active feedback that changes the dc tip potential V_{dc} until the ω variable component of the force vanishes ($V_{dc} = V_{cp}$). KPFM allows to study the electric potential distribution of a surface with resolutions of a few nanometers and some millivolts.

3.3 Magneto-Optic Kerr Effect

The first magneto-optic effect was discovered by Faraday in 1845. He found that the effect of a magnetic field applied to a transparent specimen was to rotate the polarization plane of the transmitted light. Thirty-two years later Kerr discovered this effect when examining the polarization of light reflected from a polished electromagnet pole. Then, in 1985 magneto-optic Kerr effect was applied to the study of surface magnetism [Bader and Moog, 1985]. Since then, this technique is commonly used to characterize the magnetic properties of magnetic surface and thin films.

3.3.1 Principles of MOKE

The origin of magneto-optics relies on the difference in the refractive indexes for right- and left-handed circularly polarized light in magnetized media. As a consequence of its interaction with the sample, the polarization state of the light is modified. First, the polarization plane rotates due to different propagating velocities of the two polarized modes, which causes different phase shifts. Secondly, the different absorption rates affect the polarization ellipticity. The difference in the refractive indexes can be understood both on the basis of the macroscopic dielectric theory and the microscopic quantum theory. In the frame of the microscopic approach, the key quantity is the spin-orbit coupling that can be written as $\sim \boldsymbol{\mu} \times \nabla V \cdot \mathbf{p}$. This is the energy of interaction of

the electron magnetic moment ($\boldsymbol{\mu}$) with the magnetic field it sees as it moves through the electric field ∇V with momentum (\mathbf{p}). The magnetic moment and the motion of the electron are thus related and since the motion of charges affects the optical properties of the specimen, the magneto-optical effect is explained. In particular, it is the asymmetry in the electron wave functions for the spin-up and down electrons that explain the difference in the two refraction indexes. On this basis the Kerr effect for ferromagnets can be completely described [Argyres, 1955]. From a macroscopic point of view to find the origin of magneto-optic effects we have to consider the electric displacement of a magnetized medium $\mathbf{D} = \boldsymbol{\varepsilon}(\mathbf{E} + iQ_V\mathbf{M} \times \mathbf{E})$. The dielectric tensor is:

$$\boldsymbol{\varepsilon} = \varepsilon_0 \begin{pmatrix} 1 & -iQ_V M_z & iQ_V M_y \\ iQ_V M_z & 1 & -iQ_V M_x \\ -iQ_V M_y & iQ_V M_x & 1 \end{pmatrix} \quad (3.4)$$

The refraction indexes of the left- and right-circularly polarized light modes are then:

$$n_L = \sqrt{\varepsilon} \left(1 - \frac{Q_V \mathbf{M} \cdot \hat{\mathbf{k}}}{2} \right) \quad \text{and} \quad n_R = \sqrt{\varepsilon} \left(1 + \frac{Q_V \mathbf{M} \cdot \hat{\mathbf{k}}}{2} \right) \quad (3.5)$$

where Q_V is the Voigt coefficient and \mathbf{M} is the material magnetization and $\hat{\mathbf{k}}$ is the unit vector along the direction of light. Thus, the magneto-optic effect arises from the presence of antisymmetric, off-diagonal elements in the dielectric tensor.

To explicit the expression for Kerr rotation and ellipticity one has to calculate the reflectivity of the system [Zak et al., 1990]. We focalize here on the simple and common case of a magnetic sample surface reflecting a linearly p -polarized light, as sketched in Fig. 3.9a:

$$\mathbf{E}_r = \begin{pmatrix} R_K \\ R_N \end{pmatrix} = \begin{pmatrix} r_{ss} & r_{sp} \\ r_{ps} & r_{pp} \end{pmatrix} \cdot \mathbf{E}_i = \begin{pmatrix} r_{ss} & r_{sp} \\ r_{ps} & r_{pp} \end{pmatrix} \cdot \begin{pmatrix} 0 \\ E \end{pmatrix} = \begin{pmatrix} E r_{sp} \\ E r_{pp} \end{pmatrix} \quad (3.6)$$

where \mathbf{E}_i and \mathbf{E}_r are the incident and reflected electric field, respectively. The Kerr rotation and ellipticity are then given by $\phi_p = \phi'_p + i\phi''_p = r_{sp}/r_{pp}$. The component $R_K = E r_{sp}$ arises from the sample magnetization, thus the goal of the experiment is to measure this quantity. To do so, a polarizer is placed at a small angle δ from the p axis to eliminate the majority of the p component. Then a photodetector will measure the intensity [Š. Višňovský et al., 1995; Qiu and Bader, 2000]:

$$I = |E r_{pp} \sin \delta + E r_{sp} \cos \delta|^2 \approx |E r_{pp}|^2 |\delta + \phi' + i\phi''|^2 \approx I_0 \left(I + \frac{2\phi'}{\delta} \right) \quad (3.7)$$

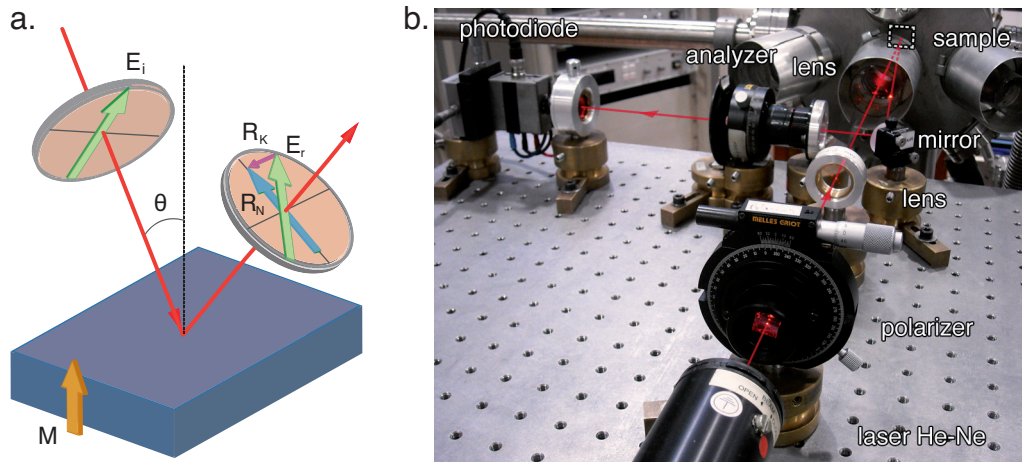


Figure 3.9: a. Schematic representation of the Kerr effect in the polar configuration. b. Picture of the experimental optical setup used for MOKE measurements.

since ϕ' is linearly proportional to the magnetization, measuring the intensity as a function of the applied magnetic field yields the hysteresis loop.

According to the direction of the magnetization vector with respect to the reflecting surface and the plane of incidence three different geometries can be identified. In the polar MOKE the magnetization is perpendicular to the surface and parallel to the plane of incidence, in the longitudinal MOKE the magnetization is parallel to both the surface and the plane of incidence, in the transversal MOKE the magnetization is perpendicular to the plane of incidence and parallel to the surface.

3.3.2 Experimental setup

The optical setup for MOKE is reported in Fig. 3.9b. A He-Ne laser is used as a light source ($\lambda = 633 \text{ nm}$, $P = 13 \text{ mW}$). A first Glan-Taylor polarizing prism (Melles Griot⁵) defines the polarization plane of the incident light. A lens with focal length $f = 50 \text{ cm}$ focuses the laser beam on the sample surface within the UHV apparatus. The optical access is provided by a fused-silica viewport, whose birefringence can be neglected. After being reflected from the sample the beam exits from the UHV chamber where it is further reflected by a mirror. Then it goes through another lens ($f = 10 \text{ cm}$) and the crossed analyzer, another Glan-Taylor prism. Parasitic beams are removed with an iris diaphragm and the stray background light is eliminated with an interferential filter. The

⁵<http://www.cvimellesgriot.com>

light is finally focused at the center of a photovoltaic diode detector.

For polar measurements the magnetic field is generated with a electromagnetic coil wrapped around the sample holder, outside the UHV apparatus. At its center, an uniform field of 130 Oe/A is generated. The intensity of the magnetic field is controlled by a function generator, through a bipolar power supplier (Kepco⁶). Additionally, the sample is placed on a cryostat that can be cooled with a continuous flow of liquid nitrogen or liquid helium down to 20 K or heated up with a resistive heater. The sample temperature is checked with a silicon diode and a rhodium-iron resistance sensor. Temperature ramps can thus be performed thanks to a temperature controller (Lakeshore⁷).

The susceptibility measurements as a function of temperature are carried out using the so-called ac-MOKE [Berger et al., 1994; Aspelmeier et al., 1995]. In this case a sinusoidal magnetic field of small amplitude ($\nu = 1$ Hz, $H_{\text{RMS}} = 10$ mT) is applied. The sample response is also sinusoidal and is detected by a lock-in amplifier (Stanford Research System⁸) locked to the coil alimentation signal as a reference. In this way the magnitude and the dephasing of the signal permit to measure at the same time the real and imaginary parts of the complex susceptibility $\chi = \chi' + i\chi''$.

⁶<http://www.kepcopower.com>

⁷<http://www.lakeshore.com>

⁸<http://www.thinksrs.com>

Growth on linear Au(111) and magnetism of Co island arrays

In this chapter we will focus our attention on the growth and the magnetic properties of epitaxial Co nanostructures on Au(111) surfaces. This is a model system, since Au(111) surface reconstruction organizes the first stage of growth in well-ordered clusters with a diameter adjustable up to few nanometers. Since the islands are quasi mono-dispersed, measurements over macroscopic areas reflect single-island properties, allowing to unambiguously study the magnetic properties of the clusters.

The first section will be dedicated to the Au(111) surface and its herringbone reconstruction, that has already been widely studied in the literature. Then, we will show that the Au reconstruction can be lifted to obtain a unidirectional one, using a new multilayer sample. In the successive section the growth of Co on both these templates will be described. The conventional Au(111) surface is well known to guide the growth of Co in arrays of nanoislands with tunable size. On the other hand, we investigate the capability of Au(111) with unidirectional reconstruction to obtain unidimensional nanostructures. Finally, in the last section of the chapter is reported the study of the magnetic behavior of the nanoparticles grown on these templates. In particular, a detailed analysis on the size dependence of the Co nanoislands magnetic behavior has permitted to gain new insights into the magnetization reversal of this system.

4.1 Au(111) surface

The surface of Au(111) has gained a predominant role in the field of self-organization at surfaces thanks to its herringbone reconstruction. This can be used as a regular template to organize the growth of metal clusters. In the following we will describe this unique surface in detail. We will also show that its reconstruction can be lifted to purely linear.

4.1.1 Au(111) with herringbone reconstruction

The driving force for Au(111) surface reconstruction is the tensile stress that would act on the outermost layer of the unreconstructed surface. In response to this stress, the surface layer spontaneously densifies along the $\langle 1\bar{1}0 \rangle$ directions, arranging one extra atom every 22 atoms of the underlying layer with bulk lattice parameters. In this way the reconstructed layer is 4% denser than the bulk (111) planes, giving rise to the $22 \times \sqrt{3}$ reconstruction. Inside the unit cell the atoms are arranged in fcc and hcp-type stacking domains separated by two stacking fault lines (or discommensuration lines), where atoms pass continuously from one type of stacking to the other (Fig. 4.1a). These lines are pairwise-arranged and run in the $\langle 11\bar{2} \rangle$ direction. The distance between neighbored pairs in the $\langle 1\bar{1}0 \rangle$ direction amounts to 64 Å while the individual lines within a pair are distant ~ 24 Å. In the stacking fault regions the atoms are raised above the surface of around ~ 0.3 Å and thus they appear brighter in the STM image [Wöll et al., 1989; Barth et al., 1990] (as can be seen in Fig. 4.1a).

Due to the hexagonal symmetry of the surface, the atoms can densify to give the $22 \times \sqrt{3}$ reconstruction along three equivalent directions. Actually, there is a regular alternation of domains of two out of three orientations and the $22 \times \sqrt{3}$ domains bend by 120° . In this way a mesoscopically ordered pattern is formed with a typical period of $a_1 = 7$ nm and $a_2 \simeq 25$ nm (but can vary between 20 and 30 nm according to the area or the samples) [Barth et al., 1990]. This so-called herringbone reconstruction pattern is a secondary superstructure that arises from more delicate long-range elastic interactions mediated by the substrate [Narasimhan and Vanderbilt, 1992], to relax a compression otherwise unidirectional. On the boundaries between the uniaxial domains the discommensuration lines change direction forming elbows, as shown in Fig. 4.1c. The direction of the elbows and their appearance alternates from one uniaxial domain boundary to the next. In one case the hcp regions are very narrow and in the other case the hcp and fcc regions are nearly equals: thus the two types of elbows are called respectively pinched and bulged. The distorted structure of the elbows can be explained on the basis of the crys-

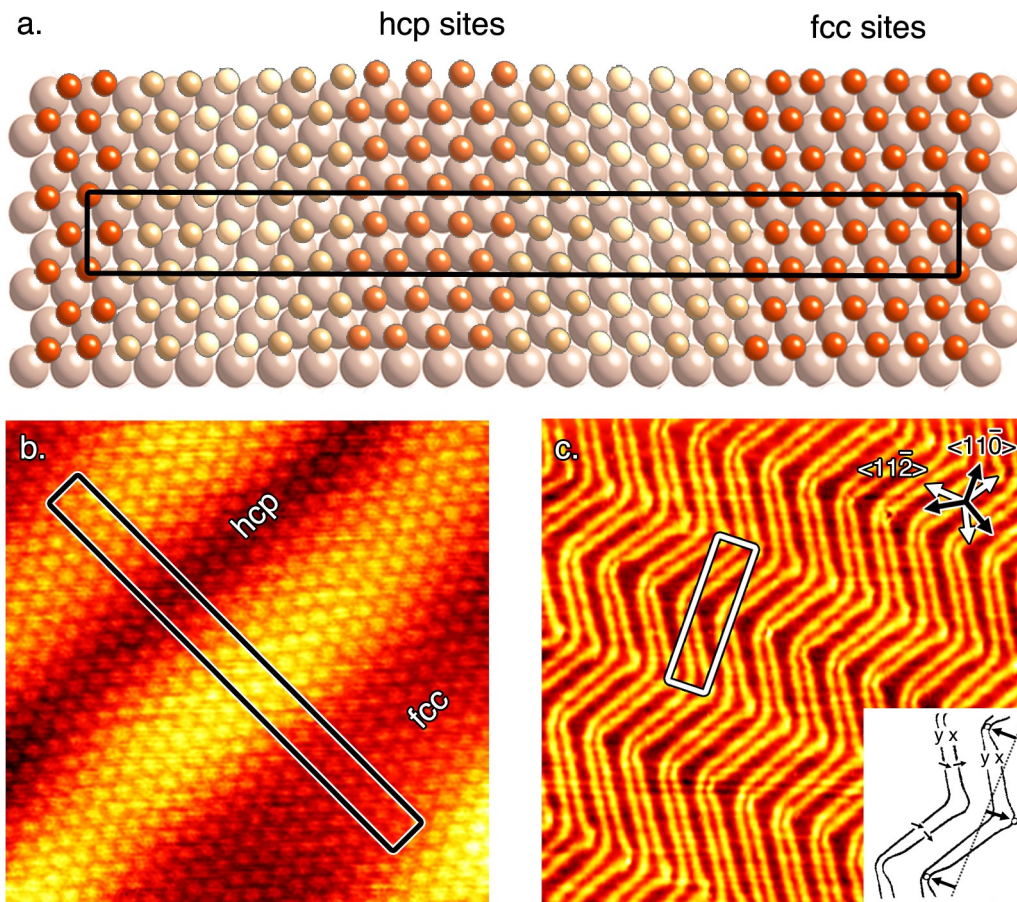


Figure 4.1: a. Atomic model of the $22 \times \sqrt{3}$ reconstruction (figure redrawn from [Ibach, 1997]). b. Atomic resolution STM image ($6.7 \times 6.7 \text{ nm}^2$) of Au(111) surface the unit cell of the $22 \times \sqrt{3}$ reconstruction highlighted. c. STM image ($100 \times 100 \text{ nm}^2$) of Au(111) surface showing the herringbone reconstruction pattern, whose unit cell is highlighted.

tallography of the reconstruction. Indeed, the discommensuration lines of the $22 \times \sqrt{3}$ reconstruction are described by two different Burger vectors [Wöll et al., 1989]. When the reconstruction bends by 120° , the Burger vector remains oriented in the same direction in the case of the so-called type- y discommensuration line (following the notation of [Chambliss et al., 1991]) while changes direction for the type- x , as shown in the inset of the Fig. 4.1c. In this case, when two segments of the uniaxial domain meet a dislocation arises in the surface lattice, whose Burger vector is the difference between those of the two segments. In the proximity of the dislocation the atoms are strained and under-coordinated. For this reason the elbows represent preferential nucle-

ation sites. The regular dislocation network of Au(111) makes this surface a template capable to guide the growth of several metals towards the formation of ordered cluster arrays. Apart from Co [Voigtländer et al., 1991a], an organized growth was demonstrated for Ni [Chambliss et al., 1991], Fe [Voigtländer et al., 1991b], Pd [Stephenson et al., 1998] and Mn [Fonin et al., 2003]. When the Au(111) surface is observed by scanning tunneling microscopy, wide terraces of about 300 nm in extent are typically observed, separated by monoatomic steps 2.35 Å high. These, together with other defects of the surface like screw dislocations, induce inhomogeneous strain field and affect the reconstruction in their surroundings [Repain et al., 1999].

4.1.2 Au(111) with unidirectional reconstruction

Despite its unique properties, Au(111) surface lacks of versatility and in particular it is difficult to control the islands shape. The availability of a similar template for the organization of nanowires would have a significant impact both from a fundamental and an applied point of view, since nanowires of metallic and semiconducting elements will possibly play a crucial role in future devices. Also, nanowires of ferromagnetic elements have shown unusual magnetic properties due to the symmetry lowering [Gambardella et al., 2004]. In this section we report on the fabrication of such a linear template, resulting from the modification of the usual Au(111) reconstruction using epitaxial strain in thin Au films. The multilayer sample used for this scope (schematically shown in Fig. 4.2a) was conceived and grown by O. Fruchart and colleagues at the Institut Néel in Grenoble ¹.

Because of its role played in the Au(111) surface reconstruction, stress is the key parameter to handle if one wants to guide the surface towards new arrangements. In particular, to stabilize a purely linear reconstruction it is necessary to impose a uniaxial strain. The feasibility of this route was firstly demonstrated by Schaff *et al.* using a mica sheet upon which a Au layer had been deposited [Schaff et al., 2001]. Upon bending the mica sheet the reconstructions get deformed until the zigzags are lifted in purely linear reconstructions for 0.4% strain in the mica. However the authors acknowledge that the process was neither reproducible nor quantifiable, probably because the Au grains were floating on the bendable mica sheet.

4.1.2.1 Description of the multilayer sample

The substrate we choose for our sample is sapphire with $(11\bar{2}0)$ as terminating surface, which is now among the standard commercial wafers due to its use in the Light-Emitting Diode technology. It is important here to highlight that only the availability of highly ordered template on commercial wafers permits to exploit the advantages of self assembly on larger scale. Over this a very thin film (1 nm) of Mo and a thicker one (10 nm) of W are grown by pulsed-laser deposition. Both Mo and W are bcc metals that during the growth expose the (110) surface, which is close to an hexagonal lattice distorted by $\sim 20\%$ in the x direction (cf. Fig. 4.2b). When grown on W(110), Au(111) adopt a Nishiyama-Wassermann orientation with a unique epitaxial relationship: $\text{Au}[\bar{1}10] \parallel \text{W}[001]$ and $\text{Au}[11\bar{2}] \parallel \text{W}[\bar{1}10]$ [Bauer et al., 1977; Augustus and Jones, 1977], as shown in Fig. 4.2b. The distorted hexagonal structure of the W(110) surface causes an epitaxial mismatch in the Au film, that is essentially relieved in the first layer of Au(111). Nonetheless a weak residual strain survives in the topmost layer of the Au film (10 nm thick), that has been measured to be $\lesssim 0.1\%$ with surface X-ray diffraction [Fruchart et al.]. This weak strain induces a uniaxial strain in the Au layer which is capable to lift the original three-fold symmetry and to induce a preferential orientation of the compressed $[1\bar{1}0]$ direction. It is important to highlight that the heteroepitaxial

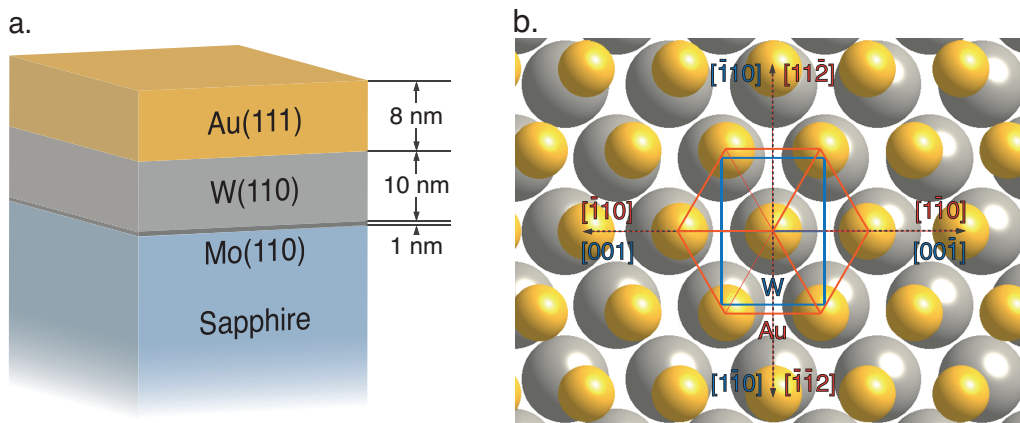


Figure 4.2: a. Scheme of the multilayer sample employed. b. A bulk-like lattice of Au(111) (in yellow) is superimposed on a rectangular bulk-like lattice of Mo(110) (in gray) to schematically represent their epitaxial relationship, the crystallographic directions of the two layers are also reported.

¹<http://www.neel.cnrs.fr>

constraints permit to stretch the reconstruction in the same direction over the whole sample. The in-plane strain and anisotropy in the Au layer are surprisingly small, at least one order of magnitude smaller than that reported by Schaff et al. required to induce the transformation to purely linear reconstruction. This could be explained by confirming the suggestion of the authors that Au film was not strongly clamped to the mica substrate.

4.1.2.2 STM study of Au(111) with linear reconstruction

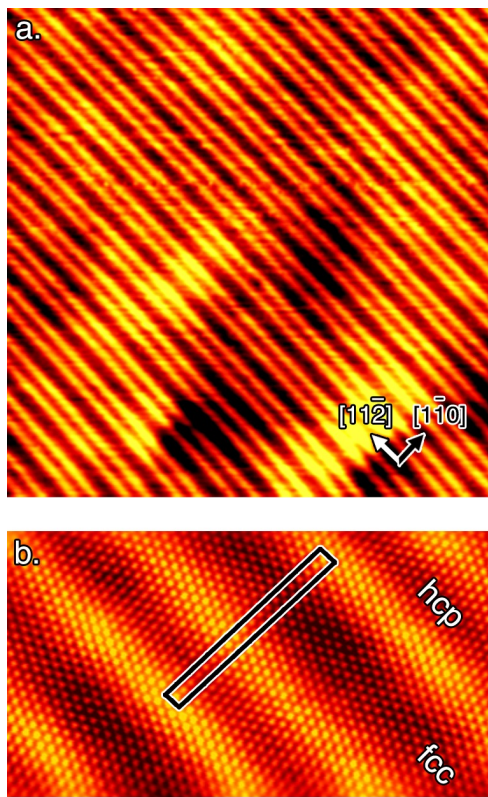


Figure 4.3: a. Room temperature STM image showing the unidirectional reconstruction of the stressed Au(111) surface ($85 \times 85 \text{ nm}^2$). b. Drift compensated atomic resolution STM image, with the unit cell highlighted ($15 \times 8 \text{ nm}^2$).

In Fig. 4.3a an image of the uniaxial Au(111) surface is reported. The brighter lines are the discommensuration lines that run along the $[11\bar{2}]$ direction, while in the close-packed $[1\bar{1}0]$ one hcp and fcc atomic stacking regularly alternate. As can be clearly seen, the herringbone reconstruction is suppressed and the purely linear reconstruction is stable over the whole sample surface. The stacking faults lines are characterized by a corrugation height of $0.17 \pm 0.02 \text{ \AA}$ while the distance between two adjacent maxima is around 57 \AA , in contrast from the value observed for the reconstruction of Au(111) single-crystal surface. Indeed, the supercell that can be identified in image of 4.3b shows that the periodicity is drifted to 20 atomic positions. As predicted theoretically [Tartaglino et al., 2002], the reconstruction period can be changed under strain but the predicted values are higher than in the present case ($\sim 0.4\%$).

At larger scale (Fig. 4.4a) some defects of the reconstruction also appears, mainly due to defects of the surface morphology. The most visible signatures in STM images come

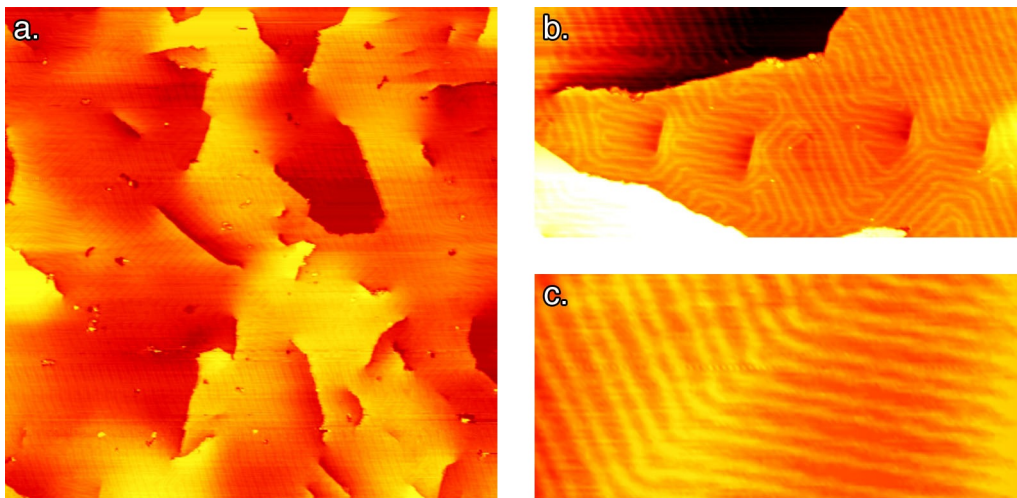


Figure 4.4: STM images of the Au(111) thin film surface a. Large scale showing the presence of different defects ($360 \times 360 \text{ nm}^2$). b. Effect of a sequence of stacking fault ribbons on Au(111) reconstruction ($130 \times 60 \text{ nm}^2$). c. The reconstruction deviates from its unidimensional character and turns of 120° as in the herringbone reconstruction ($60 \times 30 \text{ nm}^2$).

from screw dislocations that appear as emerging steps. Edge dislocations leave weaker footprints on the morphology, but are responsible for important deviations from the purely linear reconstruction. At the surface edge dislocations split into two partial dislocations that elastically repel each other and form a stacking fault ribbon that appear like a short step segment high one third of the full step height. These defects are seen also on single crystal Au(111) surface, even if less commonly [Engbæk and Schiøtz, 2006]. More particularly, on the present sample these stacking fault ribbons are commonly arranged in sequences, as shown in Fig. 4.4b. When the reconstruction deviates from its unidimensional character, it turns by 120° as in the herringbone reconstruction (Fig. 4.4c). Naturally, the reconstruction elbows constitute the main trap for diffusion adatoms and represent the principal difficulty to overcome in order to obtain a homogeneous growth. Random atomic impurities also constitute other nucleation sites; their role must be underlined in the present case because of the thinness of the Au layer that requires a careful control of the Ar sputtering time.

4.2 Self organization of Co on Au(111)

Self organization provides new and easy method for producing arrays of high periodicity with perfect structure and narrow size distribution. The strong impact of morphology on the physical properties of nanostructures makes it mandatory to finely control and tune their size and shape. In this section we will show that Au(111) permits to exercise such a control. Nanoislands with increasing size (made of up to 1500 atoms) can be obtained simply by increasing the deposition time. Moreover it is shown that this template surface can acquire a new versatility, by employing Au(111) with purely linear reconstruction to grow elongated nanoislands.

4.2.1 Co nanoislands with increasing size

Due to the large lattice mismatch between Co and Au (14% of the bulk values), one could guess that the growth follows the Volmer-Weber mode. However, the influence of the Au(111) surface was pointed out only with the first STM studies on Co submonolayer coverages [Voigtländer et al., 1991a] where it was evident that the elbows of the reconstruction act like traps for the diffusion of adatoms. At room temperature these sites strongly govern the nucleation and growth, permitting to create order and uniform array of Co nanoisland

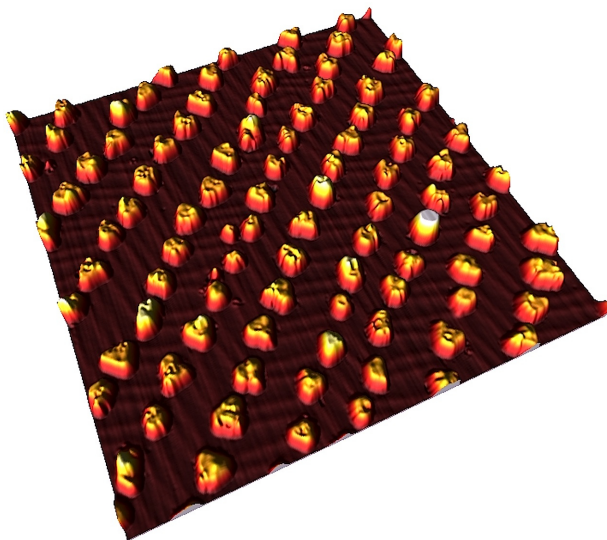


Figure 4.5: 3D STM image ($90 \times 90 \text{ nm}^2$) of a typical deposit of Co (0.4 ML) on Au(111). 2 ML height polygonal Co islands nucleate at the elbows of Au herringbone reconstruction.

as shown in Fig. 4.5. This property is due to the fact that the mean free path of diffusing atoms is larger than the distance between the elbows. Therefore, in the earliest stage of the growth the adatoms mainly reach these preferred nucleation sites. Here, Au atoms have a reduced lateral coordination due to the high strain and are susceptible to site exchange with diffusing adatoms [Meyer et al., 1996; Repain et al., 2002]. The site selective exchange is followed by preferential nucleation of islands on top of the substitutional atoms. In the first nucleation regime all the elbows sites get occupied and the following adatoms attach to the existing islands. The island density n_i on the surface remains constant and equal to the density of the nucleation sites n_{ns} . In this way an organized growth is obtained. Moreover, since the nucleation sites are periodically arranged the capture areas are similar, leading to regular islands with a narrow size distribution [Chambliss et al., 1991]. The array is imposed by the Au(111) herringbone reconstruction: inside the unit cell (with size $7 \times 25 \text{ nm}^2$) 2 nanoislands are arranged. The nucleation and growth of Co on the Au(111) surface at room temperature have been investigated notably by means of helium-atom scattering experiments [Tölkes et al., 1997] and grazing incidence small angle X-ray scattering [Fruchart et al., 2003].

The polygonal shape of the islands seen in STM images is an indication of their crystalline character, they are in prevalence hexagonal with long and short step segments opposite to each other, in agreement with the $2\pi/3$ symmetry of the Au(111) surface. The lattice mismatch between Au and Co is so strong that any stress storage is prevented and Co lattice relaxes to its bulk value. This is also the reason why bilayer islands are energetically favorable from very small cluster size (about 20 atoms) as demonstrated by experiments and numerical simulations [Chado et al., 2004]. Indeed, the step height of Co islands as measured by STM (around 4.1 \AA) corresponds well to twice the distance of two adjacent Co(0001) lattice planes in the bulk (4.07 \AA) [Hull, 1921].

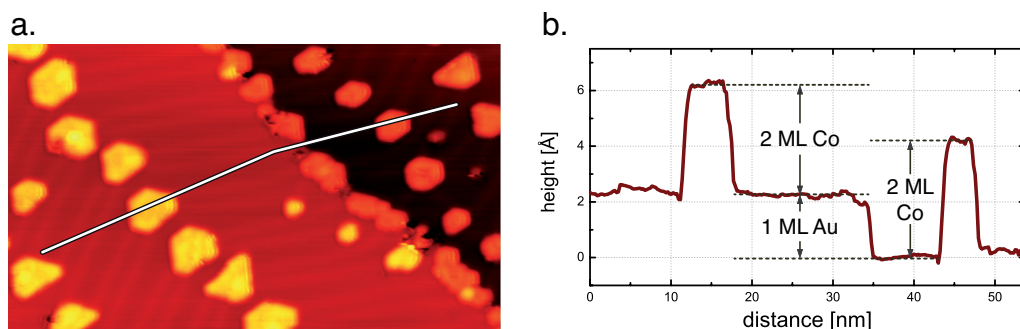


Figure 4.6: a. STM image of 0.4 ML of Co on Au(111) ($60 \times 35 \text{ nm}^2$). b. Height variation profile along the line indicated in the STM image.

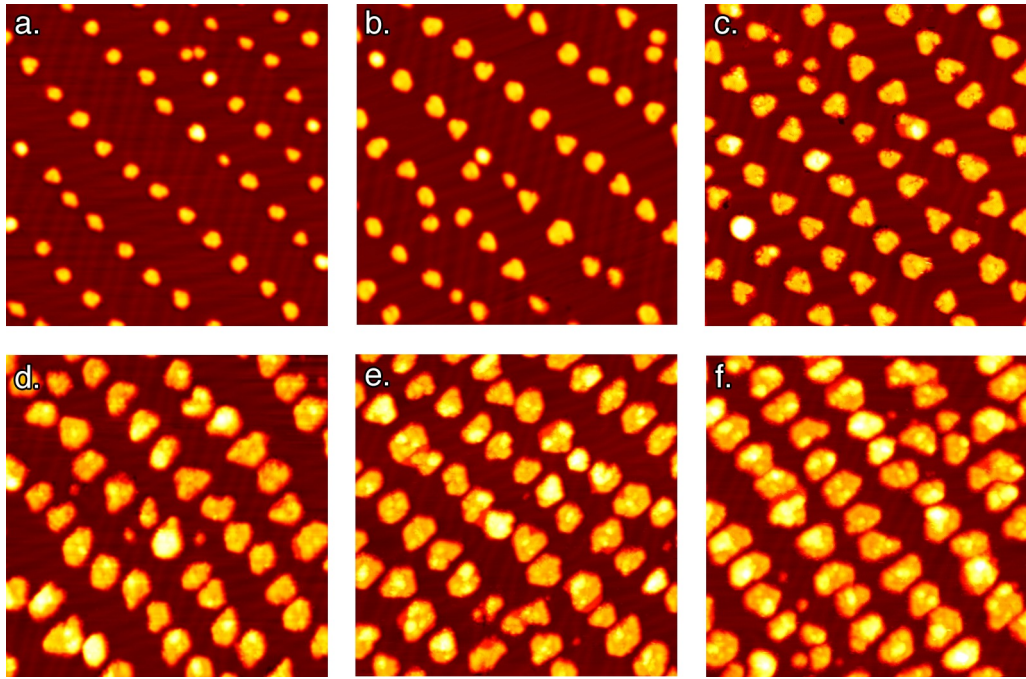


Figure 4.7: STM images show the evolution of the dot morphology when θ_{Co} is gradually increased a. 0.13 ML b. 0.19 ML c. 0.39 ML d. 0.58 ML e. 0.65 ML and f. 0.78 ML.

A typical profile height is reported in Fig. 4.6. When the coverage is gradually increased the morphology of the nanoislands evolve, as shown by different STM images in Fig. 4.7. The growth of nanoislands proceeds mainly with an augmentation of the mean diameter D while the initial bilayer height is substantially preserved. Anyway, few Co atoms can be observed on the top of some islands above 0.3 ML as brighter dots in the STM image. Taking into account the tip convolution, which is certainly high for such small lateral structures, we have estimated that they represent only 5% of the total coverage for 0.7 ML. The highest coverage studied here is inferior to 0.8 ML to maintain the islands well separated. If the coverage is further increased, the islands coalesce and form a thin film. Magnetic measurements have shown that this transition takes place around 1.5 ML [Padovani et al., 1998]

In mean, each island is composed by a number of atoms $N(t) = R \cdot t / n_i$, where n_i is the island density, t is the deposition time and R [atoms $\text{m}^{-2} \text{s}^{-1}$] is the deposition rate which is assumed to be constant. By increasing t the atoms contribute only to the islands lateral growth, since their height remains constant. STM permits to follow this evolution in details. Indeed, it is possible to perform statistical analysis on the nanoislands with height above a given thresh-

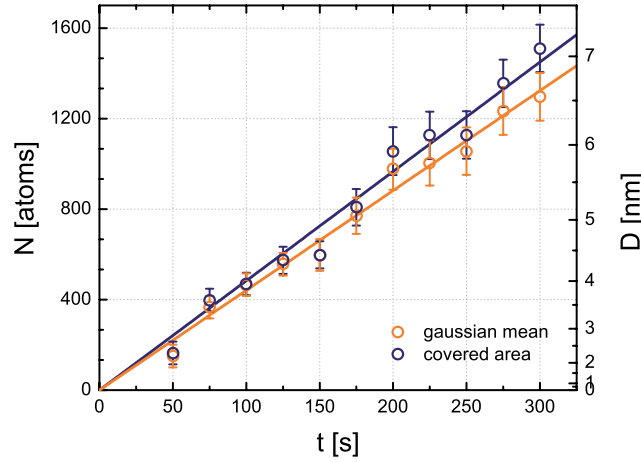


Figure 4.8: Variation of the mean number of atoms for Co nanoislands N and diameter D as a function of the deposition time t .

old. The mean area \bar{s} is then calculated by following two different routes.

1. By taking the mean of the gaussian curve that best fits the area distribution of the islands.
2. By measuring the area covered by the deposit and dividing it by the number of islands.

Most of the islands are bilayer but the presence of the third layer is also taken into account. This is done by assuming that the islands are ideally bilayer high, the third layer is then redistributed in the first two with the effect of slightly increasing the values of \bar{s} . The mean diameter D is obtained straightforwardly, approximating the shape of the islands to a disk. Then, from the mean area \bar{s} [nm²] it is possible to calculate N , the number of atoms present in each island:

$$N = \frac{4\bar{s}}{a_{\text{Co}}^2 \cdot \sqrt{3}}, \quad (4.1)$$

where $a_{\text{Co}} = 0.251$ nm is the bulk lattice parameter of Co and in the factor 4 the bilayer height of the islands is taken into account. The final value of N is then obtained with a linear interpolation of the calculated values for different t . The results are reported in Fig. 4.8. As can be seen, the two procedures give similar values: the growth rates of the islands differ by only 10% (4.4 vs 4.8 atoms/s). The islands grown here have a mean diameter in the range 2÷7 nm and each one is composed by a number of atoms that vary from 200 up to 1600.

In Sec. 4.3.1, this STM analysis will be coupled with MOKE measurements

to study how the magnetization reversal takes place depending on the island size.

4.2.2 Co nanoislands with elongated shape

In the following we investigate to what extent Au(111) with linear reconstruction may be used as a template for self-organizing wires or chains of Co dots. We successfully produced new elongated-shaped islands of cobalt following two different routes.

4.2.2.1 Growth at low temperatures

To obtain an Fig. 4.9 shows STM images of the Au(111) surface with unidirectional reconstruction onto which low Co coverages (θ_{Co}) were deposited in a wide range of temperatures ($50 \text{ K} < T < 300 \text{ K}$). When the deposition of 0.25 ML of Co is carried out a room temperature (Fig. 4.9a) all the diffusion channels are clearly activated. Due to the long diffusion length at this temperature, the adatoms are eventually pinched at the defects of the surface. As a consequence, the Co self organization is found to be seriously modified in these sample as compared to the herringbone reconstruction [Voigtländer et al., 1991a]. While the profile analysis indicates that the islands retain the usual bilayer height, the absence of the elbows in the reconstruction makes the islands loose both their regular spacing and their narrow size distribution.

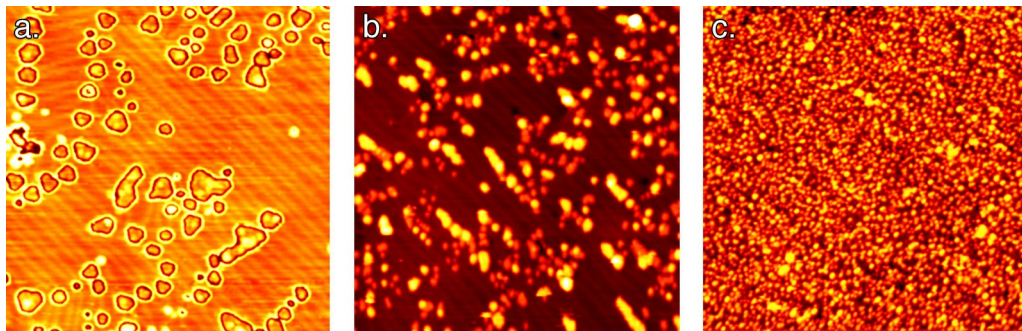


Figure 4.9: STM images of Co deposited at different temperatures on Au(111) with unidirectional reconstruction ($90 \times 90 \text{ nm}^2$). All the images are recorded at the deposition temperature. a. $T = 296 \text{ K}$, $\theta_{\text{Co}} = 0.25 \text{ ML}$, isotropic diffusion; this image has been treated in order to enhance the contrast on the substrate. b. $T = 105 \text{ K}$, $\theta_{\text{Co}} = 0.15 \text{ ML}$, anisotropic diffusion that leads to elongated islands. c. $T = 50 \text{ K}$, $\theta_{\text{Co}} = 0.15 \text{ ML}$, statistical growth.

anisotropic diffusion we reduced the temperature of the substrate at 105 K. As can be seen in Fig. 4.9b, Co ($\theta_{\text{Co}} = 0.15$ ML) forms islands elongated along the reconstruction direction, long up to 20 nm and displaying a mean aspect ratio equal to 5. The nucleation of this kind of islands takes place on the fcc zone of the reconstruction. From these observations we can deduce that at this temperature the diffusion is anisotropic and that the discommensuration lines act as energy barriers, repelling the diffusion of Co adatoms [Fischer et al., 1999]. In contrast, molecular dynamics has shown that the discommensuration lines act as attractors for Co adatoms [Goyhenex and Bulou, 2001; Bulou and Massobrio, 2004] and constitute a favorite path to the kink sites, where Co nucleates and grows. Due to the reduced mobility of adatoms, impurities and reconstruction defects constitute traps even more efficient than at room temperature. As a result, besides elongated islands also very small clusters of Co nucleate, leading to a wide distribution of island size and shape. It is the same type of defects, probably impurities, that behave as nucleation sites at 300 K (Fig. 4.9). We believe that these impurities are not only intrinsic, but are also caused by the fact that the same template has been used several times to perform experiments at various temperatures. The etching procedure applied between one deposition and the other to sputter away the Co atoms was minimized, so that the entire Au film is not fully etched away. Probably this leaves Co impurities at the surface, which upon annealing, are known to embed themselves in the uppermost plane of Au atoms, creating nucleation sites for the next deposition. It is therefore likely that deposition at 105 K on a fresh template yields more homogeneous and elongated islands. A situation similar to this one is observed if the deposition is carried out at 135 K.

As expected, if we further decrease the temperature of deposition down to 50 K ($\theta_{\text{Co}} = 0.15$ ML), the diffusion of adatoms is completely frozen and a statistical growth is observed. As shown in Fig. 4.9c, monolayer-thick islands with lateral size of few Å nucleate at spatially random locations with a high density [Padovani et al., 2000].

4.2.2.2 Growth on Au-Pt surface alloy

The temperature control over the diffusion barrier is an elegant way to drive the self-assembly of nanostructures, and we successfully employed it to grow elongated islands in the present case. However the high density of extrinsic defects on the surface disturbs the diffusion of Co adatoms preventing a homogeneous growth. In order to have a better control of the number of nucleation centers on the surface, Pt appears to be a proper candidate to elaborate a prepatterned surface [Nahas et al., 2010]. Fig. 4.10a shows an STM

image of 0.05 ML of Pt deposited on Au(111). Pt is miscible with Au and a previous study showed that, when deposited at room temperature on Au(111), Pt substitute Au atoms in the top layer [Pedersen et al., 1999]. Since at room temperature the Au surface could accumulate a maximum of 0.03 ML of Pt, we increased the substrate temperature to 400 K to favor the exchange of Pt with Au atoms. The embedded Pt atoms are imaged darker than the surrounding Au atoms, with an apparent height difference of 0.2 \AA with respect to the mean surface level. As a detrimental consequence of alloying, Au atoms are ejected from the surface and forms islands 2.35 \AA high that may perturb the regularity of the reconstruction. More importantly, Pt atoms alloying does not occur randomly on the surface but it takes place preferentially in the discommensuration regions (See inset of Fig. 4.10a). Thus the surface alloy could be regarded as a patterned surface in which Pt atoms constitute trapping sites that may permit to trigger the nucleation of Co. The ability of a seed layer to guide the growth of materials that otherwise do not show any order has been shown also for Pd on Ni₃Al(111) [Schmid et al., 2007] or Ir on graphene/Ir(111) [N'Diaye et al., 2009].

This is confirmed in Fig. 4.10b, where 0.15 ML of Co were deposited at room temperature on Au(111) prepatterned with Pt. Since the diffusion of adatoms is quenched by the presence of Pt atoms, Co islands nucleate with a high density in the form of monolayer islands with a mean lateral dimen-

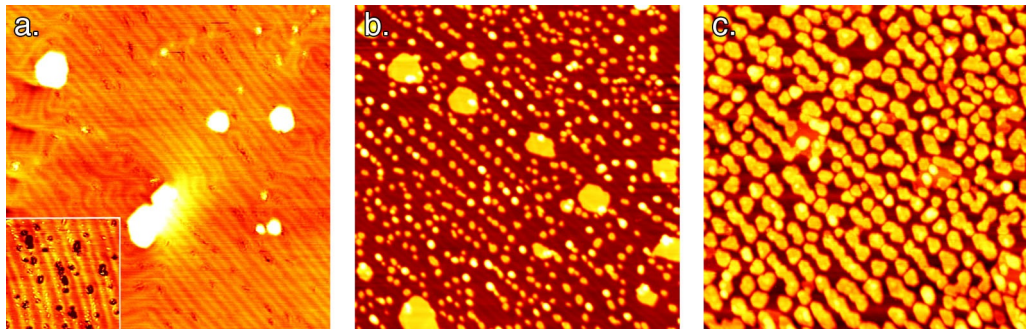


Figure 4.10: a. STM image of Pt ($\theta_{\text{Pt}} = 0.05 \text{ ML}$) deposited at 400 K on Au(111) with unidirectional reconstruction; the Pt is embedded in the surface and follows the reconstruction lines. In inset, zoom ($32 \times 32 \text{ nm}^2$) showing dark patches corresponding to Pt inserted atoms. b. ($\theta_{\text{Co}} = 0.15 \text{ ML}$) and c. ($\theta_{\text{Co}} = 1.1 \text{ ML}$), STM images of Co deposited on Pt/Au(111): Pt acts like preferential nucleation sites for Co that forms small and separated islands at low Co coverage (b.), that coalesce when the Co coverage is increased (c.). All the images are $100 \times 100 \text{ nm}^2$ and recorded at room temperature.

sion of 1 nm. Co follows the order imposed by the previous Pt deposition and forms hemispherical islands aligned along the reconstruction lines and not on the fcc stacking regions as we observed in the low-temperature growth. The deposition of Co highlights the tendency of Pt to nucleate in one over two discommensuration regions, as be seen in Fig. 4.10a. When θ_{Co} is increased, the islands grow first vertically, adopting the usual bilayer height, and then laterally (Fig. 4.10c). During this process the clusters percolate and, thanks to the small distance between islands on the same reconstruction line, they form islands often very elongated along the reconstruction direction, with an aspect ratio up to 8. In some other cases, even if two islands come very close together, the percolation does not take place probably due to an incommensurate growth of the islands [Fruchart et al., 2003]. This is observed even more systematically on Au(111) with herringbone reconstruction, and it is why the magnetic transition of Co nanoislands to ferromagnetic films happen only at 1.5 ML. The problem of incommensurate growth in this case seems to be less stringent and several island can coalesce together, as can be seen in Fig. 4.10c. Another relevant difference with Au(111) with herringbone is that the coalesce takes place in the same direction also at a macroscopic scale. This is due to the fact that the direction of the reconstruction is maintained fixed all over the sample, if surface defects are neglected. As an important consequence, the nanoislands are preferentially elongated along the same axis. Significantly, this permits to macroscopically measure the properties of such anisotropic objects along different directions. When applied to freshly re-prepared samples of uniaxial Au(111) reconstruction, the two procedures applied above (low temp deposition or Pt seeding) should provide efficient methods to fabricate uniaxial nanostructures of various materials on a macroscopic scale. No linear template with such a large period has been reported yet starting from nominally-flat surfaces.

4.3 Magnetism of Co on Au(111)

For an improved development of magnetic nanoparticles for magnetic recording technology it is necessary to get a deeper understanding of their rich magnetic behavior. This strongly depends on their size, shape and composition drastically differing from that of bulk magnets. With this purpose we studied the magnetism of Co/Au(111), that is an ideal system thanks to the high degree of order inherent of self organization. The islands show a superparamagnetic behavior with an out-of-plane magnetization and are magnetically independent of each other.

4.3.1 Magnetism of Co nanoislands as a function of their size

As shown in the previous section, the size of Co nanoislands on Au(111) can be finely tuned simply, by increasing the deposition time. The magnetic susceptibility of these particles has been studied in the diameter range of 2–7 nm (200–1400 atoms). The upper limit of this range, as cited previously, was chosen well below the coalescence regime, in order to study only the superparamagnetism of isolated particles. In fact, considering the islands height and their perpendicular magnetization, we can neglect the dipolar coupling ($\mu_0 H \approx 40$ mT) with respect to the magnetic anisotropy energy ($\mu_0 H_{\text{an}} \approx 5$ T). The real parts of the experimental dynamical susceptibility χ' (in open symbols) for nanoislands with N regularly increased are shown in Fig. 4.11. The position of the χ' peak does not bring any direct quantitative physical information about the mean blocking temperature since it depends from the size dispersion of the particle (as shown in 2.6b). The relevant quantity here is the mean activation energy for magnetization reversal E_a , that can be obtained by fitting the experimental curves with the model presented in Sec. 2.2.2. This combines the linear response theory of a two level system (Eq. 2.14) with a Gaussian distribution of the magnetic anisotropy E_a among the particle assembly (Eq. 2.19). The attempt frequency ν_0 was taken as 40 GHz and the number of atoms N inside each particle is the one deduced from the STM study (Sec. 4.2.1). In particular we choose to use the values of N as deter-

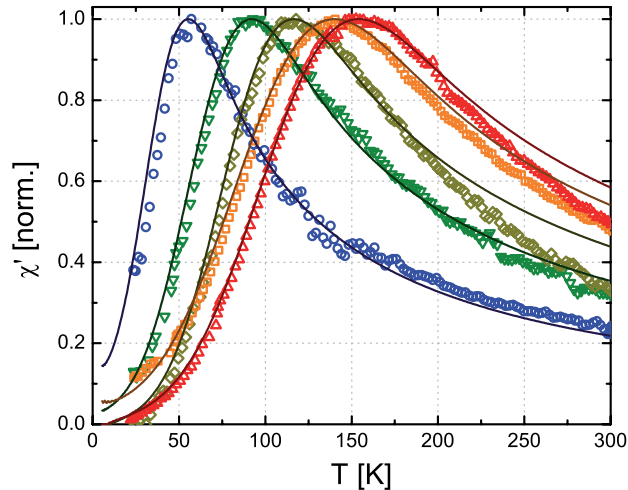


Figure 4.11: Real part of the experimental dynamical magnetic susceptibility χ' as function of temperature for different mean Co nanoisland sizes (3.3, 4.3, 5.1, 5.7, and 6.3 nm from left to right).

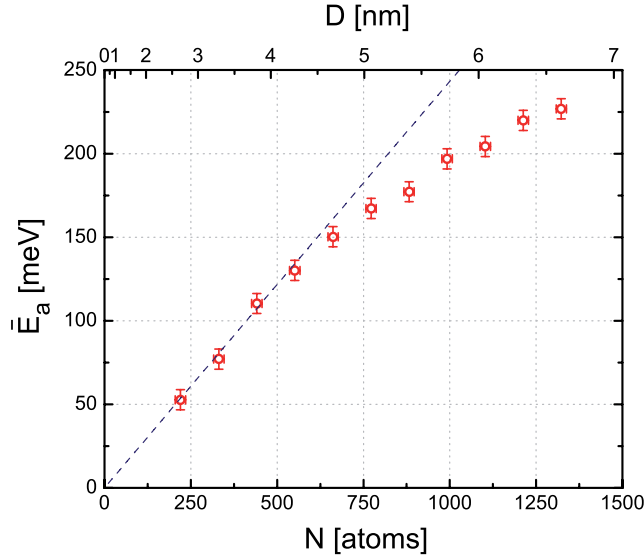


Figure 4.12: Average activation energy \bar{E}_a as a function of the average atom number per Co nanoisland N .

mined by gaussian fit of area distribution, we can assume that this is directly connected to the distribution of magnetic anisotropy used to fit the susceptibility curves. Thus the only free parameters regard the magnetic anisotropy distribution: the mean \bar{E}_a and the standard deviation σ . These values are the result from the fit, typically $\sigma/\bar{E}_a \approx 0.3$. The experimental values of the susceptibility curves and the corresponding theoretical fits are shown in Fig. 4.11 for nanoislands with N regularly increased.

In Fig. 4.12 is shown how the average activation energy for magnetization reversal \bar{E}_a as a function of the average atom number per island. As can be clearly seen, this does not scale linearly with N , in opposite with the macrospin expectation with homogeneous anisotropy. In fact, whereas it increases linearly for small sizes (almost 0.3 meV/atom) it is deviating for larger sizes ($N \gtrsim 500$ atoms, $D \gtrsim 4$ nm), which have smaller activation energies than predicted from the Néel-Brown model. For the largest N measured here ($N = 1330$ atoms), the discrepancy is around 30 %. It is worth noting that this behavior could be described in terms of an enhanced anisotropy at the edge atoms [Rusponi et al., 2003], the activation energy assumes the expression $E_a = P \cdot K_{\text{edge}}$, where P is the number of perimeter atoms. However, as it will be shown in the following, this result rather indicates a deviation from the macrospin model. Indeed, this behavior can be perfectly reproduced with an out-of-plane homogeneous anisotropy and considering the important role of thermally excited magnetic modes on the reversal process.

4.3.2 From uniform rotation to spin-wave assisted reversal

To understand the physical reason for the discrepancy between the experimental results and the macrospin expectations it is necessary to go beyond this latter picture. The macrospin approximation, by building a unique magnetic moment, neglects all the degrees of freedom and the excitations (notably thermal) inside the nanoparticles. To authorize also these possible fluctuations we have collaborated with S. Rohart and A. Thiaville at the Laboratoire de Physique des Solides in Orsay² to develop a new theoretical model where each atom composing the island is individually described. In this way it is possible to study in more details the intrinsic dynamical character of magnetical reversal.

The magnetic nanoislands are described at the atomic scale using a Heisenberg Hamiltonian including all the magnetic energies (Zeeman, exchange coupling, crystalline anisotropy and dipolar coupling terms) [Rohart et al., 2007]:

$$E = -\mu_0\mu_{\text{at}}\mathbf{H}\sum_i \mathbf{m}_i - J \sum_{\langle i,j \rangle} \mathbf{m}_i \cdot \mathbf{m}_j - \sum_i k_i (\mathbf{m}_i \cdot \mathbf{e}_i)^2 - \sum_{i,j \neq i} \frac{\mu_0\mu_{\text{at}}^2}{8\pi} \left[\frac{3(\mathbf{m}_i \cdot \mathbf{r}_{ij})(\mathbf{m}_j \cdot \mathbf{r}_{ij})}{r_{ij}^5} - \frac{\mathbf{m}_i \mathbf{m}_j}{r_{ij}^3} \right], \quad (4.2)$$

where \mathbf{m}_i is the atomic magnetic moment unit vector on site i , μ_{at} the atomic magnetic moment and \mathbf{r}_{ij} is the vector connecting sites i and j . The magnetization dynamics is derived by integrating the Landau-Lifshitz-Gilbert equation:

$$\frac{d\mathbf{m}_i}{dt} = \gamma_0(\mathbf{H}_i^{\text{eff}} + \mathbf{h}_i(t)) \times \mathbf{m}_i + \alpha \mathbf{m}_i \times \frac{d\mathbf{m}_i}{dt}. \quad (4.3)$$

The effective field $\mathbf{H}_i^{\text{eff}}$ acting on the magnetic moment \mathbf{m}_i comes from Eq. 4.2:

$$\mathbf{H}_i^{\text{eff}} = -\frac{1}{\mu_0\mu_{\text{at}}} \frac{\partial E}{\partial \mathbf{m}_i}. \quad (4.4)$$

Moreover, in Eq. 4.3 thermal effects are included with the addition of a random field with a white spectrum (Eq. 2.10) as proposed by Brown and described in Sec. 2.2.1.

The parameters used are $\mu_{\text{at}} = 2.1 \mu_{\text{B}}/\text{atom}$, exchange constant $J = 29 \text{ meV}/\text{bond}$ [Šipr et al., 2007] and damping factor $\alpha = 0.2$ [Respaud et al., 1999]. The magnetic anisotropy, oriented along the dot axis, has been taken homogeneous over the whole particle: $K = 0.4 \text{ meV}/\text{atom}$. Taking into account the shape

²<http://www.lps.u-psud.fr>

anisotropy [Rohart et al., 2007], the activation energy for a coherent magnetization reversal is about 0.3 meV/atom, as observed in the low diameter range of the experimental study of the previous section. Eleven particles have been studied from 1 to 1459 atoms ($D = 0.2 - 10.1$ nm). To get a reasonable calculation time, single layer nanoislands with a circular shape are considered, the atoms being on a hexagonal lattice. The program has been tested with a single atom particle, for which an analytical solution is possible Brown [1963]. In this case the Maxwell-Boltzmann distribution is recovered and the Eq. 2.11 are verified [Vouille et al., 2004].

At zero temperature behavior of the islands as simulated is well described by the macrospin model. If the magnetic field is applied along the easy axis the

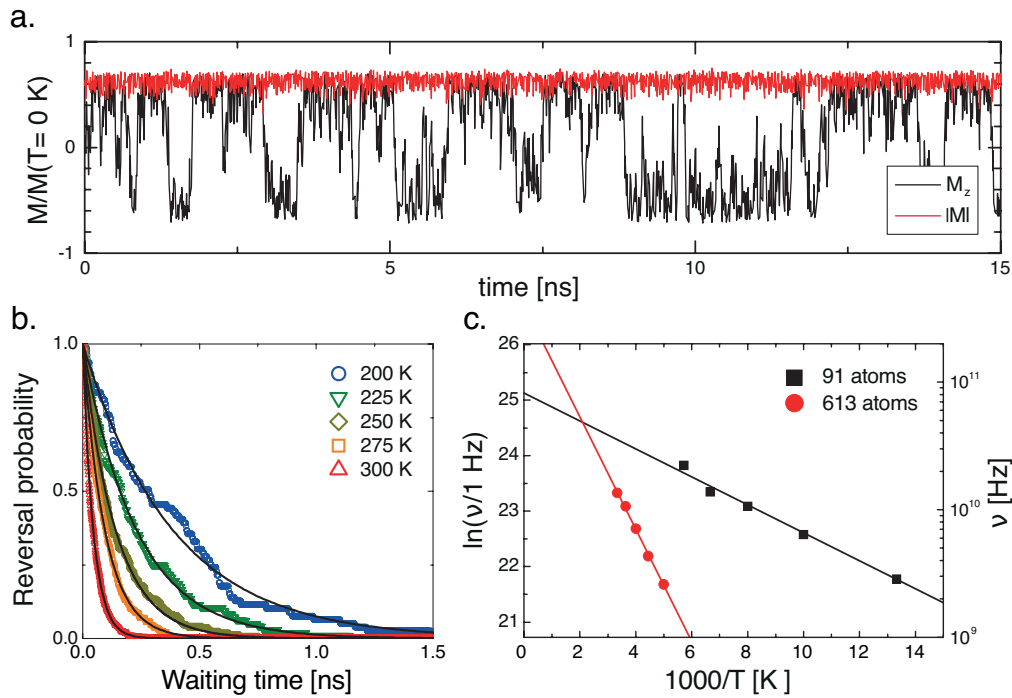


Figure 4.13: a. Time dependence of the magnetization in a nanoislands composed of 613 atoms at 200 K as obtained from simulations. The red curve represents the magnetization modulus while the black curve the component of magnetization along the easy axis z , which shows a telegraph noise. In both cases the quantity were normalized with respect to the values at zero temperature. b. Waiting time analysis performed on the same island but at different temperatures. The full lines correspond to exponential decay fits. c. Arrhenius plot of the switching rate for two particles, composed of 91 and 613 atoms.

switching field corresponds exactly to the anisotropic field (Eq. 2.5), indicating that the reversal takes place by coherent reversal. The magnetic fluctuations have been simulated at finite temperature and in zero applied field in a time window of the order of 10 ns. A typical example is reported in Fig. 4.13a. In this condition a reduction of magnetization modulus is observed indicating that the nanoisland is in a magnetic excited state. Above a threshold temperature, which can be regarded as the blocking temperature, superparamagnetic fluctuations are observed, giving rise to a telegraph noise for the magnetization component along the easy axis M_z . During the magnetization reversal the modulus of the magnetization $|\mathbf{M}|$ remains constant which suggests a coherent magnetization reversal. Moreover the magnetization amplitude is reduced with respect to $T = 0$ K, mainly because temperature induces incoherent fluctuations from one spin to the other. The telegraph noise permits to perform a waiting time analysis [Wernsdorfer, 2001], which consists in measuring the probability p that the magnetization has not switched after a certain time t : $p(t) = e^{-t/\tau}$ (as shown in Fig. 4.13b). τ , the lifetime between switching events, is the inverse of the switching rate ν (Eq. 2.8). If this procedure is repeated at different temperatures, we get the Arrhenius law $\nu = \nu_0 \exp(-E_a/k_B T)$, from which both the activation energy for reversal E_a and the attempt frequency ν_0 are obtained. For all the particles studied the Arrhenius law behavior is observed, as shown in Fig. 4.13c.

In the case of a single atom particle the activation energy ($E_a = 0.39$ meV) well corresponds to the magnetic anisotropic energy ($K = 0.4$ meV/atom). For larger islands if $N \lesssim 100$ atoms the activation energy still coincides with the anisotropic energy as typical for the macrospin magnetization reversal $E_a = N \cdot K$, while for larger particles a significant deviation is found and the variation of E_a follows a power law ($E_a \propto \sqrt{N}$). This result is qualitatively in good agreement with the experiments. However, due to the monolayer height in the simulations, the number of atoms, above which deviations to the macrospin model are observed, is different from the experiments. As we will show in the following, the key parameter is rather the diameter. This provides a much better agreement between experiments (deviation above ~ 4.5 nm) and simulations (~ 3.5 nm).

What is the origin of the deviation from the expected activation energy? A possible answer to this question might be given by continuing to admit the validity of the macrospin model. In this way, the activation energy for magnetization reversal continues to follow the expression $E_a = N \cdot K$ and the observed trend could be explained with a decreasing of the magnetic anisotropy K in large nanoisland. The origin of this effect can be ascribed to thermal excitations which arise when the lateral size of the islands is increased. This destabilize the magnetic order and induces a magnetization reduction and also

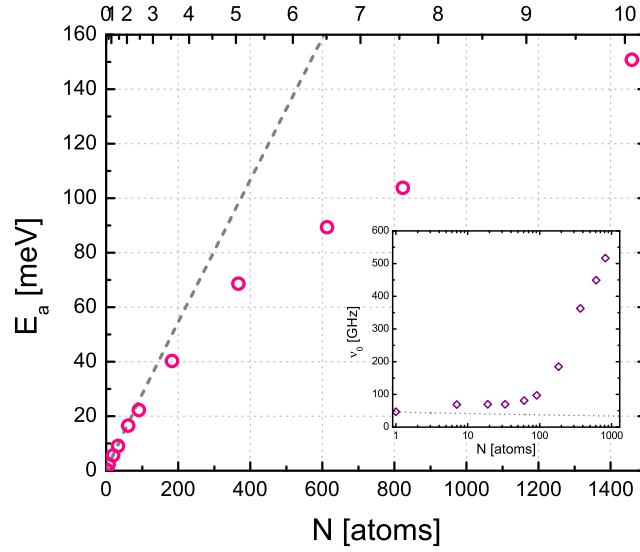


Figure 4.14: Average activation energy E_a as a function of the average atom number N per simulated Co nanoslands. The dotted line corresponds to the macrospin expectation.

a decreasing of K , according to the expression $K(T) = K(0) \cdot (M_s(T)/M_s(0))^3$ [Callen and Callen, 1966]. The value of K can also be estimated from the precession frequency of the magnetization f . Indeed at zero applied field $2\pi f = \gamma_0 H_{an}$ and, by substituting the expression for anisotropic field (Eq. 2.5), we get:

$$K = \frac{\pi \mu_{at} f}{\gamma_0}. \quad (4.5)$$

This permits to find the value of K independently from the activation energy E_a . In order to study the magnetization dynamics, simulations have been performed at reduced temperatures where no superparamagnetic fluctuations are observed. The frequency content of the magnetization dynamics were studied by calculating the power spectra density (PSD) of the in-plane magnetization component M_{xy} :

$$S_{M_{xy}}(f) = \lim_{T \rightarrow \infty} \frac{1}{T} \left\langle \left| \int_{-T/2}^{T/2} M_{xy}(t) \exp(-i2\pi f t) dt \right|^2 \right\rangle. \quad (4.6)$$

The presence of a peak in the spectra indicates the excitation of eigenmodes in magnetization dynamics (and notably the precession mode), while incoherent thermal fluctuations contribute to the background noise. We will now

consider two nanoislands with different sizes ($N = 61, 367$ atoms) and identical reduced temperature (as compared to the anisotropy energy). The two nanoislands are chosen in such a way that the activation energy for magnetization reversal follows and deviates from the macrospin prediction. Moreover, the spatial distribution of the eigenmodes can be studied by plotting the intensity of the PSD at a given frequency f for each atom composing the particle. As can be seen in Fig. 4.15a, in the case of smaller island the precession mode is lower at the edge atoms than at the center, what can be ascribed to dipolar couplings. This mode takes place at a frequency $f = 129$ GHz in agreement with the macrospin expectation $\gamma_0 H_{\text{an}}/2\pi = 130$ GHz. By substituting this value in Eq. 4.6 one gets $K = 0.28$ meV/atom, which coincides with the value obtained with E_a . In the case of the bigger island the precession mode is found at lower frequency $f = 116$ GHz which gives $K = 0.25$ meV/atom. On the other hand, from the activation energy we obtain $K = 0.18$ meV/atom. The

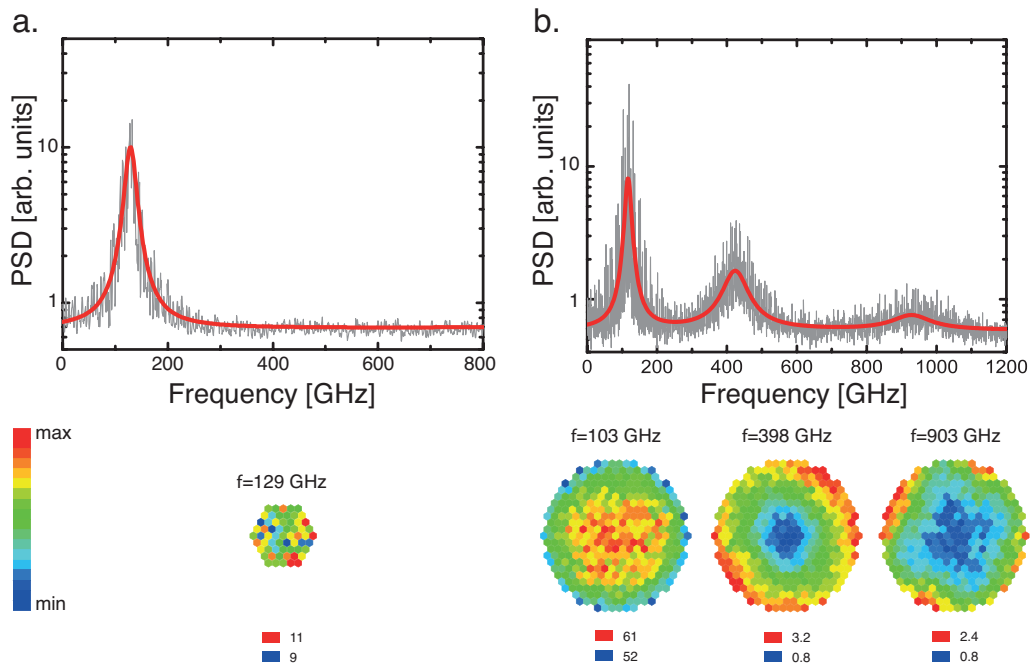


Figure 4.15: Fourier transform of the in-plane component of a single spin extracted from the magnetization fluctuation on a a. 61-atom nanoisland at 10 K and a b. 367-atom one at 50 K. In the first case all the composing atoms show the same spectra, while in the second case the two peaks at high frequency are characteristic of edge atoms. The full (red) lines are multiple Lorentzian fits. Below, for each peak (eigenmode) is reported the cartography of the PSD.

lack of coherence between the two determinations is not acceptable: it is thus inadequate to preserve the macrospin validity and assume a decrease of K . Moreover, the deviations from the macrospin model are not only seen from the activation energy, but also from the attempt frequency ν_0 (inset of Fig. 4.14). This according to Brown's model (Eq. 2.11) is proportional to $K^{3/2}$ and thus this formula predict a decrease of ν_0 and cannot account for the huge increase of ν_0 obtained from the calculation. For our parameters ν_0 is expected to be 40 GHz, a value perfectly reproduced by the one atom simulation. Up to 100 atoms ν_0 is slightly larger (70-100 GHz) and the a very important increase is observed with frequencies of several hundreds of GHz. All these considerations forbid constructing an effective macrospin model for this system.

The deviation from the macrospin model is due to the thermal excitation of spin-wave modes inside the nanoislands. These appear as new peaks at higher frequency (see Fig. 4.15b). The eigenmode active at $f \simeq 400$ GHz is a spin-wave mode since the precessions of two symmetric spins with respect to the dot axis show a π phase shift and cancel when averaging the effect on the whole particle. The second spin-wave mode (at $f \simeq 900$ GHz) is also antisymmetric but is characterized by the presence of two nodal planes. In both these modes the intensity of PSD is enhanced at the edge atoms and is nearly zero at the center of the island, the comparison of the two first modes shows that the edge localization increases with the order of the mode. The shape of these modes is in good agreement with a previous calculation on a similar system [Lévy et al., 2006].

As spin-wave modes in nanoislands are confined, the energy needed to create inhomogeneous modes is inversely proportional to a power of D , depending on the pinning conditions at the particle edge [Mercier et al., 2000]. This explains why spin-wave modes can be observed only above a critical diameter for a given temperature. Magnetization reversal is a collective effect over the whole island so that only the precession mode is directly related to the reversal. However, spin-wave modes can act as an energy reservoir and this provokes an increase of the switching rate that appear as both an increase of ν_0 and a decrease of E_a .

In conclusions by increasing the size of the island and the temperature of the system, internal degrees of freedom are activated. This causes a temperature dependence of the activation energy for reversal E_a which invalidates the Néel-Brown formula 2.11. As a further consequence ν_0 loses its physical meaning of attempt frequency and could explain the unrealistic values observed.

4.3.3 Magnetism of Co nanoislands with elongated shape

In the previous section, we pointed out the influence of thermally excited modes on magnetization reversal of compact nanoislands. In the case of elongated particles, the influence of these thermal fluctuations has been demonstrated to be even more important. In fact, Braun have shown theoretically that nanowires whose length exceeds the width of a domain wall the magnetization reversal occurs via nucleation and propagation of domain walls [Braun, 1993]. The activation energy is then no longer proportional to the volume as in the Néel-Brown theory, but proportional to the cross-sectional area of the particle. This prediction was confirmed for nanowires with diameter in the range of 6-50 nm [Paulus et al., 2001].

For this reason, we have investigated also the magnetic behavior of the elongated Co nanoislands. In particular, the islands were grown using a seed layer of Pt (as described in Sec. 4.2.2.2), in order to avoid Ostwald ripening up to 300 K. The real part of the experimental dynamical susceptibility χ' is reported in Fig. 4.16 together with the theoretical fit. This gives as result an energy of activation of 168 meV. To compare this value with the results obtained for compact nanoislands it is necessary to estimate the number of atoms N . This task is complicated by the size polydispersity of the nanoislands. If the size distribution is fitted with a single gaussian we found that each island is composed of around 600 atoms. The comparison with Fig. 4.12 then shows that the mean

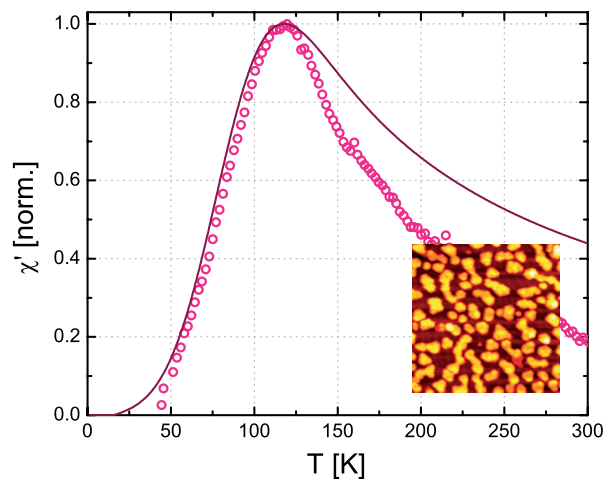


Figure 4.16: Real part of the experimental dynamical magnetic susceptibility χ' as function of temperature for Co nanoislands with elongated islands. In inset an STM image of the measured sample is shown.

activation energy is similar in the cases of compact and elongated nanoislands (for $N \simeq 600$, \bar{E}_a is also close to the macrospin expectation). Nonetheless, with this procedure the impact of the bigger elongated nanoislands ($N \simeq 1800$ atoms) is neglected, which would lead to a significant lowering of \bar{E}_a . Even if the size distribution complicates the analysis, we can also get more insights by a more careful analysis of the susceptibility curve in Fig. 4.16. It is clear that the theoretical fit does not describe well the experimental trend. Indeed, while the first part of the curve (where the particles are in a blocked state) is well reproduced, the fit moves away from the data at higher temperature. We assign this difference to the thermal activation of other magnetization reversal modes, like nucleation and propagation of domain-wall. Thus, the differences between the magnetic behavior of compact and elongated islands emerge from this preliminary study. However, to get a more detailed comprehension of the magnetic behavior it is necessary a higher control on the growth of Co nanoislands, which will permit a more direct comparison between STM and MOKE measurements. On the other hand, the availability of islands with a wide distribution of size and aspect ratio could be exploited in local measurements like SP-STM.

4.4 Conclusions

In this chapter, we have described the growth and the magnetic properties of Co nanostructures on Au(111). This subject has been developed following two parallel routes. The former one is devoted to the study of islands with increasing size while the latter of islands with elongated shapes. These objectives are reached by following the same essential steps: the exploitation of a well-ordered template, the control of nucleation and growth of the islands and the magnetic characterization.

The growth of Co on Au(111) with herringbone reconstruction has been widely studied and is now understood in detail. For this reason our attention was concentrated mainly on the magnetic properties of this model system. By coupling STM and MOKE studies the magnetic behavior of the nanoislands was studied as a function of their size. Our results pointed out that the magnetism of this system cannot be described by constructing an effective macrospin for the system, since this model overestimate the thermal stability of nanoparticles with a diameter of few nanometers.

The nucleation and growth of Co on the new Au(111) surface with linear reconstruction has required a more profound work, due to the originality of our approach. The control on the adatoms diffusion permitted to obtain particles with a high aspect ratio. The same goal was reached also with the deposition

of a seed layer of Pt, which forms a surface alloy with Au preferentially on the discommensuration lines. Preliminary magnetic measurements on elongated islands have shown some difference with the case of compacted islands. However, more detailed studies are needed in order to understand how the elongated shape of nanoislands affects their magnetic behavior.

Metallic and molecular capping of Co nanostructures

Surface effects are of primary importance in determining the magnetic properties of ultrathin films and nanostructures and in particular their magnetic anisotropy. As a consequence, the magnetism of these systems can be strongly modified simply by replacing the vacuum-facing interface with a different one. The effect of a non-magnetic overlayer is manifold, including structural contributions such as strain, chemical intermixing, the surface roughness and morphology together with electronic contributions due to interfacial hybridization between the film and the overlayer.

In this chapter we study the influence of a metallic and a molecular capping on the magnetism of Co nanoislands and thin films on Au(111). In the first section the Co nanoislands are covered with platinum, a particularly interesting system since Co/Pt multilayers are promising candidates for high-density magnetic recording media. In the second section Co nanoislands and thin films are capped with *n*-dodecanthiols, a molecule capable to chemically bind with Co thanks to its thiol headgroup (-SH) and to self-assembly in compact monolayers.

5.1 Capping with a metal: core-shell Co-Pt islands

The coercivity and magnetic anisotropy of Co are significantly increased if noble metals are deposited on the top as overlayer [Beauvillain et al., 1994]. For thin films this effect has been extensively studied, due to the potential applications in high-density magnetic recording media. It is assumed that the major role in determining these changes is played by band hybridization at the interface [Engel et al., 1993]. In this framework Pt occupies a particularly important position since it is very close to satisfying the Stoner criterion and thus has a tendency to be magnetically polarized. Indeed, depth profile resolved X-ray Magnetic Circular Dichroism (XMCD) analysis have shown that Pt atoms in contact with a Co surface have a total magnetic moment of $0.61 \mu_B$ which decreases exponentially with the distance from the interface [Suzuki et al., 2005]. Moreover, other XMCD measurements indicated that the high spin-orbit coupling constant of Pt induces an enhanced perpendicular orbital momentum in Co atoms via the interface hybridization [Nakajima et al., 1998]. An analogous increasing of magnetic anisotropy would be interesting also for nanoparticles (forming core-shell structures), in order to enhance their thermal stability. Moreover, the coating of magnetic nanoparticles with inert metals prevents them from oxidation. Au capping was demonstrated to cause an increase of activation energy for magnetization reversal of sputtered Co nanoparticles with diameters ranging from 1 to 3.5 nm [Luis et al., 2006]. This effect was tentatively ascribed again to hybridization effects, but a more recent study showed that it is magnetoelasticity that plays a major role [Nahas et al., 2009]. Indeed, the Au overlayer induces a lattice dilatation in self-organized Co nanoislands, which can explain the change of E_a for different Au coverage. In this section we will study the case of a Pt overlayer, in order to clarify if the magnetoelastic term is the dominant one or if a more subtle interplay between different contributions is established (notably the interface hybridization, more important for Pt with respect to Au).

5.1.1 STM study of Pt growth on Co islands

The growth of Pt on self-assembled Co nanoislands has been studied by STM for the initial coverage of 0.5 ML of Co (Fig. 5.1a). The coverage of Pt overlayer was varied in the range of 0.5 to 2.5 ML. Fig. 5.1b displays a typical STM image of the system when half a monolayer of Pt is deposited. The original size and shape distribution of Co nanoislands remains practically unchanged. As shown in Fig. 5.1.1, Pt forms monolayer rims that completely surround all the

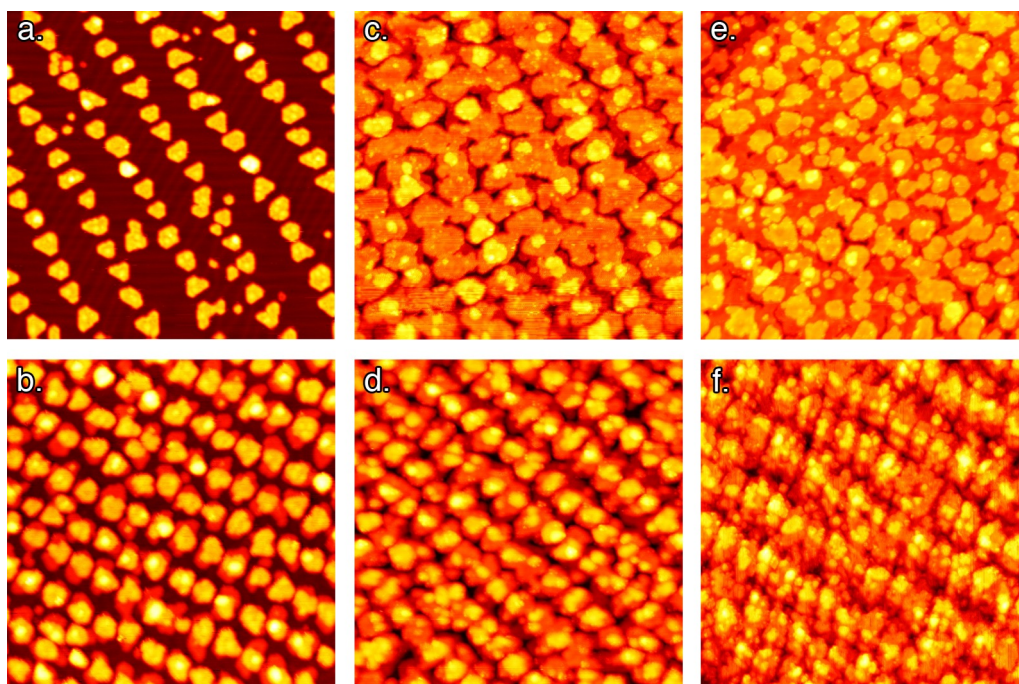


Figure 5.1: STM images ($100 \times 100 \text{ nm}^2$) showing the growth of Pt around and on the top of Co nanoislands. a. 0.5 ML of Co. b. 0.5 ML of Pt surrounding the Co islands. 1.5 and 2.5 ML of Pt deposited in one time (c,e) and in successive steps (d,f) on Co.

dots, whose height is around 2.4 \AA in accordance with the distance between two Pt(111) crystallographic planes [Hull, 1921]. At this stage the rims of adjacent islands begin to coalesce even if the typical shape is prevalently bulged in the direction perpendicular to the islands rows. A profile analysis suggests that the layer on the top of nanoislands is likely to be the third layer of Co rather than the Pt capping layer, the islands are thus uncovered.

A complete capping of the nanoislands is achieved if the Pt coverage is increased. This has been done by following two different routes: the first one consists in depositing at once the established coverage on different samples, while in the second one several successive depositions are performed on the same initial Co sample. Fig. 5.1c and d show STM images where 1.5 ML of Pt is deposited following these two different approaches. In both the location of the initial islands organization is still visible, but the morphology of the Pt overlayers is clearly different. If the deposition is completed in one single time Pt forms a quasi-continuous film 2 ML thick, the third and the first layer are also visible on the top and between Co nanoislands, respectively. It is to highlight here that a Moiré pattern is not observed on top of the Co islands, as it

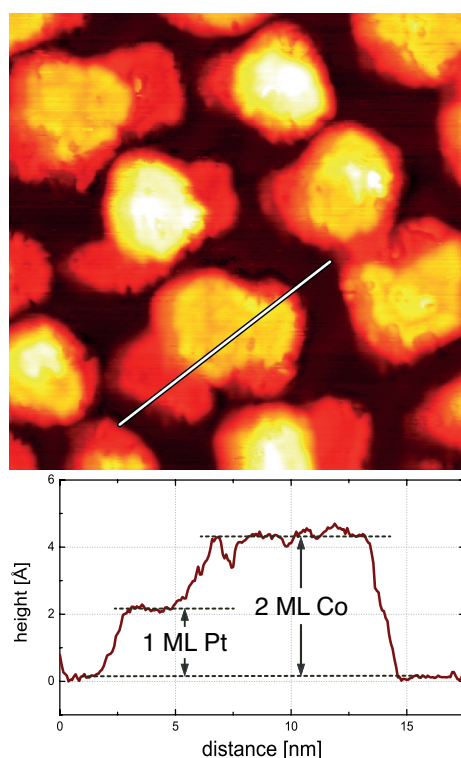


Figure 5.2: STM images ($30 \times 30 \text{ nm}^2$) and profile analysis of 0.5 ML of Pt on Co nanoislands.

happens for Au capping [Nahas et al., 2009]. On the other hand, if 1.5 ML of Pt are deposited in two successive steps the capping is less uniform. These differences are even more visible in the case of 2.5 ML thick Pt layer. If the deposition is performed in one single time (Fig. 5.1e) the growth proceeds clearly with a layer-by-layer mode, while in the successive deposition case (Fig. 5.1f) the Pt layer shows high roughness and protrusions with undefined height, symptoms of a non-perfectly crystalline atomic arrangement. We believe that the reason for this difference relies on the well-known miscibility of Co and Pt. If the deposition of Pt is done in multiple steps the system has enough time to evolve towards thermodynamical equilibrium and naturally mixes [Arbiol et al., 2005]. This induces disorder at the Co/Pt interface, disturbing the packing of the Pt atoms. Reasonably, the alloying process occurs faster in the case of a submonolayer coverage of Pt, since most atoms at the interface are undercoordinated. On the contrary, mixing is slowed down if the deposition is completed in one single time, probably because Pt atoms are well-arranged in the crystalline lattice as the STM images show. A schematic representation of how the morphology of Pt capping layer changes with the coverage θ_{Pt} is reported in Fig. 5.3.

5.1.2 Magnetism of Co-Pt core-shell nanoislands

The magnetic properties of core-shell Co-Pt nanoislands have been investigated by measuring their magnetic susceptibility as a function of the temperature. The experimental data, the corresponding theoretical fits (Sec. 2.2.2) and the corresponding activation energy for magnetization reversal are shown in Fig. 5.4.

In the case of single Pt depositions the capping causes a initial decreases of the transition temperature between ferromagnetic and superparamagnetic states

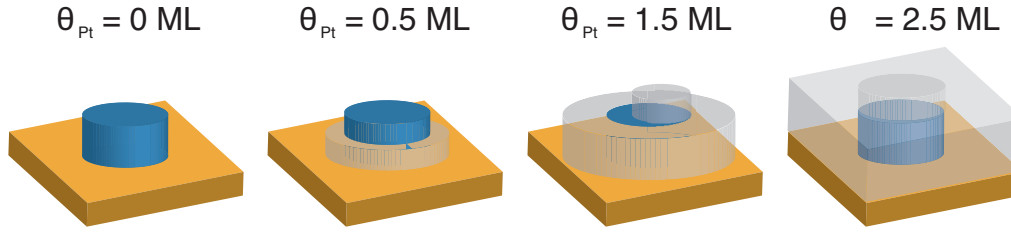


Figure 5.3: Schematic representation of the Pt capping layer disposition around and on Co nanoislands at different coverages.

which increases afterwards, if more than 1 ML of Pt covers the islands (Fig. 5.4a). This trend is clearly visible if the energy activation for magnetization reversal E_a is plotted as a function of Pt coverage θ_{Pt} , as in Fig. 5.4b. The presence of Pt rims around Co nanoislands reduces \bar{E}_a of around 15%. On the contrary, supramonolayer coverages increase considerably the activation energy, up to $\sim 35\%$ for $\theta_{Pt} = 2.5$ ML ($\bar{E}_a = 250$ meV). In the case of successive depositions the effect is similar qualitatively but quantitatively is significantly reduced. As can be observed in Fig 5.4c, the susceptibility curves are nearly superposable. The fitting results show that after the first reduction, \bar{E}_a increases but without overcoming the initial value (Fig. 5.4d). However in this case all the fitted values are within the experimental uncertainty.

Before analyzing the evolution of magnetic behavior of core-shell Co/Pt nanoislands, we will try to explain the reason of the difference between the cases of single and successive Pt depositions. We propose that this is again caused by Co-Pt alloying at the interface, that occurs to a greater extent if the system is given more time to evolve. $Co_{1-x}Pt_x$ nanoislands are characterized by a lower activation energy for magnetization reversal since Pt essentially reduces Co islands out-of-plane magnetic anisotropy [Moreau, 2010]. This differs from the increasing of \bar{E}_a obtained with an abrupt Co/Pt interface, as supposed if the deposition is carried in one single time.

It is here to highlight that the evolution of \bar{E}_a with Pt coverage is opposite to what observed with Au capping [Nahas et al., 2009]. In that case \bar{E}_a increases with submonolayer range and decreases with supramonolayer Au coverages. Molecular dynamics simulation showed that Au encapsulation induces a dilatation of Co lattice that can explain this trend. If the nanoislands are surrounded by a Au rim the strain acts mostly in-plane, causing a increasing of magnetic anisotropy, while if they are completely covered an additional vertical dilatation occurs and the overall effect is a decreasing of the anisotropy. It is likely that magnetoelasticity have an important impact also in the present case. If so, the observed trend could be explain qualitatively simply by an in-

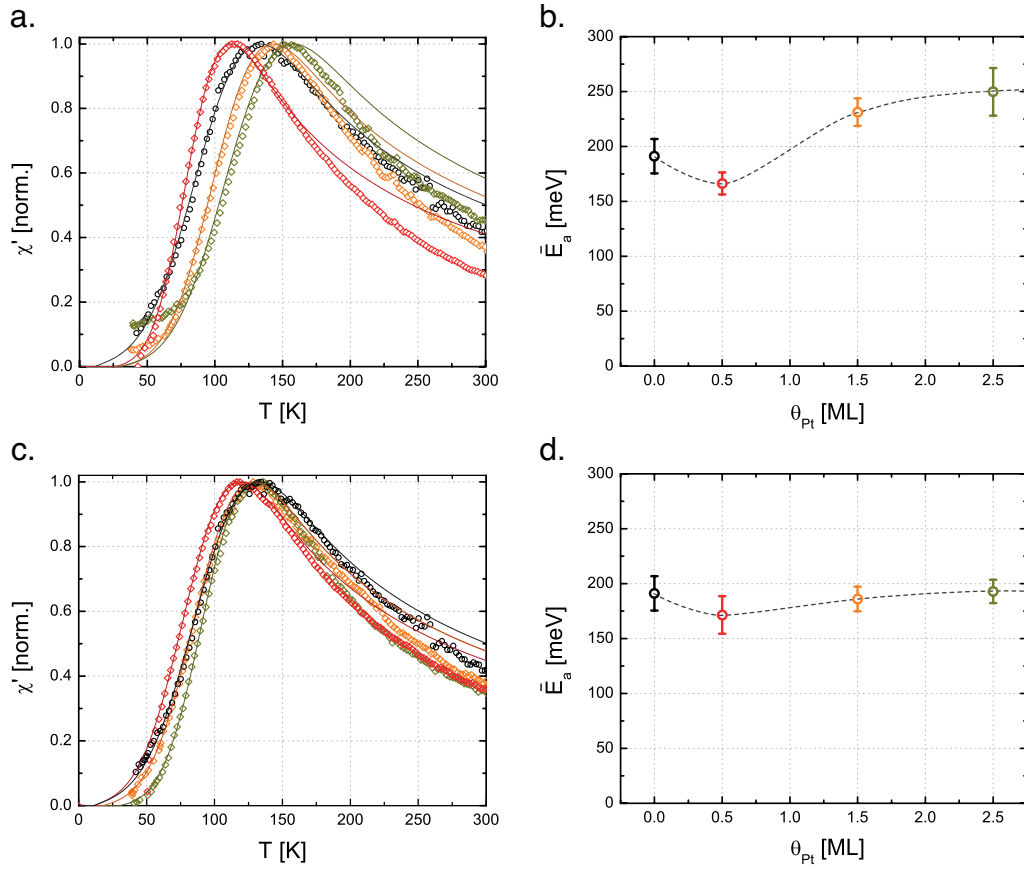


Figure 5.4: a,c. Real part of the magnetic susceptibility of a 0.5 ML Co upon which different coverages of Pt were deposited in single (a) or separate (c) depositions. b,d. Energy of activation for magnetization reversal as a function of Pt coverage in the the cases of single (b) and separate (d) depositions; the dashed lines are drawn as a guide for the eye.

duced contraction of the Co lattice in place of a dilatation. However this phenomena is quite unlikely and is also contradicted from Extended X-ray Absorption Fine Structure measurements performed at Soleil synchrotron¹. For pure Co the lattice parameters were found to be $a_{Co} = 2.51 \text{ \AA}$ and $c_{Co} = 4.07 \text{ \AA}$ while if Co is capped with 2.5 ML of Pt $a_{Pt/Co} = 2.55 \text{ \AA}$ and $c_{Pt/Co} = 4.14 \text{ \AA}$. Thus the lattice parameters change with the same trend observed for Au, and thus magnetoelasticity cannot explain the change of magnetic anisotropy induced by Pt capping. In order to have deeper insights into the magnetism of this system, XMCD experiments were performed at the ID08 beamline of

¹<http://www.synchrotron-soleil.fr/Recherche/LignesLumiere/SAMBA>

the European Synchrotron Radiation Facility (ESRF) in Grenoble ². In particular the attention was focused on Co nanoislands (0.5 ML) covered with 2.5 ML of Pt (deposited in one single time). The hysteresis cycles were obtained by recording the intensity variation of the XMCD absorption signal at the Co L_3 ($2p_{3/2} \rightarrow 3d_{3/2}, 3d_{5/2}, 4s$) adsorption edge as a function of the applied field. The loops were measured at different temperature in the range $10 \div 150$ K and at two different angles of incidence: $\alpha = 0^\circ$ (normal to the surface) and $\alpha = 60^\circ$ (Fig. 5.5). If the cycles are measured along the surface normal direction at temperature lower than 50 K, the intensity of the applied field (5T) is not sufficient to saturate the sample magnetization and minor loops are observed. At higher temperatures saturation is attained, the coercivity fields ($H_C \simeq 2.5$ T at $T = 50$ K) decreases gradually and vanishes between 100 and 150 K. In this range of temperature the transition between ferromagnetism and superparamagnetism takes place, as observed in MOKE experiments. The squared shape of the loops indicates that the easy axis lies out-of-plane. The comparison with the loops obtained at 60° makes this conclusion more evident. In this case indeed the loops assume a sigmoidal shape and saturation is hardly achieved. Such an angular dependence is in agreement with the prediction of the Stoner-Wohlfarth model [Stoner and Wohlfarth, 1948], the hard axis lies thus in-plane. The experimental cycles are fitted with a two-state model including a distribution of magnetic anisotropy. The best fits are obtained if in average the island are composed in mean by $N = 720$ atoms, each one with a mean magnetic anisotropy $\bar{K} = 0.38$ meV/atom ($\sigma_K = 0.09$

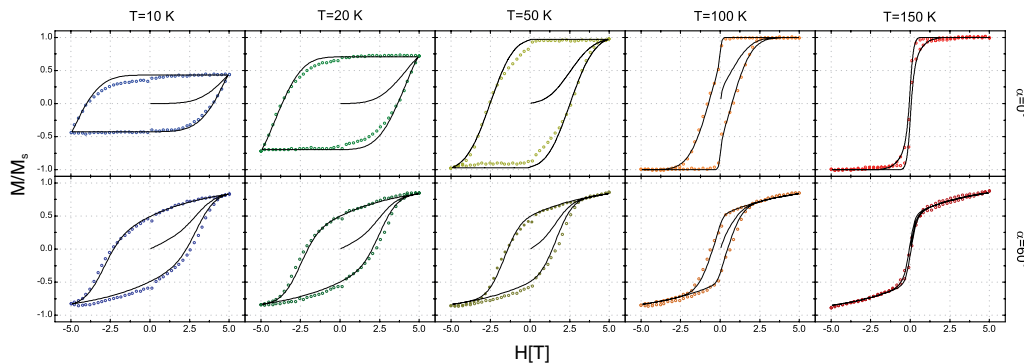


Figure 5.5: Experimental hysteresis loops (open circles) determined with XMCD at different temperatures T and angles α . The full lines correspond to a fit with the two-state model including a anisotropy distribution [Rohart et al., 2006].

²<http://www.esrf.eu/UsersAndScience/Experiments/ElectStructMagn/ID08>

Table 5.1: Effect of Pt capping on the magnetic anisotropy and on the spin and orbital momenta of Co.

	Co(0.5 ML)/Au(111)	Pt(2.5 ML)/Co(0.5 ML)/Au(111)
N [atoms]	700	720
\bar{K} [meV/atom]	0.33	0.38
\bar{E}_a [meV]	231	274
μ_L [μ_B /atom]	0.177	0.256
μ_S [μ_B /atom]	1.65	1.78
μ_L/μ_S	0.11	0.13

meV/atom). The same procedure was performed on Co nanoislands without Pt overlayer. In this case we get as a result that the islands are composed by $N = 700$ with a mean magnetic anisotropy $\bar{K} = 0.33$ meV/atom ($\sigma_K = 0.11$ meV/atom). As a consequence the activation energy for magnetization reversal \bar{E}_a changes from 231 meV to 274 meV. These results are in good agreement with MOKE measurements.

XMCD is also a technique capable to sense the local anisotropy of the angular (μ_S) and spin momentum (μ_L) around an atom that is excited by the absorption of X-rays. These quantities are obtained from magneto-optical sum rules and angle resolved measurements [Stöhr, 1999]. As can be seen, the spin momentum increases only slightly (within experimental uncertainty), passing from 1.65 to 1.78 μ_B /atom. On the other hand, an important increasing in the angular momentum is observed, which is raised from 0.177 to 0.256 μ_B /atom. All these results are summarized in Table 5.1

Eventually, these results together with the comparison with Au capping [Nahas et al., 2009] give rise to the following conclusions. Whereas the magneto-elastic part of magnetic anisotropy is almost similar in both cases (maybe slightly smaller for Pt/Co), the variation of magnetic anisotropy with capping is different considering the electronic hybridizations. Indeed from a microscopic point of view, Au hybridizes less with Co than Pt, leading to a very small induced magnetic moment [Šipr et al., 2007] (see Fig. 5.6). As a consequence, the direct influence of Au (through the spin-orbit coupling) on the magnetic anisotropy is lower than for Pt. We therefore mainly observe the variations of magneto-elastic anisotropy for Au capped Co islands and of interface anisotropy for Pt capped islands. It is worth noting that this picture is different from the one developed for ultrathin films, where Au and Pt were believed rather similar interface anisotropy due to hybridization effects.

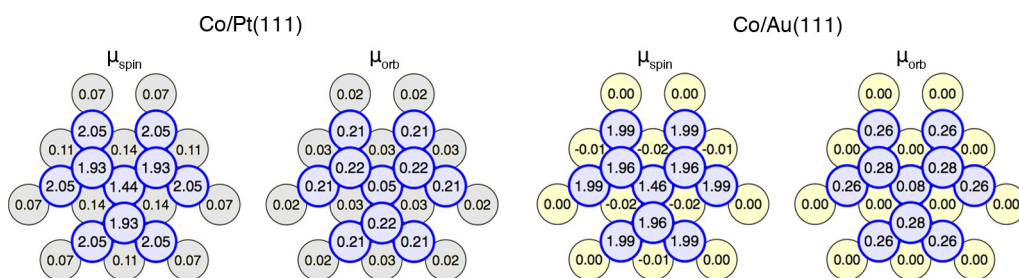


Figure 5.6: Local spin and orbital moment of Co atoms and of substrate atoms for bilayer of 10-atom clusters on Pt (left diagrams) and on Au (right diagrams) (figure extracted from [Šipr et al., 2007]).

5.2 Capping with molecules: thiols on Co

The idea to conjugate magnetism with the molecular world can bring new ways to control and manipulate spins in materials. One of the main opportunities offered by this route consists in using chemical bondings to tune magnetic anisotropy. In particular here we will analyze the impact of a molecular monolayer on the magnetic behavior of Co. Also, this study fits within the field of molecular spintronics, for which an understanding of the underlying physics requires to clarify the phenomena at the ferromagnet/molecule interface. Self-assembled monolayers (SAMs) and in particular *n*-alkanethiols (C_nSH , where *n* indicates the number of carbon atoms in the aliphatic chain) constitute a model systems for both these purposes because are simple, reactive molecules which easily form crystalline monomolecular films. Moreover, in a longer term view, they offer the possibility to play with their backbone in order to engineer the organic/inorganic interface, optimizing the performance of the devices. The present study was possible only by evaporating the molecules directly in UHV, maintaining high levels of cleanliness and avoiding the possible oxidation of the Co layer.

5.2.1 STM study of thiols growth

In the structural characterization of SAMs STM studies have gradually gained a privileged place since they allow real-space imaging down to molecular resolution and permit to observe non periodic structures, notably defects [Poirier, 1997a]. An understanding of the molecular packing of SAMs is important for the interpretation of fundamental studies and for the development of practical applications.

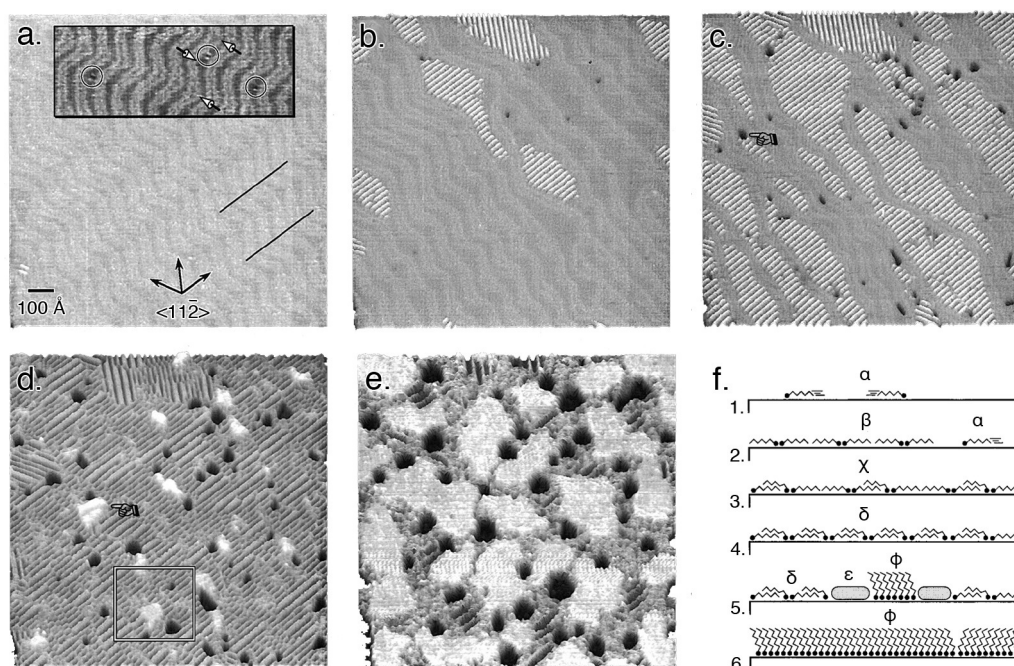


Figure 5.7: a-e. STM images for increasing exposures of hexanethiol C_6SH on Au(111) (figures extracted from [Poirier and Pylant, 1996]. a. Clean Au(111) surface; b. striped phase islands; c. striped phase growth with Au vacancy islands; d. nucleation of standing-up phase; e. growth of standing-up phase at expense of the striped one. f. Schematic representation of phases succeeding during decanethiol $C_{10}SH$ growth (figure extracted from [Poirier, 1999]).

5.2.1.1 Alkanethiols on Au(111)

Alkanethiols self-assemble on several metal surfaces, however they are grown mainly on gold. The first reason is because historically this system is the most studied one. However there are other characteristics that make gold a good choice as substrate. The main advantage consists in the fact that Au (unlike Ag and Cu, for example) can be handled in air without the formation of an oxide surface layer and can survive harsh chemical treatments which remove contaminants. The smoothness of the metal surface dictates the structure of the monolayer, especially the defect density. For the most highly ordered crystalline SAMs, an atomically smooth substrate, i.e. a single crystal surface, is required.

Self-assembly from solution is the traditional route for the preparation of SAMs, however the study of the growth from the gas phase in UHV offers the best chances for a detailed understanding of the self-assemble process [Schreiber,

2000], since it allows a precise cleanliness of the substrate and the use of a wide range of high-resolution vacuum techniques. In UHV STM studies provided a detailed molecular picture of the assembly mechanism (as shown in Fig. 5.7a-e) [Poirier and Pylant, 1996] which was later confirmed also by other diffraction techniques [Schreiber et al., 1998]. These analysis revealed that the growth of alkanethiols passes through different stages before reaching the full-monolayer. For this purpose, the most studied molecule was decanethiol $C_{10}SH$, but the general trend is common for all alkanethiols. At very low coverages the assembly involves probably a precursor, a physisorbed and mobile thiol, and chemisorbed thiolates with non-crystalline geometry (following the nomenclature by Poirier we will call this phase α [Poirier, 1999]). By increasing the coverage alkanethiols exhibits a distinct ordered motif and the so-called striped phases are formed. The stripes are aligned with the substrate $\langle 11\bar{2} \rangle$ directions and exhibit a corrugation of 5 \AA period along the row. The interrow spacing, on the other hand, depends critically on the length of the aliphatic chain. In these structures the alkanethiols molecules lie flat on the surfaces, with the molecular axis parallel to the $\langle 1\bar{1}0 \rangle$ directions. The unit cell of this submonolayer packing structure can thus be written with the general formula $p \times \sqrt{3}$. The structure of the striped phases changes with the coverage. The simpler one (β phase), in which the aliphatic chains are not interdigitated, occurs at lower coverages. For $C_{12}SH$ (whose length is 15.3 \AA) the phase β is described by a $13 \times \sqrt{3}$ unit cell [Camillone III et al., 1996] ($3.75 \times 0.5 \text{ nm}^2$), as shown in Fig. 5.8a. When the coverage is increased the thiols can adopt other flat structures to reach a higher packing density. In the case of decanethiol two

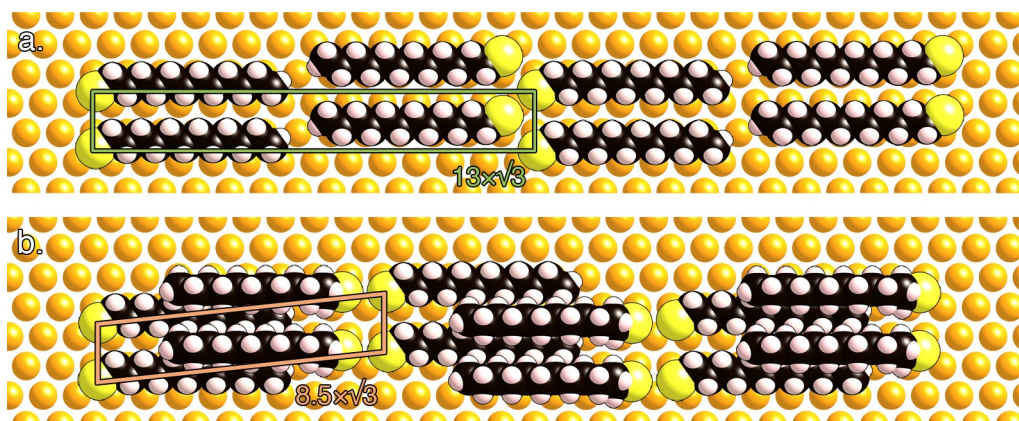


Figure 5.8: Proposed packing structures for the striped phases of dodecanethiol on Au(111), in analogy to the ones proposed for decanethiol [Poirier, 1999]. Top view of the β (a.) and δ (b.) phase models.

additional ordered flat phases were identified (γ and δ) where the chains interdigitate slightly out-of-plane [Poirier, 1999]. In the case of $C_{12}SH$ only the δ phase has been reported, with a unit cell of $8.5 \times \sqrt{3}$ [Pi et al., 2005] (inter-row spacing of 2.45 nm). The structure of this phase is sketched in Fig. 5.8b. If we further increase the thiol coverage the molecular order is disrupted. The molecular chains adopt different conformations and heights above the surface, this non-periodic and dynamic phase ϵ can be regarded as a two dimensional liquid. On Au(111) this structure is metastable so that, allowing the monolayer to relax, the chain orient upright adopting the full-coverage phase ϕ . This corresponds to the highest possible packing of the molecules: the surface is saturated and the monolayer is dense and solid-like. The hydrocarbon backbones adopt an all-trans configuration and are tilted of around 30° with respect to the surface normal. The central bonding habit of this phase is based on a $(\sqrt{3} \times \sqrt{3})R30^\circ$ overlayer [Chidsey and Loiacano, 1990; Widrig et al., 1991], the intermolecular distance is thus 0.5 nm. A more detailed analysis revealed that this phase adopts a secondary ordering of the chains corresponding to a

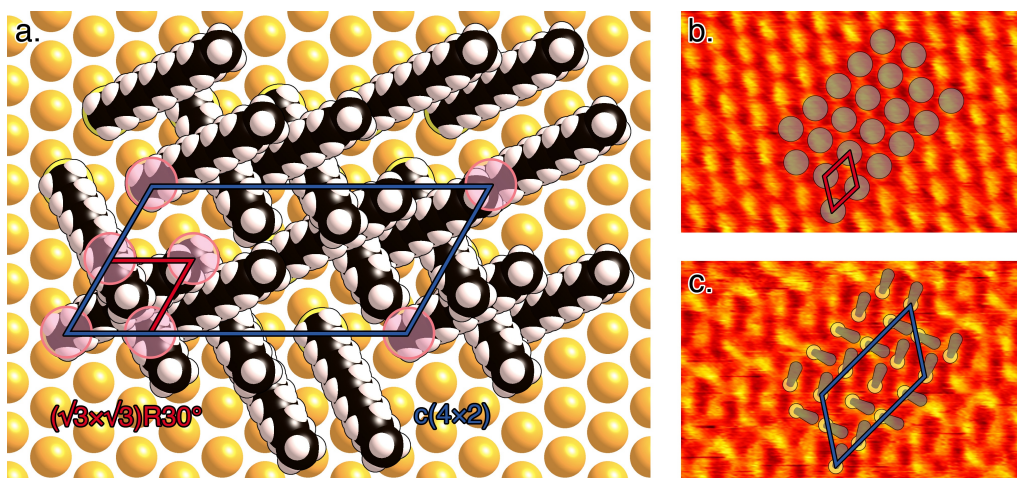


Figure 5.9: a. Structural model depicting the arrangement of dodecanethiols on Au(111) when maximum coverage of thiols is attained. The arrangement shown is a $\sqrt{3} \times \sqrt{3}R30^\circ$ (unit cell in red) where the sulfur atoms (sometimes highlighted with pink circles) are in the 3-fold hollows of Au lattice. The alternating orientation of the alkane chains defines a $c(4 \times 2)$ superlattice structures (unit cell in blue). b,c. Molecular-resolved STM image of the same area under different tunneling parameters: $U=+1.0$ V, $I=20$ pA (a) and $U=-1.0$ V, $I=20$ pA (b). To these images is superimposed a schematic representation of the $C_{12}SH$ molecules as shown in a.

$c(4 \times 2)$ superlattice of the $(\sqrt{3} \times \sqrt{3})R30^\circ$ hexagonal lattice [Nuzzo et al., 1990; Camillone III et al., 1993]. The primitive orthorhombic unit cell comprises four thiols arranged as two like-pairs with different orientations of the molecular backbone (twist angle around 90°). This structure is reported in Fig. 5.9, it is however to point out that some STM studies suggest polymorphism [Delamarche et al., 1994]. In molecular resolution STM images each protrusion is assigned to an individual alkanethiolate molecule. The observed contrast is chiefly due to the sulfur non-bonding electrons which enter in the conduction region. STM images thus show an hexagonal arrangement typical of the $(\sqrt{3} \times \sqrt{3})R30^\circ$ structure, like in Fig. 5.9b. If the imaging conditions are changed different patterns appear: it is not clear if this is due to a dynamic behavior of the monolayer induced by the tip $(\sqrt{3} \times \sqrt{3})R30^\circ \rightleftharpoons c(4 \times 2)$ [Terán Arce et al., 1998] or if the alkyl chains play a role in the STM imaging under certain tunneling conditions [Wang et al., 2001]. In some cases the motif of the $c(4 \times 2)$ superstructures can be clearly observed, as shown in Fig. 5.9c.

In Fig. 5.10a a large-area STM image of a Au(111) surface is shown, where dodecanethiols were deposited from evaporation directly in UHV, as described in Sec. 3.1.3. Even if the coverage of thiols is not sufficient to reach full saturation, it is possible to observe very large (typically $\sim 10^4 \text{ nm}^2$ wide) islands of dodecanethiols standing upright on the Au surface (apparent height $\sim 2 \text{ \AA}$). Fig. 5.10b shows a molecular resolution image taken in one of these islands. As can be seen, thiols are well-crystallized over relatively large scales (more than $100 \times 100 \text{ nm}^2$). Only few molecular defects in the alkanethiols lattice are present in the form of both vacancies and dislocations [Schönenberger et al., 1995]. At larger scale also pit-like defects are visible, whose depth corresponds

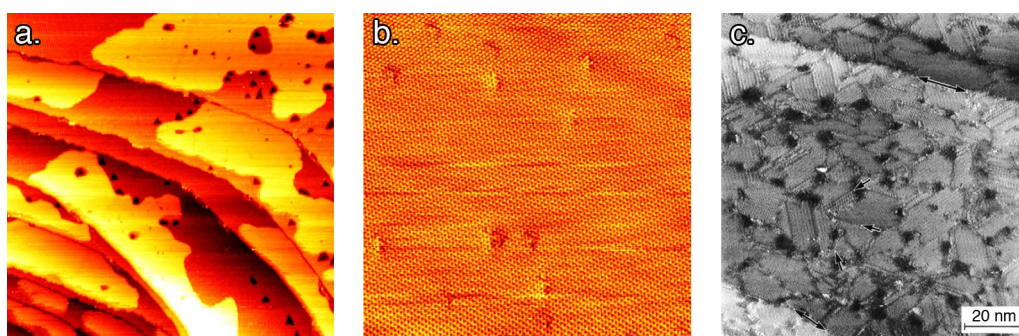


Figure 5.10: a. Large-area STM image ($500 \times 500 \text{ nm}^2$) of Au(111) surface where C_{12}SH were deposited from vapor phase in UHV. b. Molecular-resolution STM image ($45 \times 45 \text{ nm}^2$) taken on islands of C_{12}SH standing upright. c. Typical STM image of a solution-grown SAM of dodecanethiol on Au(111) [Delamarche et al., 1994].

a Au(111) single-atom step height, indicating that are Au vacancy islands. If the SAM is formed by immersion in solution, the presence of these islands is explained with chemical etching where Au atoms are dissolved by the solvent [Edinger et al., 1993]. The formation of these defects also in UHV has been explained assuming a shrinkage of the surface lattice upon thiol adsorption [McDermott et al., 1995] or by ejection of excess Au atoms from the surface during the relaxation of Au(111) reconstruction [Poirier, 1997b]. The density of Au vacancy islands in the present case is very low with respect to what observed in the case of C₆SH (see for example Fig. 5.7e). The dependency from the molecular components of SAMs contrasts with hypothesis that the topmost layer of Au surface is the principal responsible for the formation of vacancy. As a consequence, we speculate that during the assembly process the alkyl chains induce a certain mobility in some Au atoms of the topmost layer, in the attempt to adopt a stable molecular packing. This displacement leaves Au vacancy islands on the surface. Finally, we cannot exclude the eventual detachment of one or more Au atoms, etched away with the thiols if these re-evaporate from the surface during growth.

As a comparison, an STM image of a SAM of C₁₂SH prepared by immersion in an ethanolic solution and annealed at 50 °C is reported in Fig. 5.10c as a typical example taken from the literature [Delamarche et al., 1994]. It is clear that the density of defects is significantly higher if thiols are adsorbed from solution, with respect to the grown in UHV, the difference of grain boundaries density being the most significative. The improved crystalline quality of the monolayer grown with the present method is important in view of many possible SAM applications, like electronics or spintronics. In fact, a metallization of the thiol SAMs is often needed to build different types of devices. Defects enable the diffusion of metal adatoms, thus connecting the deposited metal layer with the substrate and leading to inefficient systems.

5.2.1.2 Alkanethiols on Co(0001)

Literature reports for SAMs on Co surface are extremely limited. The main reason is probably the reactivity of this metal, which readily oxidizes to form a passivation layer that inhibits the formation of sulfur-metal linkages. However, the few available reports in the literature suggest that thiolated molecules can bind to this substrate [Caruso et al., 2004; Hoertz et al., 2008]. More importantly, by comparing photoemission spectra of the occupied states of an arylthiol (biphenyldimethyldithiol, schematically represented in Fig. 5.11a) adsorbed on Au and on polycrystalline Co, it was observed a shift of ~ 1.7 eV towards greater binding energy [Caruso et al., 2006], as shown in Fig. 5.11b. The shift was related to a stronger hybridization at the Co surface, leading to

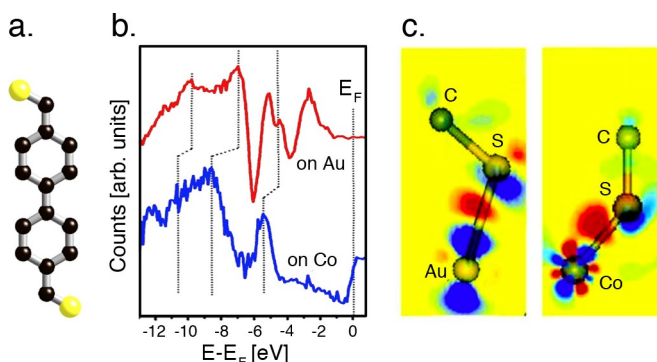


Figure 5.11: a. Ball and stick view of biphenyldimethyldithiol. b. Difference spectra between the clean substrate and vapor-adsorbed biphenyldimethyldithiol on Au and Co; the dotted lines trace out the common molecular orbitals. c. Calculated difference densities $\Delta\rho = \rho(\text{CH}_3\text{S}/\text{substrate}) - \rho(\text{substrate}) - \rho(\text{CH}_3\text{S})$ for the optimized bonding site and S to C orientation on Au and Co substrates (figures b and c extracted from [Caruso et al., 2006]).

the important conclusion that thiols are more strongly bound to cobalt than to gold. First-principles calculations for the simpler molecule of methanethiol (CH_3SH) on $\text{Co}(0001)$ qualitatively support this finding. In fact, the adsorption energy is found to be much higher for Co (3 eV) than Au (0.5 eV). The calculated charge redistribution at the interface (Fig. 5.11c) shows a more extensive hybridization in the case of Co (donation of $0.22 e^-$ to each S atom) compared to Au ($0.09 e^-$). Other theoretical calculations predicted the structure adopted by methanethiol on $\text{Co}(0001)$. The most stable configurations turned out to be the $\sqrt{3} \times \sqrt{3}R30^\circ$ superstructure [Wang et al., 2004], exactly like on $\text{Au}(111)$ surface, despite the considerable change in the hexagonal lattice parameters (assuming bulk values: $a_{\text{Co}} = 2.51 \text{ \AA}$, $a_{\text{Au}} = 2.89 \text{ \AA}$). To our knowledge no other reports investigate the growth and structure of thiols on Co.

The possibility to evaporate molecules directly in UHV permitted us to conduct a STM study about the growth of dodecanethiols on Co thin films of various thickness (up to 10 ML) deposited on $\text{Au}(111)$. In Fig. 5.12 the case of a 4.4 ML thick film, upon which C_{12}SH is deposited is shown. The coverage of thiols is increased by increasing the deposition time, even if with the technique employed here it is not possible to exercise any precise control over the deposition rate. In the present case the dodecanethiols are deposited by heating a freshly dipped filament with a current of 0.3 A for 8 min. In a first stage, the adsorption of C_{12}SH slightly modifies the morphology of the film. The main new

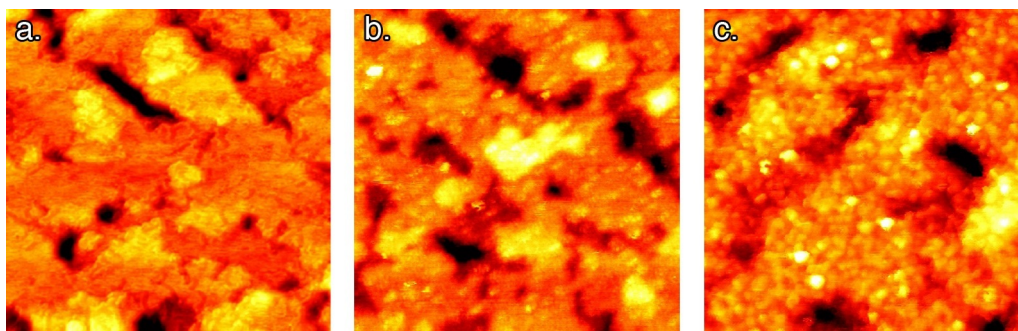


Figure 5.12: STM images ($50 \times 50 \text{ nm}^2$) showing the change in morphology of a 4.4 ML thick Co film due to dodecanethiol adsorption. a. Clean Co surface. b. After two depositions of dodecanethiols (in each one a freshly dipped filament is heated with a current of 0.3 A for 8 minutes). c. After six depositions.

feature is the appearance of bright spots on the surface, each one probably due to a thiol molecule covalently bound (Fig. 5.12b). After several deposition a clear change of the Co morphology is observed (Fig. 5.12c). Globular protrusions of different sizes and heights are now present on the surface, whose dimensions are not compatible with molecular features. We rather think that in the attempt to adopt a more favorable molecular packing, alkanethiols displace Co atoms on the surface. This induces a restructuring of the topmost layers and in particular to a roughening of the surface. This phenomenon could be analogous to what hypothesized on Au(111); the effect here is more pronounced since Co surface is less flat and a greater number of undercoordinated atoms are susceptible to be displaced.

The intrinsic roughness of Co thin films on Au(111) is the principal difficulty to study the structure of the adsorbed thiols. This is a consequence of a non perfect crystalline arrangement of Co atoms, that imperatively conducts to disordered monolayers. Nonetheless in some cases it was possible to observe a well-defined arrangement of the molecules, despite the roughness of the underlying substrate. As an example, Fig. 5.13a shows a STM image where several C_{12}SH depositions were performed on a 1.4 ML thick film. Thiols molecules can be observed nearly everywhere on Co and the typical distance between them indicates that they are compacted in the upright phase (black arrows). Sometimes C_{12}SH molecules adopt an hexagonal ordered structure (white arrow). The distance between two adjacent molecules is $\sim 5.0 \text{ \AA}$, far from the expected value for the $\sqrt{3} \times \sqrt{3}R30^\circ$ structure (4.3 \AA). On the other hand, this is in perfect agreement with a 2×2 symmetry. It is

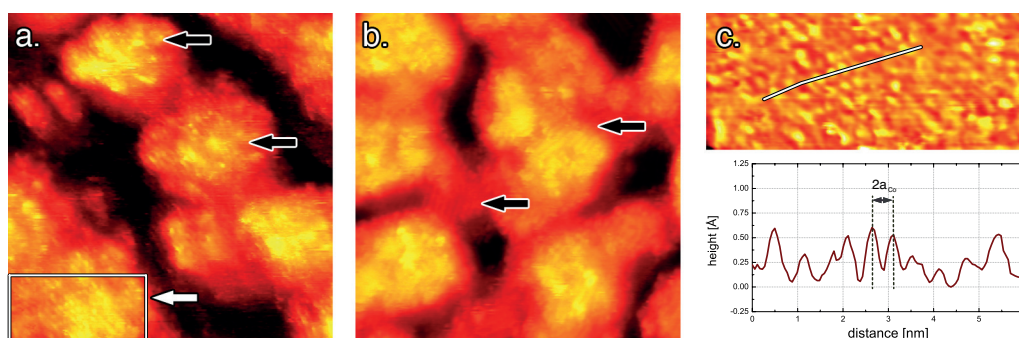


Figure 5.13: STM images ($25 \times 25 \text{ nm}^2$) where alkanethiols adsorbed on Co are visible, and indicated with black arrows. a. 1.4 ML Co thick film after six deposition of CH_{12}S . The white arrows indicates a region where an ordered arrangement of the molecules is observed. b. 2.5 ML Co thick film after one deposition of CH_{12}S . c. Zoom on the region marked in a. ($11 \times 5 \text{ nm}^2$) where the Co substrate was subtracted in order to enhance the thiol features and the corresponding section profile.

worth nothing that this packing preserves the molecular distance with respect to the structure adopted on Au(111) ($2 \cdot 2.51 \text{ \AA} \simeq \sqrt{3} \cdot 2.89 \text{ \AA} = 5.0 \text{ \AA}$). The 2×2 structure is slightly less favorable of the $\sqrt{3} \times \sqrt{3}R30^\circ$ one according to first principle calculations for methanethiol [Wang et al., 2004]. In the case of sulfur adsorption on Co(0001) the 2×2 superstructure has been experimentally observed with LEED [Lahtinen et al., 2005] and theoretically predicted to be the most stable [Ma et al., 2010]. During the first stages of growth there is evidence that alkanethiols lie flat on the surface like on Au(111). This is shown in Fig. 5.13b where black arrows indicate thiols lying down on a 2.5 ML thick film. The intermolecular distance is always 5.0 \AA . We are confident that the study of thiols adsorption on a flat Co substrate (like on a single crystal or on a layer-by-layer grown film) would permit to study in more details the structure of this system.

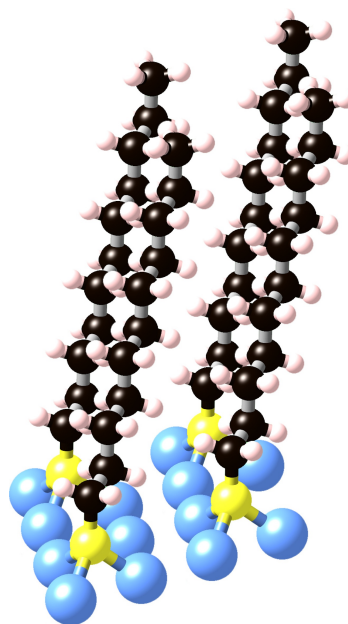


Figure 5.14: Ball and stick representation of CH_{12}S on Co(0001) in a 2×2 superstructure.

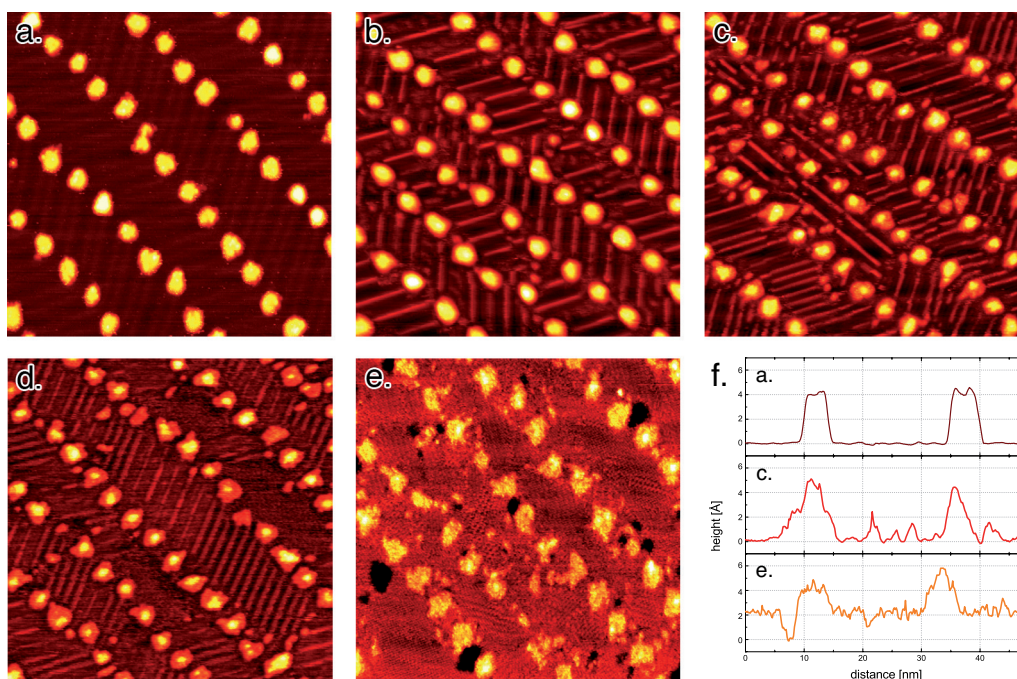


Figure 5.15: a-e. STM images ($75 \times 75 \text{ nm}^2$) of dodecanethiols adsorption on a submonolayer (0.24 ML) Co film. Before adsorption (a) and after one (b) two (c) four (d) and six (e) depositions. f. Typical profiles of Co nanoislands observed in different stage of thiols growth

5.2.1.3 Growth of thiols on and around Co nanoislands

The study of the growth of thiols on submonolayer Co thin films permits to follow the evolution of the growth by observing the succession of C_{12}SH different phases on the flat Au substrate. Fig. 5.15 reports STM images of 0.24 ML Co thin film upon which dodecanethiols are deposited. During the very first stage of growth the molecules are mobile on the substrate, but decorate the Co nanoislands and Au step edges remaining flat on the surface (5.16a). At low coverages the thiols begins to adopt ordered flat structures all above Au surface (5.15b). After the first deposition appear bright ridges due to sulfur atoms. These align in the $\langle 11\bar{2} \rangle$ directions, mainly parallel to the herringbone reconstruction. This is in contrast to what observed for the clean Au(111) surface where the sulfur alignment is parallel to the $[11\bar{2}]$ direction parallel to the elbows [Poirier and Pylant, 1996; Poirier et al., 2001]. The reason is probably due to the presence of the Co nanoislands that disturbs a parallel molecular packing. The distance between the sulfur ridges is 3.8 \AA , in good agreement with the calculated value for the $13 \times \sqrt{3}$ or β structure (3.75 \AA)

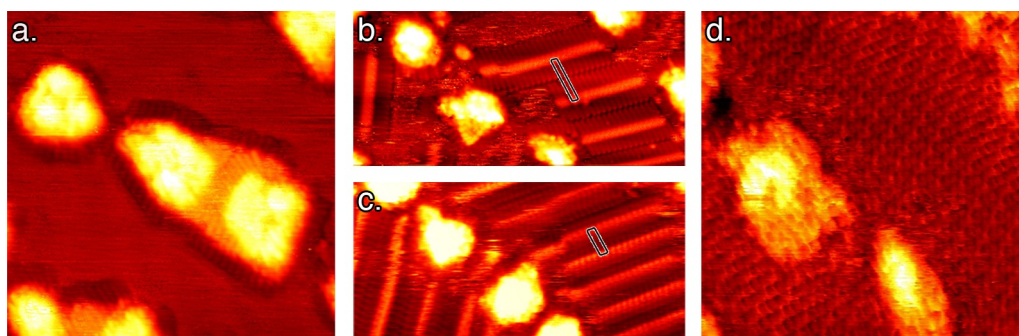


Figure 5.16: Molecular resolved STM images of dodecanethiols on and around Co nanoislands. a. CH_{12}S forms a molecular crown around the islands at very low coverage ($25 \times 25 \text{ nm}^2$). b,c. Striped β and δ phases between the islands ($30 \times 15 \text{ nm}^2$), with the respective unit cells highlighted. d. Compact and crystalline ϕ phase on the top and around Co nanoislands ($20 \times 20 \text{ nm}^2$).

[Camillone III et al., 1996]. Molecular resolved image (like the one reported in Fig. 5.16b) well show that thiols adopt a head-to-head disposition with non-interdigitated alkyl chains. By increasing the coverage, beside the β also the δ structure is adopted. The interdigitation of the chains permits to accommodate a higher density of molecules and the typical distance between S ridges is 2.5 \AA (Fig. 5.16c). If the coverage is increased again, these structures are perturbed and the principal observed phase is disordered and liquid-like (δ) (5.15c). At saturation, both the $(\sqrt{3} \times \sqrt{3})R30^\circ$ and the $c(4 \times 2)$ structures are visible (Fig. 5.16d). Thus on Au the growth of C_{12}SH follows the predicted progression. The presence of Co nanoislands disturbs the molecular packing, as becomes clear by the presence of a disordered phase all around the dots until saturation is reached. A schematic representation of the evolution of this phases with coverage is reported in Fig. 5.17.

It is interesting to observe how the evolution of the morphology of Co nanoislands changes with dodecanethiol coverage. At the beginning the size and the shape of the islands remain practically unchanged but, by increasing the

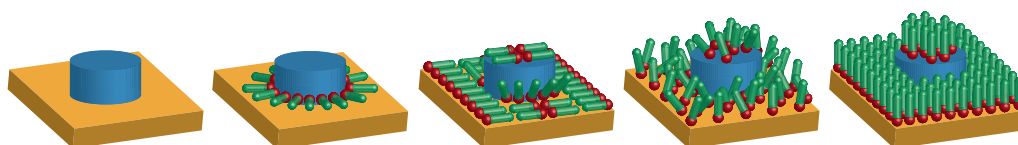


Figure 5.17: Schematic representation of the evolution of the SAM molecular structure around Co nanoislands with increasing thiols coverage

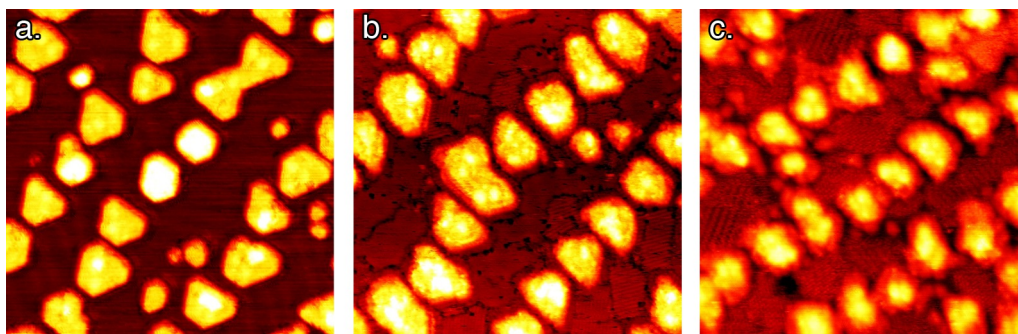


Figure 5.18: a-c. STM images ($50 \times 50 \text{ nm}^2$) of dodecanethiols adsorption on a submonolayer (0.51 ML) Co film. Before adsorption (a) and after one (b) and three (c) depositions.

number of depositions, a shell of Co monolayer becomes evident around the bilayer core of the islands. This is another confirmation of the ability of alkanethiols to restructure the surface by displacing atoms upon it. Co atoms are evidently more prone to be repositioned due to their peculiar under-coordination. As a result of this restructuring small Co monolayer islands appear out-of-site. The morphology of the islands drastically changes after the formation of the upright phase: most of the islands are now one monolayer high and their originally compact shape is lost (5.15e). The reason for this major change of the morphology is the substantial rearrangement of the chains to adopt the new compact structure. This confirms that the mobility of surface atoms is mainly due to the attempt of the thiols to adopt the more favorable packing inside the SAM. The STM images show that dodecanethiols are in the upright configurations also upon the Co nanoislands, as can be seen also from the profile height (5.15f).

If C_{12}SH is deposited on a larger submonolayer coverage, the bigger Co nanoislands disturb more markedly the molecular packing that hardly attains an ordered structure. For example, in the case of $\sim 0.5 \text{ ML}$ of Co we did not observe the formation of striped phases. Alternatively, we report a new structure, where the alkanethiols are always flat on the surfaces with the usual intermolecular distance of 5.0 \AA , but without forming ridges of aligned sulfur atoms. The ordered along the direction parallel to the alkyl chains is lost as a consequence of the limited available space. The upright crystalline phase is also heavily perturbed and disordered liquid phases are always present even if the coverage is close to saturation. The constant presence of this liquid phase probably moderates restructuring of the nanoislands, whose structure changes less significantly.

5.2.2 Effect of thiols on Co magnetic behavior

The physisorption of small gas molecules modifies significantly the behavior of ferromagnetic thin films and nanoparticles, as we seen in Sec. 2.3.2. The effect of chemisorbed molecules is expected to be even more substantial. In the present section we will study how the adsorption of dodecanethiols changes the magnetism of the underlying Co layer, in the form both of thin films and of nanoislands.

5.2.2.1 On the ferromagnetism of thin films

The influence of $C_{12}SH$ on the magnetism of cobalt nanostructures was studied as a function of film thickness. On Au(111) the magnetic properties of Co films change with the coverage θ_{Co} . As we have seen extensively, Co forms isolated islands with a superparamagnetic behavior. Above $\theta_{Co} = 1.5$ ML the nanoislands start to coalesce leading to a ferromagnetic thin film with perpendicular magnetization [Padovani et al., 1998]. By further increasing the Co coverage the ferromagnetic hysteresis loop becomes more square since an almost fully connected 2D net of islands is formed. Then at around 4 ML a spin reorientation transition (SRT) occurs: the dipolar interactions overcome the magnetic surface anisotropy and force the magnetization into the plane [Allenspach et al., 1990] for thicker films.

It is more convenient to study the effect of $C_{12}SH$ starting from the simplest case of a film well above the magnetic percolation. We thus consider the case of a 3.5 ML film, which exhibits well-saturated square hysteresis loop, with a coercive field H_c around 9 mT. Upon the first adsorption the hysteresis loop maintains its squared shape but H_c increases considerably reaching a value of ~ 17 mT. The same happens with the successive depositions: the coercive field gets the maximum value after the third deposition (25 mT) then it slightly decreases if further thiols are deposited. The evolution of the hysteresis loop with thiols deposition is reported in Fig. 5.19a. Kinetics effects due exclusively to the Co layer (like post-deposition mobility) are not responsible for the observed change of coercivity, since measurements have been repeated just before and after each deposition and without observing any modifications. It is difficult to draw an inference from these data, since coercivity is strongly real-structure dependent. Notably, imperfections of the film can cause localized nucleation for magnetization reversal, as well as traps capable to pin down the domain-wall motion. In the present case, the chemical modification of Co atoms due to the Co-S bonding can induce the formation of additional localized inhomogeneities. The increasing coercivity can thus be interpreted in terms of a more efficient domain-wall pinning. On the other hand, $C_{12}SH$

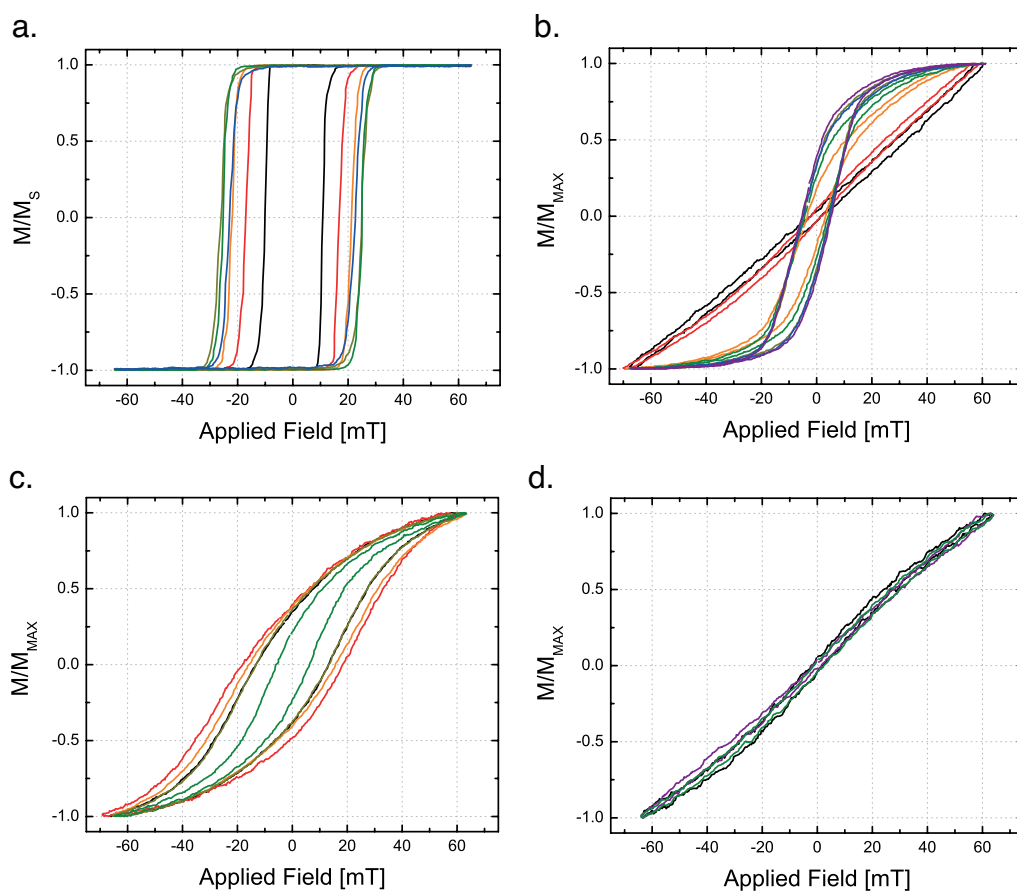


Figure 5.19: Evolution of hysteresis loops with the adsorption of CH_{12}S for Co films of different thickness: a. 3.5 ML b. 4.3 ML c. 1.8 ML d. 1.4 ML. In all cases the loops were normalized. The black lines represent the clean Co layers and the colored ones after one (red), two (orange), three (yellow), four (green), five (blue) and six (purple) CH_{12}S depositions.

adsorption can cause an increasing of Co magnetic anisotropy, which is the principal origin of coercivity.

To support the latter hypothesis C_{12}SH was deposited on a 4.3 ML thick film, just above the critical thickness for SRT. As can be seen in Fig. 5.19b, the curve in perpendicular geometry is an unsaturated loop, nearly closed. The linear dependence on field is a hard axis behavior, demonstrating that the easy axis of magnetization is parallel to the film plane [Pütter et al., 2001]. After the first thiol deposition the hysteresis loop remains essentially the same, but it changes clearly the shape after the successive adsorption. Even if saturation is not achieved, the cycle is now open ($H_c \approx 5$ mT) indicating that the easy axis

of the magnetization is shift back to the out-of-plane direction. It is tempting to ascribe this phenomenon to an increase of the out-of-plane magnetic anisotropy, strong enough to overcome again dipolar interactions.

The same experiment was performed on a 1.8 ML film. In this case the loop is unsaturated but clearly open with a $H_c \approx 13$ mT, as reported in Fig. 5.19c. The first deposition of thiols leads to an increasing of the coercivity ($H_c \approx 18$ mT) persuading us to reject the hypothesis of a dead-layer formation. Moreover, the successive thiol adsorption show that the underlying physics is rather subtle. Indeed, the coercivity decreases and ultimately becomes lower than the initial value. Such a trend can be temptatively explained with the simultaneous occurrence of two (or more) different phenomena with opposite effects. These seems to be counterbalanced when $C_{12}SH$ is deposited on a 1.4 ML film since no changes are observed in the magnetic response of the film, as shown in Fig. 5.19d.

The effect of thiols adsorption was investigated also on a thicker Co thin films, well after the spin reorientation transition and thus with a in-plane easy axis magnetization. $C_{12}SH$ was then deposited on a 10 ML film and the resulting hysteresis loops are shown in Fig. 5.20. Surprisingly, the cycle remains essentially unchanged and no apparent changes in the magnetic behavior are observed even after several depositions. At present we believe that the impact on magnetism is overcome by a larger volume contribution.

To estimate the change in magnetic anisotropy for films with perpendicular magnetization we considered previous measurements of Co thin films on Au(111) [Rodary et al.]. On the basis of the change of the measured coercivity

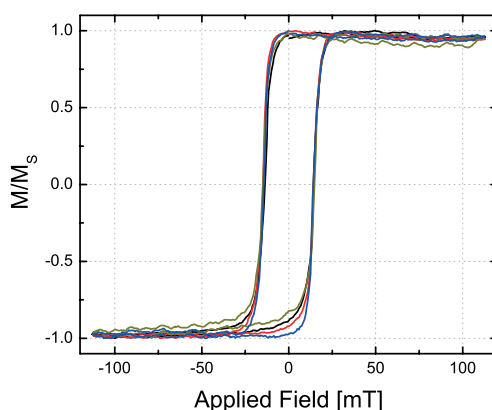


Figure 5.20: Evolution of planar (a) and perpendicular (b) hysteresis loops with the adsorption of $CH_{12}S$ for 10 ML thick Co film. The black line represents the clean Co layer and the colored ones after one (red), three (dark yellow) and five (blue) $CH_{12}S$ depositions.

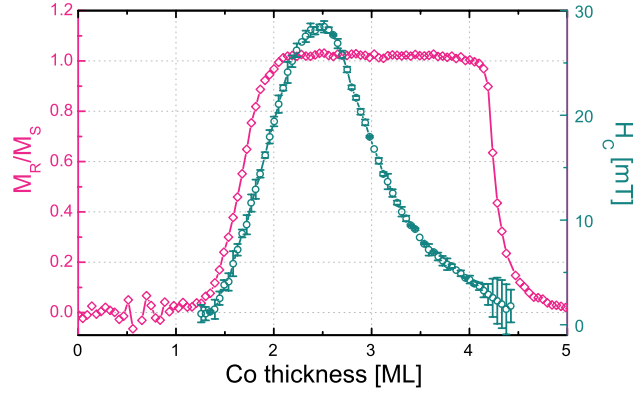


Figure 5.21: Thickness dependence of the coercivity field H_C (open diamonds) and of the ratio M_R/M_S (open circles) for Co thin films on Au(111) [Rodary et al.].

field as a function of the film thickness t shown in Fig. 5.21, to each sample was assigned an 'effective thickness' t_{eff} . That is, the thickness of the Co film was fictitiously altered to take into account the effect of thiol adsorption. Indeed, with this procedure it is possible to use the phenomenological relation between the effective anisotropy K_{eff} and thickness for ultrathin film:

$$K_{\text{eff}} = K_V + K_S/t \quad (5.1)$$

with the experimental found values $K_V = -622 \text{ kJ m}^{-3}$ and $K_S = 0.55 \text{ mJ m}^{-2}$ [Rodary et al., 2007]. This method is applicable only starting from $\sim 2.5 \text{ ML}$ since for thinner films the increasing of H_C is mainly due to an increasing of the magnetic percolation during the transition from zero-dimensional superparamagnetism to two-dimensional ferromagnetism [Padovani et al., 1999] rather than to a change in anisotropy. The results are shown in Fig. 5.22. The effective anisotropy is clearly increased for C_{12}SH adsorption both on 3.5 ML and on 4.3 ML thick films. However the trends are slightly different. Notably, the change in K_{eff} is pronounced since from the first deposition on the 3.5 ML film while it is not on 4.3 ML. The change of anisotropy in this last case does not seem to reach a kind of saturation, as in the other sample and as suggested from the hysteresis loops (Fig. 5.19b). This could be due to the procedure employed to calculate K_{eff} that is particularly delicate for small coercivity fields like these. At a first sight the change is more pronounced if thiols are deposited on a 3.5 ML film ($\Delta K_{\text{eff,max}} = 220 \text{ kJ m}^{-3}$) with respect to the adsorption on a 4.3 ML film ($\Delta K_{\text{eff,max}} = 77 \text{ kJ m}^{-3}$). These values should be taken with caution, due to the roughness of the method used for their determination. However, we are confident that this method provides a correct order of magnitude for

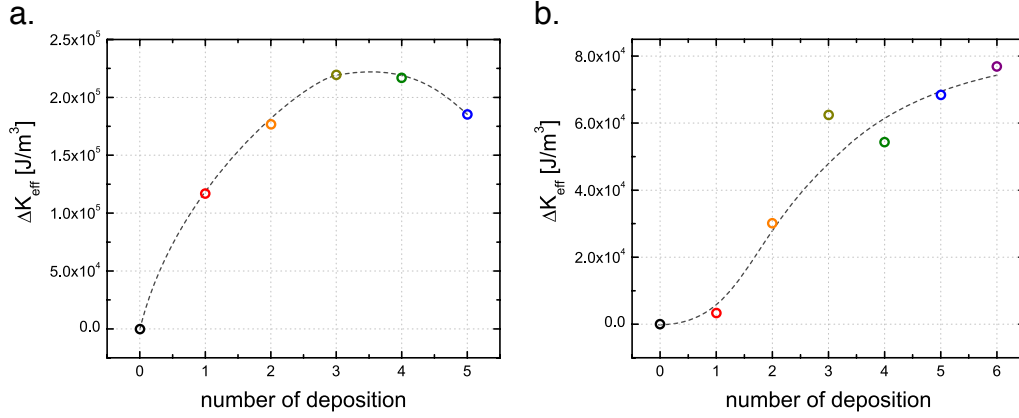


Figure 5.22: Evolution of the effective anisotropy K_{eff} with CH₁₂S depositions for a 3.5 ML thick (a) and 4.3 ML thick film (b). The dashed lines are drawn as a guide for the eye.

the change in magnetic anisotropy.

This brings us to the core issue: what are the physical phenomena causing a change in the magnetic anisotropy? The first one is the structural restructuring caused by thiols, as observed by STM (Sec. 5.2.1.2). Such an effect is surely present, but it is not the principal one, since the change in K_{eff} is always more pronounced in the first stages of adsorption when the morphology of the Co layer is practically unaltered. On the other hand, major changes on the surface structure are visible after some depositions, when the magnetic behavior does not almost vary.

Lattice relaxation induced by physisorbed molecules was identified as the dominant contribution in the change of magnetic anisotropy for the system Ni/Cu(001) [Hong et al., 2004; Sander et al., 2004]. As a consequence, the important contribution of magnetoelastic anisotropy must be taken into account. To do this, we consider the difference of magnetoelastic energy density of a bulk crystal for the magnetization lying perpendicular and parallel to the c axis [Sander, 2004]:

$$\Delta E_{\text{me}} = E_{\text{me},\parallel} - E_{\text{me},\perp} = (B_1 + 2B_3)\varepsilon_{xx} + B_2\varepsilon_{zz} \quad (5.2)$$

where the bulk magnetoelastic coupling coefficients are $B_1 = -8.1 \text{ MJm}^{-3}$, $B_3 = 28.2 \text{ MJm}^{-3}$ and $B_2 = -29 \text{ MJm}^{-3}$. The problem is now shifted to determining the values of strain coefficients ε_{xx} and ε_{zz} . The lack of structural data obliges us to search in the literature for values of similar systems, reported here in Table 5.2. The closest system is methanethiol on Co(0001) for which the adsorbed structures was calculated with density-functional theory calculations [Wang et al., 2004, 2005]. If the S is located in fcc or hcp

hollow sites (with $\sqrt{3} \times \sqrt{3}R30^\circ$ superstructure) the topmost layer of Co dilates while the underlying layer contracts with respect to the clean surface. Other studies (also experimental) on S/Co(0001) show that the Co layer relax in the same qualitative manner. Unluckily no data about the in-plane strain are available, even if there is some evidence that the three Co atoms below the S-atoms move slightly away (few hundredths of Å) from the fcc-symmetry point [Lahtinen et al., 2005; Ma et al., 2009]. Thus, we will consider only the effect of the vertical relaxation, using the values calculated for methanethiol on Co(0001) in FCC sites [Wang et al., 2005], averaging the relaxations of the first three interlayer distances to obtain $\varepsilon_{zz} = 0.013$. By substituting in Eq. 5.2 we get $\Delta E_{me} \simeq -380 \text{ kJ m}^{-3}$. The thiol-induced dilatation would thus cause a decrease in the out-of-plane anisotropy and cannot explain the observed enhancement of magnetic anisotropy.

The real peculiarity of chemisorption is that the electronic structure of both the molecule and substrate are strongly perturbed, as an intrinsic consequence of the chemical bonding. The outcomes on magnetic properties have been only partially investigated in the first-principle calculations for $\text{CH}_3\text{SH}/\text{Co}(0001)$ [Wang et al., 2004, 2005; Caruso et al., 2006]. The adsorption mainly affects the topmost atomic Co layer, as can be seen by comparing the density of states for different layers shown in Fig. 5.23 for the clean and covered surfaces. In the top atomic layer the d band width is smaller than for the underlying layer due to the reduced coordination. After the thiol adsorption this band becomes wider. The minority d band is only partially occupied so that the number of electrons depends on the band width. The widening of the d band, according to Bruno's model (Eq. 2.3), should provoke a decrease of surface magnetic anisotropy. Another consequence of the widening is a change in the atomic magnetic moment. In particular there are two different types of Co atoms:

Table 5.2: Interlayer distances d_{ij} for the clean Co(0001) surface and relaxations induced by methanethiol and sulfur adsorption. The distances are given in Å while the relaxations in percentage by $\Delta d_{ij} = (d_{ij}^{\text{ads}} - d_{ij}^{\text{clean}})/d_{ij}^{\text{clean}}$

reference	clean		fcc		hcp	
	d_{12}	d_{23}	Δd_{12}	Δd_{23}	Δd_{12}	Δd_{23}
CH ₃ SH/Co(0001)						
[Wang et al., 2005] - DFT	1.97	2.04	+1.4	-0.8	+1.1	-0.8
S/Co(0001)						
[Lahtinen et al., 2005] - LEED	1.99	2.06	+3.0	-1.4	-	-
[Lahtinen et al., 2005] - DFT	1.95	2.03	+1.5	-1.0	+0.5	-0.5
[Ma et al., 2008] - DFT	1.97	2.05	+0.8	-0.3	+1.2	-0.5

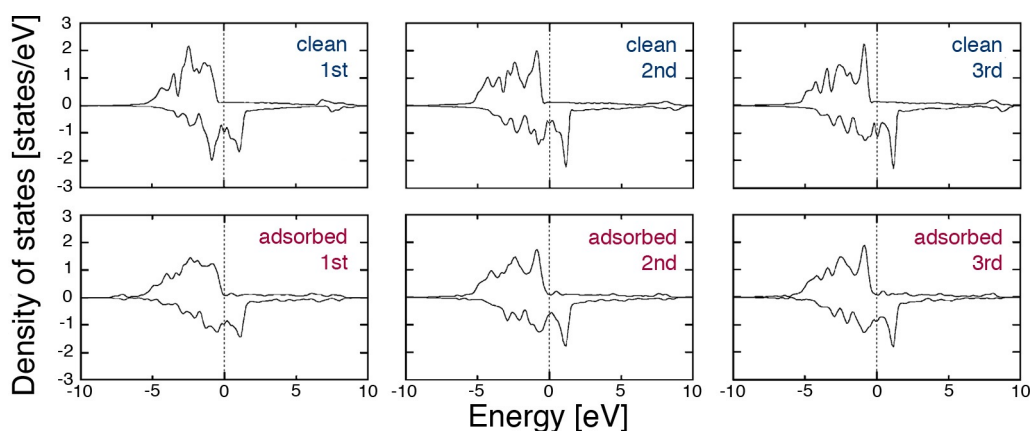


Figure 5.23: Layer-projected density of states for the clean and CH_3S adsorption surfaces, with the molecule in the fcc hollow sites and arranged in a $\sqrt{3} \times \sqrt{3}R30^\circ$ superstructure (Figure extracted from [Wang et al., 2005]).

the first one, directly bound to S, has a magnetic moment of about $1.66 \mu_B$, which is smaller than on clean-surface atoms ($1.76 \mu_B$); whereas the second one, unbound to S, have a larger magnetic moment of $1.85 \mu_B$). Moreover the exchange splitting of the 3d band induces, via the Co-S bonding, a small magnetic moment of $0.08 \mu_B$ at the sulfur atom. Thus Co-S is predicted not to quench magnetism, as indeed confirmed by our experimental results.

A point that must be taken in particular consideration is the formation of dipoles at the interface. In fact, it has been shown that an intense electric field can tune magnetic anisotropy [Maruyama et al., 2008]. Molecular dipoles are attracting alternatives, and the present case could be one of the first step towards this direction. Theoretical calculations showed that there is a donation of 0.22 electrons from cobalt to sulfur [Caruso et al., 2006]. This negative charge on S atoms certainly perturbs the crystal field at the surface, possibly increasing the out-of-plane anisotropy. All these studies testify how the impact of thiols on the Co magnetic behavior should be mainly connected to the induced change in the electronic structure. We thus believe that further discussions require first principle calculations. The understanding of this relation will permit not only to enlighten the presented results, but also to address molecular engineering of the magnetic anisotropy.

It has been demonstrated that molecular monolayers, and in particular alkanethiols, act as barriers against environmental agents, for example as protective layers against the oxidation of Cu [Laibinis and Whitesides, 1992]. Here we demonstrate that this protection from oxidation can preserve the magnetic properties of ferromagnetic ultrathin films in ambient conditions. To

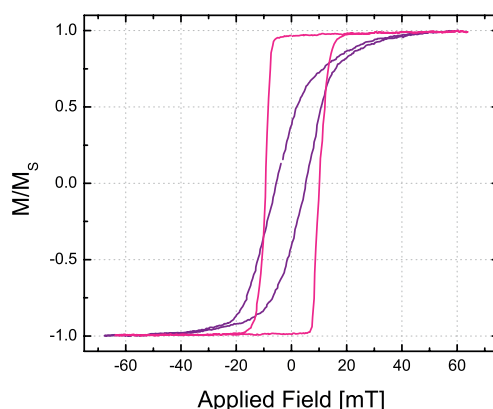


Figure 5.24: Evolution of the planar hysteresis loops of 4.4 ML thick Co film covered with a $C_{12}SH$ after exposure to environmental conditions. The purple and the pink line represent the magnetic response of the sample before and after the exposition to air, respectively.

do so, a 4.4 ML thick Co film covered with $C_{12}SH$ was exposed to air for 15 minutes and then its magnetic behavior was remeasured, as reported in Fig. 5.24. At the present moment it is not easy to find an explication for the change in shape of the hysteresis loops, which becomes more squared. Nonetheless, the relevant result here is that the magnetism survive after the exposure to air. In a successive experiments the time evolution of the loops of a 10 ML thick Co film covered with thiols was measured in environmental conditions. As in the previous case the change of the loops clearly changes but a magnetic response is measured even after 48 hours of exposure to air.

5.2.2.2 On the superparamagnetism of nanoislands

The study of the effect of dodecanethiol adsorption on submonolayer coverages of Co is a topic that must be treated separately. As we have seen in Sec. 4.2.1, cobalt forms single-domain islands whose magnetization reversal occurs via coherent rotation with respect to multi-domain thin films where the reversal proceeds with nucleation and propagation of domain walls. So, even if the physical phenomena influencing magnetism are probably the same, their impact could give rise to completely different effects since the system is completely different magnetically.

Dodecanethiols were deposited in successive steps on a 0.6 ML Co film and after each one the magnetic behavior was studied by measuring the thermal dependence of magnetic susceptibility. The evolution with the number of deposition is shown in Fig. 5.25a. As can be seen by increasing the thiol cov-

erage the transition from ferromagnetic to superparamagnetic behavior shift down towards lower temperatures. After the third one, a kind of saturation is observed and the curves are essentially superposed. The experimental curves were fitted in order to extract the energy of activation for magnetization reversal \bar{E}_a (Fig. 5.25b). This is reduced of about the 20% after the first deposition and of $\sim 40\%$ after the third one.

By coupling this measurements with STM images we can relate this trend with the molecular structure of the SAM. One of the most important features emerged from the STM study (Sec. 5.2.1.3) is that thiols can induce important modifications in the islands morphology. This issue complicates substantially the study of the magnetic effect, nonetheless some observations are worthy of remark. The transition from ferromagnetism to superparamagnetism is lowered the most after the first deposition when the islands morphology is nearly unchanged. Thus, as in the case of thin films, we can state that, even if the restructuring of islands surely affect the magnetic behavior, this effect is not the most important one. Moreover, from STM images we can say that the magnetism ceases to change even if the monolayer has not reached the compact structure typical of full coverage. Probably the Co nanoislands are already completely surrounded by molecules (and the magnetism fully changed) even before the formation of the crystalline SAM.

Overlooked the change of islands structure, we can affirm that the decrease of \bar{E}_a is connected to a lowering of magnetic anisotropy induced by CH_{12}S ad-

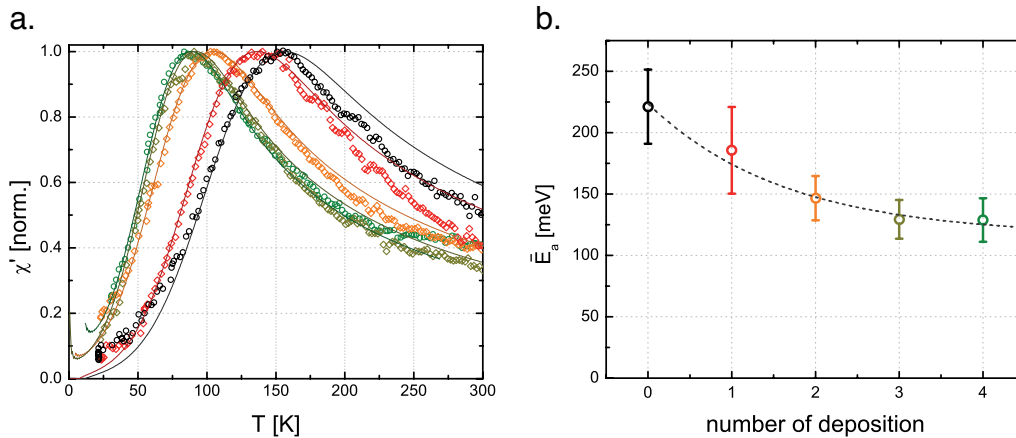


Figure 5.25: a. Evolution of the real part of the magnetic susceptibility of a 0.5 ML thick Co film with the number of C_{12}SH depositions. b. Energy of activation for magnetization reversal as a function of C_{12}SH depositions.

sorption. This is exactly the opposite trend with respect to the one observed for thin films. Nonetheless, we believe that the physical phenomena determining these changes are the same in both cases. If more mechanisms are simultaneously active their total balance on the magnetic anisotropy results in reverse effects, which could counterbalance when nanoislands coalesce, as observed in a 1.4 ML thick film. We are confident that a deeper comprehension of the impact of alkanethiols adsorption on the magnetism of Co thin films will permit to elucidate also the change observed for Co nanoislands.

5.3 Conclusions

Metallic and molecular overlayers dramatically influence the magnetic behavior of thin films and self-organized nanoislands, as widely shown in this chapter. The influence of a Pt overlayer on the magnetism of Co thin films is well known in the literature, but not in the case of Co nanoislands. The impact of a molecular overlayer is a new topic, and the originality of this case consists in the fact that the organic molecules are chemically bound to the magnetic element and self-organized in a compact layer. In both cases a detailed STM study of the growth of the overlayer is presented. The change in the magnetic properties of the nanostructures is discussed by presenting the physical phenomena that can compete to alter the original response. In order to elucidate the role of each contribution and to evaluate their interplay further investigations are actually in progress. This goal is fundamental to understand and engineer the anisotropy of magnetic nanostructures. In this perspective, the use of a molecular capping layer is particularly appealing since the unlimited possibilities offered by chemical synthesis can be exploited. As a further perspective, well-characterized SAMs can be used as barriers in magnetic tunnel junctions. A previous study showed that electrons can cross the barrier while remaining spin polarized [Petta et al., 2004], but their influence on the spin polarization must be clarified.

Molecular patterning with AFM

In the previous chapter we saw that when a SAM assembles above and around the nanoislands, the pattern defined by their arrangement is preserved. As a consequence, the ordered metallic self-assembly allows the selective grafting of the self-organized molecular layer at the nanometer scale. This property can be exploited to elaborate a mixed SAM where the two molecular components are regularly arranged in domains with a lateral size of few nanometers. To do so the metal array acts as a mask for the assembly of thiols, which form a crystalline layer on the Au surface all around the Co nanoislands. If this deposition is carried out by dipping the sample in a thiol solution, Co is readily oxidized when the sample is removed from UHV environment. Co oxide can be dissolved with an acid etching, locally revealing the bare Au areas. Inside this 'nanoholes' it is possible to selectively graft another kind of thiol. Schematic representations of the steps of this process are reported in Fig. 6.1, together with the corresponding STM images which demonstrate the feasibility of this route. The precise localization of the two molecular components can be combined with the design flexibility of SAMs allowing to fabricate molecular networks with well-defined properties and functionalities. The potentiality of this approach are being investigated in the frame of the SAMNET project, a collaboration between the STM team and the ITODYS laboratory¹, to which I contributed.

In this chapter we will show another way to pattern self assembled monolayers, where a scanning probe microscopy (and in particular AFM) is used

¹<http://www.itodys.univ-paris7.fr/>

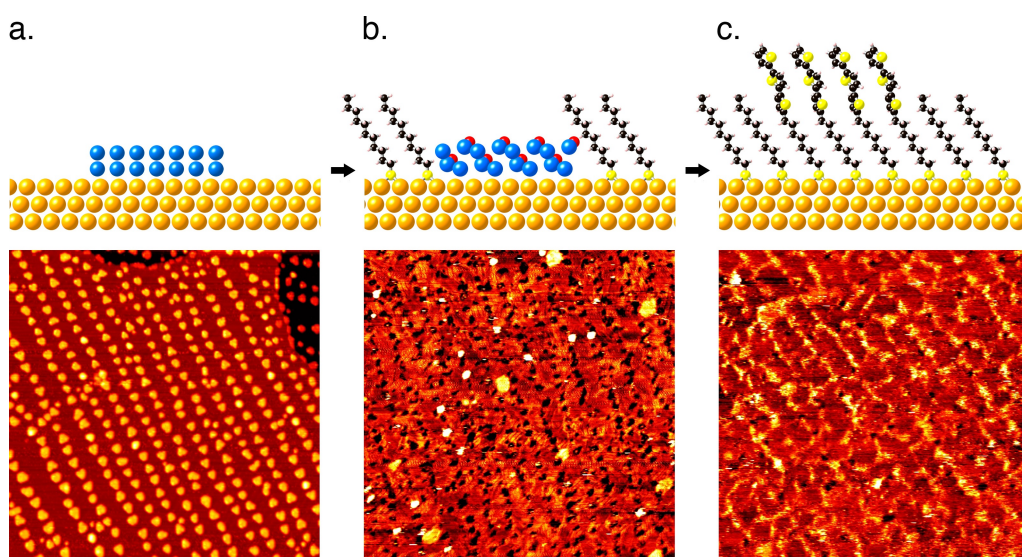


Figure 6.1: Schematic representation of the elaboration of a molecular network following the paths described in the text. In this case the two molecular components patterned are dodecanethiol and terthienyl-octanethiol. Below each representations, the corresponding STM images ($200 \times 200 \text{ nm}^2$) are shown.

not only for surface imaging, but also as active tool to manipulate matter at the nanoscale. The technique employed is called Dip-Pen Nanolithography (DPN) and its principles are described in the next section. When SAMs are formed on the surface their molecular dipoles align and influence the surface potential, whose change can be spatially mapped using Kelvin Probe Force Microscopy (KPFM). This technique is based on long-range interactions, so that a preliminary study about the contrast transfer in KPFM is presented. Finally, we combined static and dynamic force microscopy measurements for the imaging and characterization of SAM nanopatterns with the aim to obtaining detailed and reliable information about their morphology and structure.

6.1 Principles and procedures of Dip-Pen Nanolithography

The ability to obtain patterned surfaces has reached new frontiers since scanning probe microscopies have been used as active tools to manipulate matter with nanoscale precision. In particular DPN [Piner et al., 1999] is one of

the most promising lithography techniques, thanks to the high spatial resolution achievable, its parallelization capabilities and remarkable flexibility [Ginger et al., 2004; Salaita et al., 2006]. DPN involves the deposition of reactive species (inks) onto deliberate areas of the surface through the liquid meniscus formed between an ink-coated AFM tip and the substrate; here, the ink molecules chemisorb onto the surface to form compact SAMs, as shown in Fig. 6.2. Following different chemical approaches, DPN has been successfully employed to generate patterns using a wide variety of ink-substrate combinations, including biological molecules, polymers, metallic ions, and colloidal nanoparticles on metallic, semiconducting, and insulating substrates; as a result, the applications of DPN cover very different fields, ranging from medicine to electronics [Salaita et al., 2007]. Thanks to its potentials, efforts for new technological developments of DPN and of fundamental research to understand its underlying physics are active. In this latter field, most of the work is devoted to the comprehension and to the consequent developing of models describing the phenomena that enable the transfer of the ink molecules to the surface. Conversely, the study of the morphology, structure and related properties of SAMs deposited with DPN is only in its initial stage [Barsotti et al., 2004], due to the difficulty to characterize such small and sometimes damageable patterns. On the contrary, an in-depth study of the morphology and structure of DPN patterns is the basis for the possibility to control and finely tune the surface physical properties at the nanoscale.

As in the wider field of self-assembled monolayers, the most known case-study in DPN is represented by thiols chemisorbed on gold. Within the family of thiols, mercaptohexadecanoic acid (MHA, $\text{HS}-(\text{CH}_2)_{15}-\text{COOH}$) became

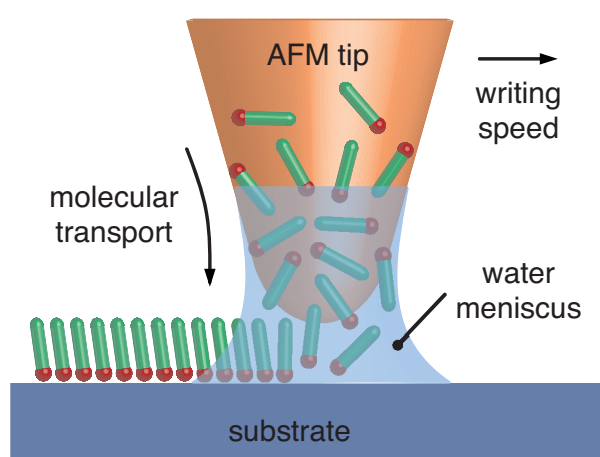


Figure 6.2: Schematic representation of Dip-Pen Nanolithography.

a prototype ink for DPN and the subject of many investigations, in particular examining the environmental condition effects on the writing process [Schwartz, 2002; Rozhok et al., 2003; Peterson et al., 2004], thanks to its propensity to form high-quality and stable SAMs. The interest around this molecule is also due to the possibility to exploit the reactivity of the carboxylate end group, envisaging the possibility to use MHA patterns as templates to build more complex structures. So far, this approach has been successfully employed with nanoparticles [Liu et al., 2002], nanotubes [Zou et al., 2007], DNA [Demers et al., 2001], and proteins [Lee et al., 2002]. SPM measurements were performed using silicon nitride probes (Veeco, ORC8, force constant 0.05 N/m) for DPN and contact mode imaging and metal coated silicon probes (Veeco, MESP, force constant 2 N/m, resonance frequency 75 kHz) for tapping mode imaging and electrostatic measurements. The instrument was enclosed in a home-made glove-box under a nitrogen atmosphere and the humidity was controlled by either feeding N₂ directly into the chamber or bubbling it through water. Relative humidity and temperature were monitored with a digital thermohygrometer. AFM tips were subjected to a 20 min cleaning with an UV/ozone treatment, then coated by dipping the cantilever three times for a few seconds in a 5 mM solution of MHA in ethanol (Sigma-Aldrich, NanoThinks ACID16). After each immersion the tips were blown dry with nitrogen and then used for patterning. All the depositions were carried out at a constant temperature of 27°C and a relative humidity of 55%. Ultra-flat polycrystalline gold surfaces (roughness: ~ 0.5 nm rms over an area of 100 m²) were prepared as described in the literature [Hegner et al., 1993]. Briefly, gold was evaporated on a freshly cleaved muscovite mica sheets. Then, small pieces of a Si(100) wafer were glued on the gold face using an epoxy glue. Finally, the mica was carefully stripped using a glaucoma knife or alternatively an adhesive tape.

6.2 Kelvin Probe characterization of nanopatterns

As for the characterization of the DPN patterns, among the available microscopic techniques, Lateral Force Microscopy (LFM) is usually chosen to visualize them, since it ensures high image contrast with short acquisition time. This technique measures the twist of the cantilever, which is determined by different friction areas on the sample. In particular, the areas patterned with MHA are characterized by a higher friction with respect to the surrounding clean Au surface, due to the presence of the polar terminal carboxy groups.

However, LFM it is intrinsically unsuitable to give reliable quantitative information due to the strong interaction with the surface, the difficulty to obtain absolute values of the lateral force and the difficulty to eventually relate such quantity with the physical properties of the nanodeposit.

Beyond the modification of the surface tribological properties, SAMs are also well-known to induce important changes in the substrate electronic properties. In particular, the alignment of molecular dipole moments on the surface induces a change in the surface potential. SAM of alkanethiols on gold can be considered as a dipole layer in which the total dipole moment arises from two internal dipoles stacked on top of each other. The first dipole $\mathbf{p}_{\text{Au-S}}$ is formed by the Au-S charge transfer interaction, while the second one \mathbf{p}_{SAM} is determined by the composition of the monolayer itself [de Boer et al., 2005]. These can be visualized as a double layer of two parallel charge sheets, separated by two dielectric layers with dielectric constants of $\epsilon_{\text{Au-S}}$ and ϵ_{SAM} . To simplify, the two dipoles are commonly substituted with an effective dipole \mathbf{p} , with only two parallel charge sheets characterized by a charge density $\pm\sigma$, as schematically represented in Fig. 6.3a. In this way, the change in the surface potential assumes the expression [Ashkenasy et al., 2002]:

$$\Delta V = n \left(\frac{p_{\text{SAM}} \cos \alpha}{\epsilon_0 \epsilon_{\text{SAM}}} + \frac{p_{\text{Au-S}}}{\epsilon_0 \epsilon_{\text{Au-S}}} \right) \simeq \frac{n p \cos \alpha}{\epsilon_0 \epsilon_r} \quad (6.1)$$

where n is the surface density of molecules, α the tilt angle of the molecular main axis relative to surface normal, ϵ_0 is the vacuum permittivity and ϵ_r is the relative dielectric constant of the the molecular film when is bounded to the surface. In the case of metals, this interface dipole influences the work

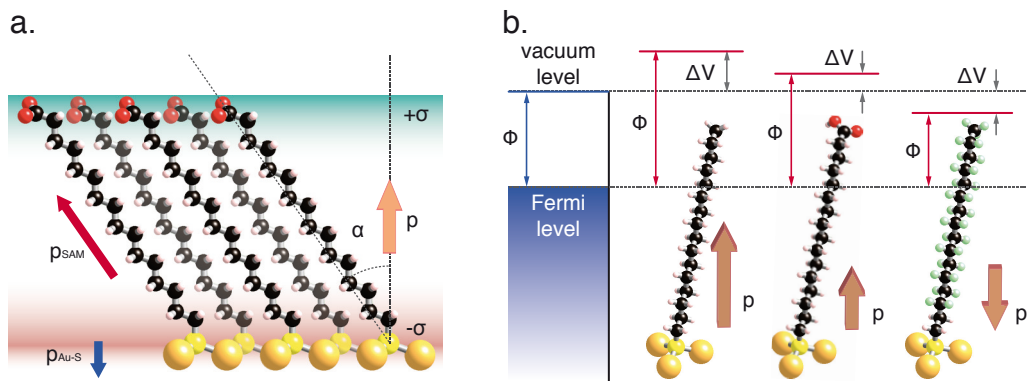


Figure 6.3: a. Schematic representation of how a SAM of alkanethiols on Au can be considered as a dipole layer arising by two internal dipoles. b. By changing the intensity and the orientation of this dipole the Au work function can be chemically tuned.

function, that can be thus chemically tuned [Campbell et al., 1996], as shown in Fig. 6.3b. This is a key phenomenon that would permit to control the band alignment when an interface is created between the metal and a semiconductor, with immediate implications on the performance of hybrid devices [de Boer et al., 2005]. Moreover the possibility to modulate the surface density of states through self-assembly offers new technologically relevant applications. [Didiot et al., 2007].

The local surface potential can be mapped by using KPFM, a technique that have been employed to characterize different ordered molecular architectures [Palermo et al., 2006], but only in one case DPN nanopatterns [Sinensky and Belcher, 2007]. As can be seen in Eq. 6.1, thanks to the impact of n and θ on the surface potential variation, Kelvin probe measurements are in principle able to give quantitative information on the SAM structure. Nonetheless, the KPFM characterization of nanopatterns is affected by serious problems of sensitivity and resolution, due to the long range nature of electrostatic interaction. Indeed, all the parts of an AFM probe (tip apex, pyramid and cantilever) bring local and non local contributions to the KPFM signal, resulting in a reduced lateral resolution. In the following, we exploited the ability to pattern surfaces with DPN forming nanodeposits of MHA with well-defined size and shape, to measure accurately the KPFM transfer function and consequently to evaluate the effective surface potential variation induced by the deposit. On this basis, we interpreted the measured surface potentials in terms of morphology and mechanical properties of the nanodeposits formed under different conditions, revealing the possibility to control the formation of three different phases.

6.3 Study of the transfer function of KPFM

Fig. 6.4 shows a pattern of 25 dots generated by leaving the tip at a fixed position in contact with the surface, for a dwell time that was gradually increased from 5 to 360 s. The ink molecules diffuse radially from the tip apex, thus forming a dot whose radius r depends on the dwell time t . The surface topography is shown in Fig. 6.4a, representing the height signal collected in tapping-mode AFM. This modality is particularly suitable for imaging soft or brittle samples (as in the present case), since the adhesion and frictional forces between the tip and the surface are suppressed. The topography image confirms that the molecules of MHA are standing upright on the surface, since the height of the monolayer is equal to $1.7 \pm 0.3 \text{ nm}$ (see cross-sectional profile below Fig. 6.4a), which is close to the length of a molecule in its all-trans conformation [Dannenberger et al., 1997], and remains constant throughout

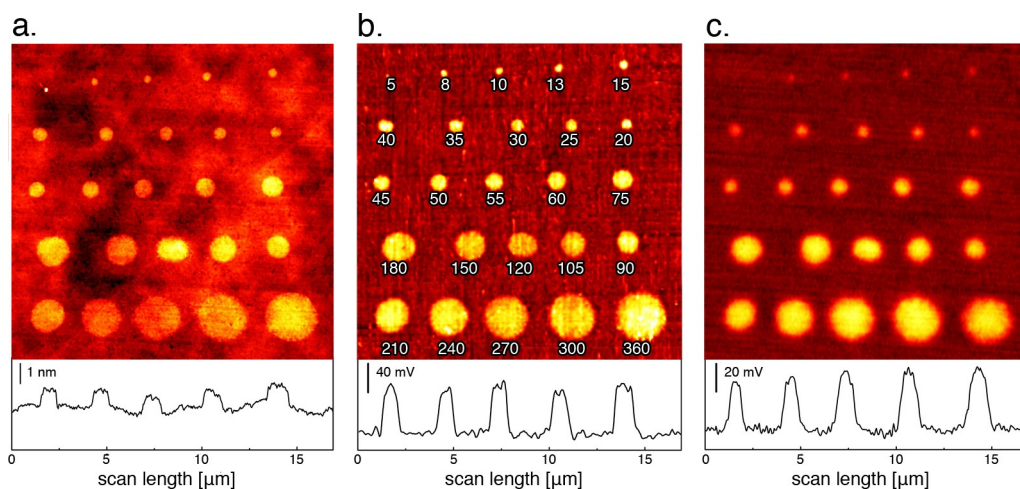


Figure 6.4: Height (a), lateral force (b) and surface potential (c) maps of a pattern of 25 dots for sequentially longer dwell time (reported in seconds in the central image). Below each image, a cross-sectional profile taken along a horizontal line passing through the central row of the pattern is shown.

the series of dots. This suggests that the structure of the monolayer is independent on t , and that the SAM continues to grow uniformly even when the dwell time becomes longer. As expected, the radius of the dots increases with the dwell time, in particular our results show that r increases with the square root of t , following a dependence predicted in a theoretical model for ink molecules flowing constantly from the tip, diffusing on the surface following a random walk, and finally assembling to form the monolayer [Jang et al., 2001]. The LFM image reported in Fig. 6.4b, collected with a clean tip, shows bright spots where the protruding hydrophilic carboxylic groups of the adsorbed MHA increase the friction of the tip with respect to the bare gold surface.

The ability to deposit patterns whose features have precise geometry and tunable size makes DPN patterns an ideal model system to study how the surface potential distribution contribute to the KPFM signal. The surface potential map of the pattern is reported in Figure 6.4c. First of all, it has to be pointed out that since the mapping of the surface potential was collected in the so-called 'lift mode', cross-talk between topographic and electrostatic signals is prevented: as a consequence, the visualization of the pattern is completely independent of the substrate morphology, thus resulting particularly clear. A further advantage of performing a KPFM characterization of DPN patterns is the reduced risk of damaging the SAM during the tapping mode operation.

The patterned areas show a brighter contrast, thus indicating that the alkanethiol monolayer chemisorption increases the surface potential or, equivalently, lowers the metal work function. Several studies have been carried out to provide a detailed explanation of this behavior, revealing that the change in the surface potential is mainly due to the dipole moment in the thiolate layer, while the dipole due to sulfur-gold bonds and charge transfer phenomena are negligible [Rusu and Brocks, 2006]. Thus, the dipole moment of MHA is oriented along the main axis of the molecule where the negative pole is on the sulfur side; the presence of the terminal carboxylic group contributes to reduce the SAM dipole moment with respect to a methyl-termination, even if it does not invert the orientation of the total dipole moment of the molecule, in agreement with one of the first KPFM study of alkanethiols on gold [Lü et al., 1999]. In this description, the KPFM contrast is assumed to originate at a molecular level, but the change in surface potential observed is a collective phenomenon resulting from the presence of the monolayer. Indeed, from an electrostatic point of view, the ensemble of dipoles in the monolayer can be approximated with two layers of opposite charge, a negative one close to the Au/SAM interface, and a positive one closer to the SAM/air interface.

Since the dots are uniform in height throughout their diameter (see Fig. 6.4a), we expect their electrostatic potential SP to be independent on the dot lateral size, however the surface potential increases from the dot periphery to the center due to the effect of long-range interactions in KPFM. Indeed, the difference $\Delta SP = SP - SP_{\text{sub}}$, where SP_{sub} is the surface potential of the substrate,

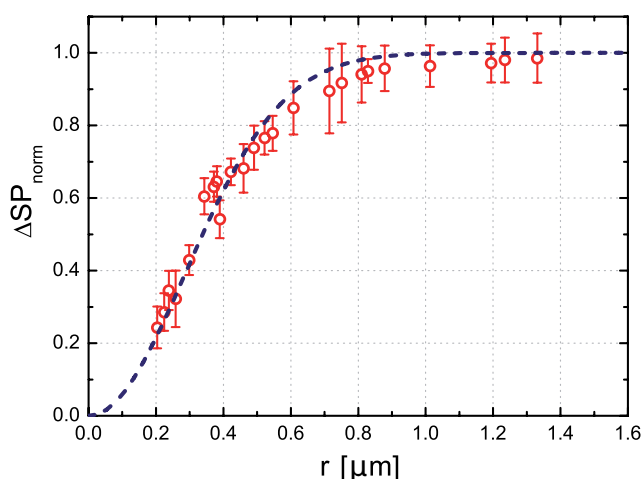


Figure 6.5: Dependence of the normalized value of surface potential at the center of the dots with the dot radius; the red line results from the fit of the data according to Eq. 6.2

depends on the distance d from the center of a dot and reaches a maximum in $d = 0$, since the non-local contributions of the signal from the bare substrate decrease the contact potential in the region where the tip is scanned over the deposit. In particular, when the size of the dot is too small, these non-local contributions are effective also at the dot center, thus influencing the measured value of ΔSP . In Fig. 6.5, the normalized surface potential at the dot center $\Delta SP_{\text{norm}} = \Delta SP / \Delta SP_{\infty}$, where ΔSP_{∞} is the surface potential for a dot of infinite radius, as a function of the dot radius is shown. These data represent how a circular area of radius r , centered under the AFM tip and characterized by a surface potential $SP = 1$, contributes to the total signal. From a different but equivalent point of view, these data describe how the contribution of the surrounding substrate ($SP_{\text{sub}} = 0$) reduce the potential of the patterned area, hence giving the experimental transfer function for our KPFM setup. Approximating the transfer function with a Gaussian-like function, our data can be fitted according to the following equation:

$$\Delta SP_{\text{norm}} = 1 - \exp\left(-\frac{r^2}{2\sigma^2}\right) \quad (6.2)$$

where the best fit value for σ is $0.287 \mu\text{m}$, the value $2\sigma = 0.574 \mu\text{m}$ is called effective width and gives an estimate of the diameter of the sample area electrostatically interacting with the AFM tip. Our data gives experimental assessment to the predictions of a theoretical study, where the contrast transfer in KPFM was calculated with numerical simulations on a series of tip-sample system by varying the tip geometries and dot diameters [Jacobs et al., 1998]. An analogous trend was also experimentally observed on island of different sizes of KBr on InSb [Krok et al., 2008] and of KCl on Au [Zerweck et al., 2005]; however, the availability of patterns with a well-defined geometry, as our pattern in Fig. 6.4, permits a more rigorous experimental study of the contrast transfer and more reliable support to the theoretical results, coming from patterns with the same circular geometry.

6.4 KPFM as diagnostic tool to study thiols structure

To understand the connection between the KPFM signal and the structure of the SAM, it is necessary to change the latter in a controlled fashion by tuning the deposition parameters. The simpler way to do this, is to deposit MHA lines while changing the tip speed v_{tip} during the process, allowing the molecules to adopt a well packed structure at low writing speed and a progressively flat

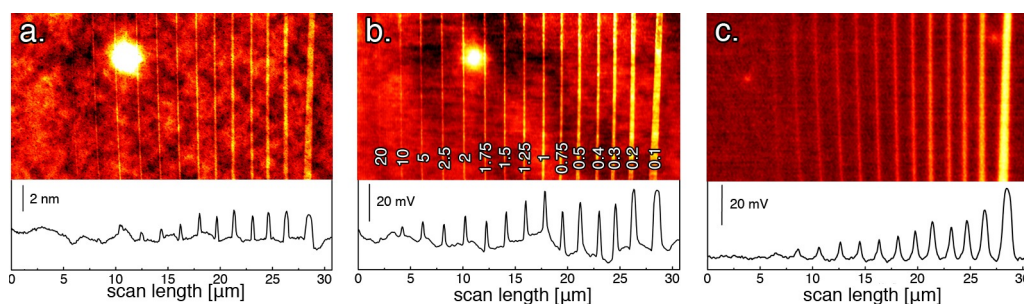


Figure 6.6: Height (a), lateral force (b) and surface potential (c) maps of a pattern of 15 lines written with gradually increasing tip speed. Tip speeds ($\mu\text{m/s}$) are indicated in the central image. Below each image, an averaged cross-sectional profile is reported.

lying conformation at high speed. Figure 6.6 shows a DPN pattern obtained varying the writing speed from 0.1 to $20 \mu\text{m/s}$. Again, the pattern is clearly visible both in height, friction, and potential images, even though it is important to emphasize some differences. As expected, LFM (Fig. 6.6b) is the technique displaying the highest sensitivity and all the 15 lines are well detectable, even when the writing speed is the highest. Conversely, the MHA pattern displays a height (Fig. 6.6a) below the instrumental sensitivity when the writing speed is higher than $5 \mu\text{m/s}$.

As shown in Fig. 6.7a, which reports the line height as a function of writing speed, at lower speed the molecules are standing upright: the measured height h of the lines is $2.0 \pm 0.3 \text{ nm}$, and it decreases exponentially by increasing v_{tip} down to $0.8 \pm 0.2 \text{ nm}$ for $v_{\text{tip}} = 5 \mu\text{m/s}$, then an abrupt change is observed in the interval $v_{\text{tip}} = 5 \div 10 \mu\text{m/s}$. The maximum height measured is in good accordance with a previously reported value calculated from XPS analysis (1.94 nm) that corresponds to a structure with molecules tilted by an angle of 32.5° to the surface normal [Dannenberger et al., 1997]. According to our measurements, the tilt angle increases with the writing speed starting from $30 \pm 7^\circ$ reaching values up to $70 \pm 3^\circ$ when $v_{\text{tip}} = 5 \mu\text{m/s}$. Obviously, the tip speed influences also the width w of the MHA lines: this decreases from $650 \pm 30 \text{ nm}$ when $v_{\text{tip}} = 0.1 \mu\text{m/s}$ to $70 \pm 10 \text{ nm}$ when $v_{\text{tip}} = 5 \mu\text{m/s}$. The dependence of w on inverse speed $1/v_{\text{tip}}$ is shown in Fig. 6.7b. Here, two different regions are clearly distinguishable, both of them showing a linear trend of w vs. $1/v_{\text{tip}}$, with two different slopes. This behavior was modeled taking into account the activation energy of the ink detachment from the tip [Weeks et al., 2002]. According to this model, the transfer process of ink molecules may follow two regimes, one dominated by surface kinetics at high tip speeds, and one controlled by diffusion at low tip speeds. The surface potential map

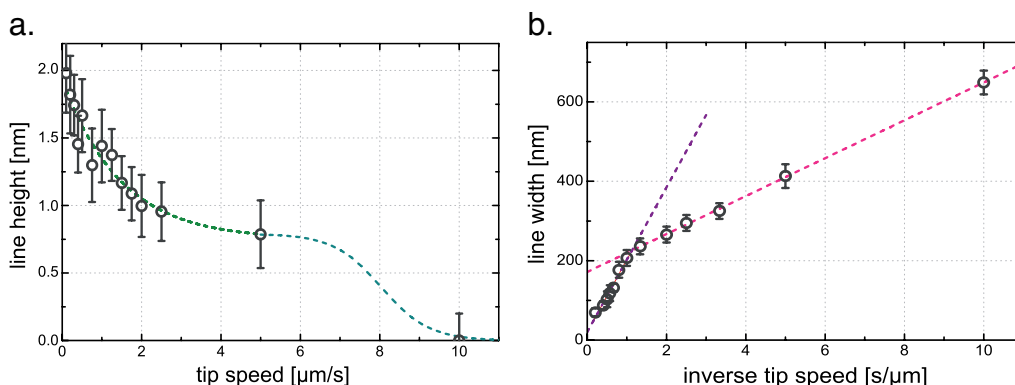


Figure 6.7: a. Height of MHA SAMs as a function of the writing speed and b. width of MHA lines as a function of inverse writing speed. The green line in panel a represents an exponential fit up to $v_{\text{tip}} = 5 \mu\text{m/s}$. In panel b, the two straight lines result from a linear regression of the experimental data.

is reported in Fig. 6.6c. Also in this case the morphology of the substrate does not affect the KPFM image, again collected in the lift mode, and the pattern appears particularly clear. Indeed, the sensitivity of the technique is quite low if compared with the one reached in LFM (Fig. 6.6b). As in the height image (Fig. 6.6a), the lines written at speeds higher than $5 \mu\text{m/s}$ are not visible: this could be explained first of all by remembering the intrinsic limitation of lateral resolution of KPFM (the topographical width of these lines extracted from LFM images is lower than 200 nm). Most importantly, under these conditions the MHA molecules are highly tilted with respect to the substrate, with a consequent reduction of the component of the dipole moment perpendicular to the surface, responsible for the KPFM signal. Finally, we can hypothesize that in these lines the monolayer is less closely packed and less ordered, and thus the number of MHA molecules that contribute to the change in surface potential is further decreased.

The lines detected in the KPFM image exhibit a maximum value of the surface potential that decreases exponentially with v_{tip} . This may result from two concomitant effects:

1. The decrease of the line width.
2. The variation of the molecular orientation in the SAM structure.

To analyze the two effects, we adopted a recent model that, in one dimensional systems, permits to quantify the potential broadening due to the effective width, to calculate the surface potential for each sharp nanostructure and

finally to simulate the surface potential map of the whole pattern [Liscio et al., 2008]. The simulation starts from the morphological information contained in height images by assigning an asymptotic potential value at each region of the surface, thus generating a stepped surface potential map that would be measured by a KPFM with infinite resolution. The broadening effect of the real measure is taken into account through a convolution of this intermediate image by simulating the edge profiles with the product of two Boltzmann functions:

$$y = 1 - SP_{\text{sub}} + \Delta SP_{\text{eff}} \frac{1}{1 + \exp\left(\frac{x - x_c - w/2}{\delta}\right)} \cdot \frac{1}{1 + \exp\left(\frac{-x + x_c - w/2}{\delta}\right)} \quad (6.3)$$

where $\Delta SP_{\text{eff}} = SP - SP_{\text{sub}}$ is the difference between the surface potential of the SAM and the one of the substrate (set as zero), x_c is the center of each line along its width (aligned to the x -axis) and w is the morphological width of the MHA lines, which can be measured from Fig. 6.6a. The shape parameter δ is related to the KPFM contrast transfer function through the formula $\delta = \sigma/2$, so that in our case $\delta = 0.144 \mu\text{m}$ (see Sec. 6.3). For each line the KPFM profile was fitted to extract the effective difference of the surface potential ΔSP_{eff} , i.e. the one unaffected from the reduced size of the patterns. The values extracted by

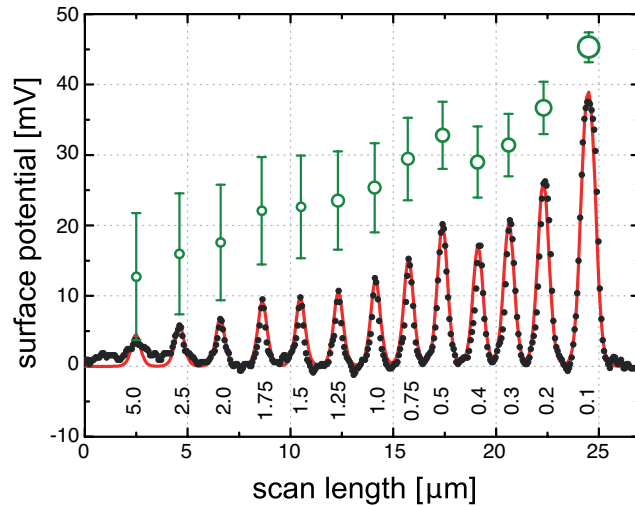


Figure 6.8: Measured (full dots) and fitted with Eq. 6.3 (red line) surface potential profile of the MHA lines reported in Fig. 6.6. The green open dots with error bars corresponds to the best fit values of ΔSP_{eff} ; that is, the surface potential that would be measured with a KPFM with infinite resolution. The diameter of each dot corresponds to the line morphological width.

fitting the experimental potential profile of each line with Eq. 6.3 are reported as green empty dots in Fig. 6.8, the fitted potential profile is also shown with a red line. As can be seen, the model perfectly follows the experimental data. In particular, here it is important to remark the good agreement obtained with the adopted value of δ and this supports the validity of the method we proposed in Sec. 6.3 to measure the transfer function.

With this procedure the effect of the size is taken into account, and KPFM measurements can be exploited to extract useful information about the SAM structure. The values of effective surface potential ΔSP_{eff} decreases noticeably as ν_{tip} increases, the reduction can thus be exclusively ascribed to the different packing of the MHA molecules as a consequence of the higher writing speed. In particular, as described by Eq. 6.1, this effect is due both to the tilt angle α and to the surface density n of the molecules in the SAMs. In principle, the first contribute could be taken into account from the height image (Fig. 6.6) since, starting from simple geometric considerations, for each line i :

$$\Delta SP_{\text{eff,tilt},i} = \Delta SP_0(\cos\alpha_i/\cos\alpha_0) = \Delta SP_0(h_i/h_0) \quad (6.4)$$

where the index 0 refers to the line written at the lowest writing speed. The three values of surface potential as measured, extracted from fitting procedure, and calculated taking into consideration the tilt angle of the molecules as function of the writing speed are listed in Table 6.1. As can be observed, the

Table 6.1: Description of measured size and corresponding surface potential of MHA lines deposited at different writing speeds.

$\nu_{\text{tip}} \mu\text{m/s}$	h [nm]	α [°]	w [nm]	ΔSP [mV]		
				measured	effective	calculated
0.1	2.0±0.3	30±7	650±30	39±3	45±2	
0.2	1.8±0.3	38±5	410±30	25±2	37±4	40±6
0.3	1.7±0.2	40±4	320±20	19±1	31±4	31±4
0.4	1.4±0.3	50±4	300±20	15±1	29±5	31±4
0.5	1.7±0.3	44±5	270±20	18±2	33±5	37±6
0.75	1.3±0.3	55±4	246±20	14±1	29±6	31±6
1.0	1.4±0.3	51±4	200±20	12±2	25±6	33±6
1.25	1.3±0.2	53±3	180±20	10±1	24±7	30±4
1.5	1.2±0.2	60±3	130±10	9±2	23±7	25±4
1.75	1.1±0.2	62±3	120±20	7±1	22±7	26±4
2.0	1.0±0.3	64±5	100±20	6±1	17±8	22±4
2.5	0.9±0.2	65±3	90±10	5±1	16±8	23±5
5.0	0.8±0.2	70±3	70±10	3±1	12±9	24±7

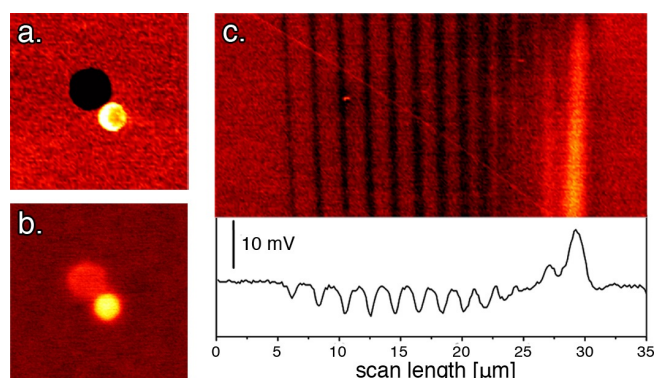
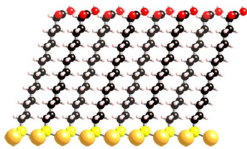
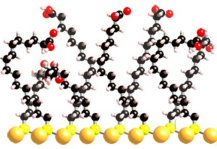
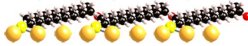


Figure 6.9: LFM (a) and KPFM (b) images of two dot features with molecules lying flat (upper left) or standing upright (lower right). c. Surface potential maps of a pattern of 13 lines written on an aged gold surface.

calculated value $\Delta SP_{\text{eff,tilt}}$ deviate significantly from ΔSP_{eff} when the writing speed is high ($\gtrsim 2 \mu\text{m/s}$), suggesting that in these cases n is particularly lowered and the molecules are less densely packed. This conclusion is fully consistent with the real situation at the surface: when α is increased, the binding sites on gold surface are less accessible, this in turn is supported by considering the limit case in which the molecules are lying flat on the surface in the striped phase, which can be studied only when the molecular coverage (and consequently n) is low, as seen in Sec. 5.2.1.1.

Previous studies claimed that patterns where the MHA molecules are in the striped phase show lower contrast with respect to the bare substrate in LFM images, since the surface exposes the methylene moieties composing the MHA backbone. A pattern which permits to observe this behavior is shown in Fig. 6.9a, where we deposited two adjacent dot features that show opposite contrast in the LFM image. The height image (not shown) taken in tapping mode confirms that the MHA molecules are standing upright only in the dot with higher friction, while in the other one the molecules are lying flat. As can be seen in the KPFM image in Fig. 6.9a, the surface potential is considerably reduced in the latter dot, due to the combined effect of increased and decreased in the striped phase, however the surface potential is still higher than that of the bare gold. In some other cases, when the substrate starts aging, we obtained SAMs with a bright contrast in LFM images but lower surface potential with respect to the substrate. An example of this is shown in Fig. 6.9c, where the pattern is similar to the one studied in Fig. 6.6. The SAM is successfully deposited, but after the first line the molecules are arranged in such a way that the total dipole moment of the molecules in the monolayer is inverted. Even

Table 6.2: Schematic representation of the structures that the molecules of MHA can adopt on the gold surface and the contrasts that these originate in height, friction and surface potential maps.

	upright	disordered	striped
			
AFM	bright	-	-
LFM	bright	bright	dark
KPFM	bright	dark	bright

if it is difficult to find an exhaustive explanation to this behavior, the MHA molecules are probably arranged in a disordered phase. In our case, the lack of order could be due to the inaccessibility of some binding sites due to the gold aging. On the basis of all these results, Table 6.2 summarizes how the combined use of tapping mode AFM, LFM and KPFM measurements permitted us to identify the different structures that MHA can adopt on the surface depending on the deposition conditions:

1. An ordered phase with tilted molecules provides bright contrast both in AFM and LFM and KPFM images. By changing the tip speed, the tilt angle of molecules can be varied from 30 to 70°, determining negative variations of the work function within a range of about 30 meV.
2. At very high tip speed, a striped phase with lying molecules is obtained, giving dark contrast in LFM images and bright contrast in KPFM images.
3. When aged substrates are employed a disordered phase is observed, giving bright contrast in LFM images and dark contrast in KPFM images. For this structure, the metal work function can be increased within a range of about 10 meV.

6.5 Conclusions

In this chapter we employed KPFM to characterize MHA patterns deposited with DPN, exploiting the change of gold work function induced by the formation of SAMs. The ability to obtain patterns with well-defined shape and size enabled us to experimentally measure the contrast transfer function. This

analysis permitted us to take into account the effect of the reduced size of the patterns, and to obtain quantitative information on the structure of the SAM, connecting it to the DPN writing conditions. Finally, when used in conjunction with other AFM techniques, KPFM can be a tool to identify three different structures that MHA can adopt on gold surface: a) an ordered phase with tilted molecules, b) a striped phase with lying molecules, and c) a disordered phase. Thanks to this structural tunability, the gold work function can be controllably changed within an interval of 50 meV.

This study demonstrates from the one hand the structure tunability of MHA SAMs and, to the other hand, the pronounced potentiality of DPN technique to control the structure of the SAM depending on the deposition conditions, and in particular on the writing speed. On this basis the connection between the physical properties of the hybrid organic-metal interface and its nanoscale morphology could be investigated. We believe that this is a key point in nanotechnology essential for the improvement and development of new electronic devices.

General conclusions

The ability to pattern nanostructures on a solid surface is essential to continue the miniaturization process and opens the way to the integration of new applications. From a more fundamental point of view, only by controlling the arrangement, morphology and composition of nanostructures it will be possible to understand and control their properties and to discover new phenomena. In this thesis work the patterning of nanostructures on gold surface was achieved by following different approaches, and the physical properties of the nanostructures were discussed and interpreted considering their morphology and surrounding. Scanning Probe Microscopies were the privileged tools to study the morphology of the considered nanostructures, but were also used as active tools to manipulate matter at the nanoscale.

A considerable part of the work were dedicated on Co on Au(111), a system which has been widely studied in literature. The Au(111) herringbone reconstruction drives the first stage of the Co growth towards the formation of well-ordered nanoisland arrays. In particular, we focused our attention on the size dependence of the magnetic behavior of the nanoislands. STM and MOKE studies were coupled in order to relate the activation energy for magnetization reversal E_a to the number of atoms N composing the islands. Our results have shown a clear deviation from the macrospin predictions, according to which $E_a = K N$, even for islands with a diameter of few nm. This result could be interpreted in terms of enhanced edge magnetic anisotropy but, thanks to atomic scale simulations, we rather attributed the discrepancy to thermal effects, which activate confined spin-wave excitations inside the islands.

On Au(111) the size of the islands can be easily adjusted, but it is hard to control their shape. In order to exercise a more extensive control on the islands morphology we employed a multilayer sample, where the Au(111) reconstruction is lifted to purely unilinear. This new template was employed to grow nanoislands with elongated shapes, a goal that was pursued through two routes. The first one relied on the temperature control over the diffusion barriers of adatoms, while the second one exploited the ordered Pt-Au surface

alloy as a seed layer to control the nucleation and growth. In this way we obtained nanoislands which are elongated in the same direction at macroscopic scale and with an aspect ratio up to 10. Preliminary magnetic measurements on Co nanoislands with elongated shape suggested that also in this case the magnetic behavior cannot be properly described by constructing an effective macrospin for the system. As a perspective, a systematic study of dependence between E_a and the island shape would permit to draw a complete picture of the influence of morphology on magnetization reversal in this system.

The capping of nanoislands with different metals has evidenced the rich variety of phenomena that arise at the interface. To this purpose cobalt was covered with a metal (platinum) and with an organic molecule (an alkanethiol). The interest around Pt was motivated mainly by the strong hybridization between this metal and Co. An important electronic effect is expected also for the alkanethiols adsorption, as a consequence of chemical bonding. We believe that the impact of interface electronic rearrangements has to be understood in order to control and tailor magnetic anisotropy. The change in Co magnetic properties was followed as a function of the structure of the overlayer, through a combination of STM and MOKE studies. In the case of Pt capping, clear differences in the growth of Pt and magnetism of Co were observed depending on the deposition conditions and were ascribed to the intermix tendency of the two metals. Insights about the role of the interface on Co magnetic anisotropy were obtained by comparing the effect of a Au (which was previously studied) and Pt overlayer. The opposite impact caused by the two noble metals capping urged us to individuate two different phenomena at the basis of the change in magnetic anisotropy. In the case of Au it was demonstrated that magnetoelasticity is the dominant effect, while we suggested that band hybridization prevails in the case of Pt.

The influence of a molecular overlayer on magnetic anisotropy is a new and emerging topic. The present study was possible thanks to the development of a simple and flexible method to evaporate molecules directly in ultra high vacuum. On Au, the monolayers obtained with this technique are highly ordered with respect to the SAMs assembled from solution. Monolayer were formed also on Co, but not organized in a crystalline arrangement. Interestingly, the magnetism of Co nanoislands and thin films is modified in a number of ways by dodecanethiol adsorption. In particular the magnetic anisotropy was markedly decreased in the case of nanoislands, while it was increased in the case of thin films, in different measure depending on their thickness. Ab initio calculations are planned in order to identify the physical phenomena which causes these changes. By playing with the backbone of the molecular components of the SAM, the magnetic anisotropy could be more widely tuned and ultimately designed for specific applications. Moreover, it will be interest-

ing of interest to use this molecule as barrier in tunnel magnetoresistance. The arrays of Co nanoislands can be used as mask to pattern thiols monolayer on Au surfaces, but the same goal was reached also by taking a different route. In the second part of my thesis work an AFM tip was used to deliver the molecular component of the SAM. The assembly takes place only locally and is accompanied by a change in the surface potential, which is due to the alignment of molecular dipoles. This allows to get quantitative information about the structure of the monolayer with KPFM, after overcoming the resolution limitation of this technique. For this reason we performed a study where the availability of a well-defined patterns was used to measure the contrast transfer function of KPFM. The combination of this with other AFM techniques permitted to distinguish between the structures that alkanethiols adopt on the surface according to the deposition conditions, revealing some insights into the assembly mechanism in DPN depositions. Depending on the molecular structure, the gold surface potential was finely changed.

Bibliography

- K. Ait-Mansour, P. Ruffieux, P. Grüning, R. Fasel, and O. Gröning. Positional and Orientational templating of C₆₀ molecules on the Ag/Pt(111) Strain-Relief Pattern. *J. Phys. Chem. C*, 113:5292, 2009.
- R. Allenspach, M. Stampanoni, and A. Bischof. Magnetic domains in thin epitaxial Co/Au(111) films. *Phys. Rev. Lett.*, 65:3344, 1990.
- J.G. Amar and F. Family. Critical Cluster Size: Island Morphology and Size Distribution in Submonolayer Epitaxial Growth. *Phys. Rev. Lett.*, 74:2066, 1995.
- T.L. Andrew, H.-Y. Tsai, and R. Menon. Confining Light to Deep Subwavelength Dimensions to Enable Optical Nanopatterning. *Science*, 324:917, 2009.
- J. Arbiol, F. Peiró, A. Cornet, C. Clavero, A. Cebollada, G. Armelles, and Y. Hutel. Capping layer effects in the structure and composition of Co nanoparticle ultrathin films. *Appl. Phys. Lett.*, 86:032150, 2005.
- P.N. Argyres. Theory of the Faraday and Kerr Effects in Ferromagnetics. *Phys. Rev.*, 97:334, 1955.
- G. Ashkenasy, D. Cahen, R. Cohen, A. Shanzer, and A. Vilat. Molecular Engineering of Semiconductor Surfaces and Devices. *Acc. Chem. Res.*, 35:121, 2002.
- A. Aspelmeier, M. Tischer, M. Farle, M. Russo, K. Baberschke, and D. Arvanitis. AC susceptibility measurements of magnetic monolayers: MCSD, MOKE, and mutual inductance. *J. Magn. Magn. Mat.*, 146:256, 1995.
- P.D. Augustus and J.P. Jones. The epitaxy of gold on (110) tungsten studied by LEED. *Surf. Sci.*, 64:713, 1977.
- S. Bader and E. Moog. SMOKE signals from ferromagnetic monolayers. *Superlattice Microstruct.*, 1:543, 1985.

- G. Bao and S. Suresh. Cell and molecular mechanics of biological materials. *Nat. Materials*, 2:715, 2003.
- C. Barraud, P. Seneor, R. Mattana, S. Fusil, K. Bouzehouane, C. Deranlot, P. Graziosi, L. Hueso, I. Bergenti, V. Dediu, F. Petroff, and A. Fert. Unraveling the role of the interface for spin injection into organic semiconductors. *Nature Phys.*, 6:615, 2010.
- R.J. Barsotti, S.M. O'Connell, and F. Stellacci. Morphology Control in Self-Assembled Monolayers Written by Dip Pen Nanolithography. *Langmuir*, 20:4795, 2004.
- J.V. Barth, H. Brune, G. Ertl, and R.J. Behm. Scanning tunneling microscopy observations on the reconstructed Au(111) surface: Atomic structure, long-range superstructure, rotational domains, and surface defects. *Phys. Rev. B*, 42:9307, 1990.
- J.V. Barth, G. Costantini, and K. Kern. Engineering atomic and molecular nanostructures. *Nature*, 437:671, 2005.
- E. Bauer, H. Poppa, G. Todd, and P.R. Davies. The adsorption and early stages of condensation of Ag and Au on W single-crystal surfaces. *J. Appl. Phys.*, 48:3773, 1977.
- P. Beauvillain, A. Bounouh, C. Chappert, R Mégy, S. Ould-Mahfoud, J.P. Renard, P. Veillet, D. Weller, and J. Corno. Effect of submonolayer coverage on magnetic anisotropy of ultrathin cobalt films M/Co/Au(111) with M=Au, Cu, Pd. *J. Appl. Phys.*, 76:6078, 1994.
- A. Berger, S. Knappmann, and H.P. Oepen. Magneto-optical Kerr effect study of ac susceptibilities in ultrathin cobalt films. *J. Appl. Phys.*, 75:5598, 1994.
- F. Besenbacher. Scanning tunnelling microscopy studies of metal surfaces. *Rep. Prog. Phys.*, 59:1737, 1996.
- G. Binnig, H. Rohrer, Ch. Gerber, and E. Weibel. Tunneling through a controllable vacuum gap. *Appl. Phys. Lett.*, 40:178, 1982a.
- G. Binnig, H. Rohrer, Ch. Gerber, and E. Weibel. Surface Studies by Scanning Tunneling Microscopy. *Phys. Rev. Lett.*, 49:57, 1982b.
- G. Binnig, C.F. Quate, and Ch. Gerber. Atomic Force Microscope. *Phys. Rev. Lett.*, 56:930, 1986.

- M. Bode, O. Pietzsch, A. Kubetzck, and R. Wiesendanger. Shape-Dependent Thermal Switching Behavior of Superparamagnetic Nanoislands. *Phys. Rev. Lett.*, 92:67201, 2004.
- M. Bode, E.Y. Vedemenko, K. Von Bergmann, A. Kubetza, P. Ferriani, S. Heinze, and R. Wiesendanger. Atomic spin structure of antiferromagnetic domain walls. *Nat. Materials*, 5:477, 2006.
- L. Bogani and W. Wernsdorfer. Molecular spintronics using single-molecule magnets. *Nature Mater.*, 7:179, 2008.
- M. Bott, T. Michely, and G. Comsa. The homoepitaxial growth of Pt on Pt(111) studied with STM. *Surf. Sci.*, 272:161, 1992.
- H. Braun. Thermally activated magnetization reversal in elongated ferromagnetic particles. *Phys. Rev. Lett.*, 71:3557, 1993.
- W.F. Brown. Thermal fluctuations of a Single-Domain Particle. *Phys. Rev.*, 130:1677, 1963.
- H. Brune. Microscopic view of epitaxial metal growth: nucleation and aggregation. *Surf. Sci. Rep.*, 31:121, 1998.
- H. Brune, H. Röder, C. Boragno, and K. Kern. Strain relief at hexagonal-close-packed interfaces. *Phys. Rev. B*, 49:2997, 1994.
- H. Brune, M. Giovannini, K. Bromann, and K. Kern. Self-organized growth of nanostructure arrays on strain-relief patterns. *Nature*, 394:451, 1998.
- P. Bruno. Tight-binding approach to the orbital magnetic moment and magnetocrystalline anisotropy of transition-metal monolayers. *Phys. Rev. B*, 39:865, 1989.
- H. Bulou and C. Massobrio. Dynamical behavior of Co adatoms on the herringbone reconstructed surface of Au(111). *Superlattice Microst.*, 36:305, 2004.
- H.B. Callen and E. Callen. The present status of the temperature dependence of magnetocrystalline anisotropy and the $l(l+1)/2$ power law. *J. Phys. Chem. Solids*, 27:1271, 1966.
- N. Camillone III, C.E.D. Chidsey, G.-Y. Liu, and G. Scoles. Superlattice structure at the surface of a monolayer of octadecanethiol self-assembled on Au(111). *J. Chem. Phys.*, 98:3503, 1993.

- N. Camillone III, T.Y.B. Leung, P. Schwartz, P. Eisenberger, and G. Scoles. Chain length dependence of the striped phases of alkanethiol monolayers self-assembled on Au(111): An atomic beam diffraction study. *Langmuir*, 12: 2737, 1996.
- I.H. Campbell, S. Rubin, T.A. Zawodzinski, J.D. Kress, R.L. Martin, D.L. Smith, N.N. Barashkov, and J.P. Ferraris. Controlling Schottky energy barriers in organic electronic devices using self-assembled monolayers. *Phys. Rev. B*, 54:R14321, 1996.
- I. Carmeli, F. Bloom, E.G. Gwinn, T.C. Kreutz, C. Scoby, A. C. Gossard, S. G. Ray, and R. Naaman. Molecular enhancement of ferromagnetism in GaAs/GaMnAs heterostructures. *Appl. Phys. Lett.*, 89:112508, 2006.
- A.N. Caruso, R. Rajesh, G. Gallup, J. Redepenning, and P.A. Dowben. Orientation and bonding of biphenyldimethyldithiol. *J. Phys.: Condens. Matter*, 16: 845, 2004.
- A.N. Caruso, L.G. Wang, S.S. Jaswal, E.Y. Tsymbal, and P.A. Dowben. The interface electronic structure of thiol terminated molecules on cobalt and gold surfaces. *J. Mater. Sci.*, 41:6198, 2006.
- I. Chado, C. Goyhenex, H. Bulou, and J.P. Bucher. Cluster critical size effect during growth on a heterogeneous surface. *Phys. Rev. B*, 69:085413, 2004.
- D.D. Chambliss, R.J. Wilson, and S. Chiang. Nucleation of ordered Ni island arrays on Au(111) by surface-lattice dislocations. *Phys. Rev. Lett.*, 66:1721, 1991.
- C.E.D. Chidsey and D.N. Loiacano. Chemical Functionality in Self-Assembled Monolayers: Structural and Electrochemical Properties. *Langmuir*, 6:682, 1990.
- S.Y. Chou, P.R. Krauss, and P.J. Renstrom. Imprint lithography with 25-nanometer resolution. *Science*, 272:85, 1996.
- P. Crespo, R. Litrán, T. C. Rojas, M. Multigner, J. M. de la Fuente, J. C. Sánchez-López, M. A. García, A. Hernando, S. Penadés, and A. Fernández. Permanent Magnetism, Magnetic Anisotropy, and Hysteresis of Thiol-Capped Gold Nanoparticles. *Phys. Rev. Lett.*, 93:87204, 2004.
- D.R.S. Cumming, S. Thoms, S.P. Beaumont, and J.M.R. Weaver. Fabrication of 3 nm wires using 100 keV electron beam lithography and poly(methyl methacrylate) resist. *Appl. Phys. Lett.*, 68:116073, 1996.

- J. A. Dagata, J. Schneir, H.H. Harary, C.J. Evans, M.T. Postek, and J. Bennett. Modification of hydrogen-passivated silicon by a scanning tunneling microscope operating in air. *Appl. Phys. Lett.*, 56:2001, 1990.
- H. Dai, N. Franklin, and J. Han. Exploiting the properties of carbon nanotubes for nanolithography. *Appl. Phys. Lett.*, 73:1508, 1998.
- O. Dannenberger, K. Weiss, H.-J. Himmel, B. Jäger, M. Buck, and C. Wöll. An orientation analysis of differently endgroup-functionalised alkanethiols adsorbed on Au substrates. *Thin Solid Films*, 307:183, 1997.
- B. de Boer, A. Hadipour, M.M. Mandoc, T. van Woudenberg, and P.W.M. Blom. Tuning of Metal Work Functions with Self-Assembled Monolayers. *Adv. Mater.*, 17:621, 2005.
- V. Dediu, M. Murgia, F. C. Maticotta, C. Taliani, and S. Barbanera. Room temperature spin polarized injection in organic semiconductor. *Solid State Commun.*, 122:181, 2002.
- V. A. Dediu, L. E. Hueso, I. Bergenti, and C. Taliani. Spin routes in organic semiconductors. *Nature Mater.*, 8:707, 2009.
- E. Delamarche, B. Michel, Ch. Gerber, D. Anselmetti, H.-J. Güntherodt, H. Wolf, and H. Ringsdorf. Real-space observation of nanoscale molecular domains in self-assembled monolayers. *Langmuir*, 10:2869, 1994.
- L.M. Demers, T.A. Taton S.-J. Park, Z. Li, and C.A. Mirkin. Orthogonal Assembly of Nanoparticle Building Blocks on Dip-Pen Nanolithographically Generated Templates of DNA. *Angew. Chem., Int. Ed.*, 40:3071, 2001.
- C. Didiot, S. Pons, B. Kierren, Y. Fagot-Revurat, and D. Malterre. Nanopatterning the electronic properties of gold surfaces with self-organized superlattices of metallic nanostructures. *Nat. Nanotechnol.*, 2:617, 2007.
- A. Dmitriev, N. Lin, J. Weckesser, J.V. Barth, and K. Kern. Supramolecular Assemblies of Trimesic Acid on a Cu(100) Surface. *J. Phys. Chem. B*, 106:6907, 2002.
- K. Edinger, A. Götzhäuser, K. Demota, C. Wöll, and M. Grunza. Formation of Self-Assembled Monolayers of *n*-Alkanethiols on Gold: A Scanning Tunneling Microscopy Study on the Modification of Substrate Morphology. *Langmuir*, 9:4, 1993.
- D.M. Eigler and E.K. Schweizer. Positioning single atoms with a scanning tunneling microscope. *Nature*, 344:524, 1990.

- J.A.A.W. Elemans, S. Lei, and S. De Feyter. Molecular and Supramolecular Networks on Surfaces: From Two-Dimensional Crystal Engineering to Reactivity. *Angew. Chem., Int. Ed.*, 48:7298, 2009.
- Jakob Engbæk and Jakob Schiøtz. Atomic structure of screw dislocations intersecting the Au(111) surface: A combined scanning tunneling microscopy and molecular dynamics study. *Phys. Rev. B*, 74:195434, 2006.
- B. Engel, M. Wiedmann, R. Van Leeuwen, and C. Falco. Anomalous magnetic anisotropy in ultrathin transition metals. *Phys. Rev. Lett.*, 48:9894, 1993.
- B Fischer, H Brune, JV Barth, A Fricke, and K Kern. Nucleation kinetics on inhomogeneous substrates: Al/Au (111). *Phys. Rev. Lett.*, 82:1732, 1999.
- M. Fonin, Y. Dedkov, U. Rüdiger, and G. Güntherodt. Growth and structure of Mn on Au(111) at room temperature. *Surf. Sci.*, 529:L275, 2003.
- O. Fruchart and A. Thiaville. Magnetism in reduced dimensions. *C. R. Physique*, 6:921, 2005.
- O. Fruchart, H. Tolentino, M. De Santis, C. Goyhenex, H. Bulou, C. Clavero, M. Przybylski, and J. Kirschner. *to be published*.
- O. Fruchart, P.O. Jubert, C. Meyer, M. Klaua, J. Barthel, and J. Kirschner. Vertical self-organization of epitaxial magnetic nanostructures. *J. Magn. Magn. Mat.*, 239:224, 2002.
- O. Fruchart, G. Renaud, A. Barbier, M. Noblet, O. Ulrich, J.-P. Deville, F. Scheurer, J. Mane-Mane, V. Repain, G. Baudot, and S. Rousset. X-ray super-cell crystallography of self-organized Co/Au(111) deposits. *Europhys. Lett.*, 63:275, 2003.
- P. Gambardella, M. Blanc, H. Brune, K. Kuhnke, and K. Kern. One-dimensional metal chains on Pt vicinal surfaces. *Phys. Rev. B*, 61:2254, 2000.
- P. Gambardella, S. Rusponi, M. Veronese, S. S. Dhesi, C. Grazioli, A. Dallmeyer, I. Cabria, R. Zeller, P. H. Dederichs, K. Kern, C. Carbone, and H. Brune. Giant Magnetic Anisotropy of Single Cobalt Atoms and Nanoparticles. *Science*, 300:1130, 2003.
- P. Gambardella, A. Dallmeyer, K. Maiti, M.C. Malagoli, S. Rusponi, P. Ohresser, W. Eberhardt, C. Carbone, and K. Kern. Oscillatory Magnetic Anisotropy in One-Dimensional Atomic Wires. *Phys. Rev. Lett.*, 93:77203, 2004.

- P. Gambardella, H. Brune, K. Kern, and V.I. Marchenko. Equilibrium island-size distribution in one dimension. *Phys. Rev. B*, 73:245425, 2006.
- P. Gambardella, S. Stepanow, A. Dmitriev, J. Honolka, F. M. F. de Groot, M. Lingenfelder, S. Sen Gupta, D. D. Sarma, P. Bencok, S. Stanescu, S. Clair, S. Pons, N. Lin, A. P. Seitsonen, H. Brune, J. V. Barth, and K. Kern. Supramolecular control of the magnetic anisotropy in two-dimensional high-spin Fe arrays at a metal interface. *Nature Mater.*, 8:189, 2009.
- B.D. Gates, Q. Xu, M. Stewart, D. Ryan, C.G. Wilson, and G.M. Whitesides. New approaches to nanofabrication: molding, printing and other techniques. *Chem. Rev.*, 105:1171, 2005.
- E.J. Giessibl. Atomic Resolution of the Silicon (111)-(7×7) Surface by Atomic Force Microscopy. *Science*, 267:68, 1995.
- D.S. Ginger, H. Zhang, and C.A. Mirkin. The Evolution of Dip-Pen Nanolithography. *Angew. Chem., Int. Ed.*, 43:30, 2004.
- C. Goyhenex and H. Bulou. Theoretical insight in the energetics of Co adsorption on a reconstructed Au(111) substrate. *Phys. Rev. B*, 63:235404, May 2001.
- L. Gross, F. Mohn, N. Moll, P. Liljeroth, and G. Meyer. The Chemical Structure of a Molecule Resolved by Atomic Force Microscopy. *Science*, 325:1110, 2009.
- C. Günther, J. Vrijmoeth, R.Q. Hwang, and R.J. Behm. Strain Relaxation in Hexagonally Close-Packed Metal-Metal Interfaces. *Phys. Rev. Lett.*, 74:754, 1995.
- J. Haisma, M. Verheijen, K. van den Heuvel, and J. van den Berg. Mold-assisted nanolithography: A process for reliable pattern replication. *J. Vac. Sci. Technol., B*, 14:4124, 1996.
- M. Hegner, P. Wagner, and G. Semenza. Ultralarge atomically flat template-stripped Au surfaces for scanning probe microscopy. *Surf. Sci.*, 291:39, 1993.
- S.-W. Hla, K.-F. Braun, B. Wassermann, and K.-H. Rieder. Controlled Low-Temperature Molecular Manipulation of Sexiphenyl Molecules on Ag(111) Using Scanning Tunneling Microscopy. *Phys. Rev. Lett.*, 93:208302, 2004.
- P.G. Hoertz, J.R. Niskala, P. Dai, H.T. Black, and W. You. Comprehensive Investigation of Self-Assembled Monolayer Formation on Ferromagnetic Thin Film Surfaces. *J. Am. Chem. Soc.*, 130:9763, 2008.

- J. Hong, R. Q. Wu, J. Lindner, E. Kosubek, and K. Baberschke. Manipulation of Spin Reorientation Transition by Oxygen Surfactant Growth: A Combined Theoretical and Experimental Approach. *Phys. Rev. Lett.*, 92:147202, 2004.
- I. Horcas, R. Fernández, J. M. Gómez-Rodríguez, J. Colchero, J. Gómez-Herrero, and A. M. Baro. WSxM: A software for scanning probe microscopy and a tool for nanotechnology WSXM: A software for scanning probe microscopy and a tool for nanotechnology. *Rev. Sci. Instrum.*, 78:013705, 2007.
- F. Hua, Y. Sun, A. Gaur, M.A. Meitl, L. Bilhaut, L. Rotkina, J. Wang, P. Geil, M. Shim, and J.A. Rogers. Polymer Imprint Lithography with Molecular-Scale Resolution. *Nano Lett.*, 4:2467, 2004.
- L.E. Hueso, J.M. Pruneda, V. Ferrari, G. Burnell, J.P. Valdés-Herrera, B.D. Simons, P.B. Littlewood, E. Artacho, A. Fert, and N.D. Mathur. Transformation of spin information into large electrical signals using carbon nanotubes. *Nature*, 445:410, 2007.
- A.W. Hull. X-ray crystal analysis of thirteen common metals. *Phys. Rev.*, 17:571, 1921.
- R.Q. Hwang, J. Schröder, C. Günther, and R.J. Behm. Fractal Growth of Two-Dimensional Islands: Au on Ru(0001). *Phys. Rev. Lett.*, 67:3279, 1991.
- H. Ibach. The role of surface stress in reconstruction, epitaxial growth and stabilization of mesoscopic structures. *Surf. Sci. Rep.*, 29:193, 1997.
- T. Ito and S. Okazaki. Pushing the limits of lithography. *Nature*, 406:1027, 2000.
- H.O. Jacobs, P. Leuchtman, O.J. Homan, and A. Stemmer. Resolution and contrast in Kelvin probe force microscopy. *J. Appl. Phys.*, 84:1168, 1998.
- M. Jamet, W. Wernsdorfer, C. Thirion, D. Mailly, V. Dupuis, P. Mélinon, and A. Pérez. Magnetic Anisotropy of a Single Cobalt Nanocluster. *Phys. Rev. Lett.*, 86:4676, 2001.
- J. Jang, S. Hong, G.C. Schatz, and M.A. Ratner. Self-assembly of ink molecules in dip-pen nanolithography: A diffusion model. *J. Chem. Phys.*, 115:2721, 2001.
- A. Jo, W. Joo, W.-H. Jin, H. Nam, and J.K. Kim. Ultrahigh-density phase-change data storage without the use of heating. *Nat. Nanotechnol.*, 4:727, 2009.

- S. Krämer, R.R. Fuieler, and C.B. Gorman. Scanning probe lithography using self-assembled monolayers. *Chem. Rev.*, 103:4367, 2003.
- S. Krause, G. Herzog, T. Stapelfeldt, L. Berbil-Bautista, M. Bode, E. Y. Vedmedenko, and R. Wiesendanger. Magnetization Reversal of Nanoscale Islands: How Size and Shape Affect the Arrhenius Prefactor. *Phys. Rev. Lett.*, 103:127202, 2009.
- T.C. Kreutz, E.G. Gwinn, R. Artzi, R. Naaman, H. Pizem, and C.N. Sukenik. Modification of ferromagnetism in semiconductors by molecular monolayers. *Appl. Phys. Lett.*, 83:4211, 2006.
- F. Krok, K. Sajewicz, J. Konior, M. Goryl, P. Piatkowski, and M. Szymonski. Lateral resolution and potential sensitivity in Kelvin probe force microscopy: Towards understanding of the sub-nanometer resolution. *Phys. Rev. B*, 77:235427, 2008.
- A. Kumar and G.M. Whitesides. Features of gold having micrometer to centimeter dimensions can be formed through a combination of stamping with an elastomeric stamp and an alkanethiol “ink” followed by chemical etching. *Appl. Phys. Lett.*, 63:2002, 1993.
- M. Lackinger, S. Greissl, T. Markert, F. Jamitzky, and M. Heckl. Self-Assembly of Benzene-Dicarboxylic Acid Isomers at the Liquid Solid Interface: Steric Aspects of Hydrogen Bonding. *J. Phys. Chem. B*, 108:13652, 2004.
- J. Lahtinen, P. Kantola, S. Jaatinen, K. Habermehl-Cwirzen, P. Salo, J. Vuorinen, M. Lindroos, K. Pussi, and A.P. Seitsonen. LEED and DFT investigation on the (2×2)-S overlayer on Co(0001). *Surf. Sci.*, 599:113, 2005.
- P.E. Laibinis and G.M. Whitesides. Self-Assembled Monolayers of *n*-Alkanethiolates on Copper Are Barrier Films That Protect the Metal against Oxidation by Air. *J. Am. Chem. Soc.*, 114:9022, 1992.
- K.-B. Lee, S.-J. Park, C.A. Mirkin, J.C. Smith, and M. Mrksich. Protein Nanoarrays Generated By Dip-Pen Nanolithography. *Science*, 295:1702, 2002.
- J.-M. Lehn. *Supramolecular Chemistry: Concept and Perspectives*. VCH, 1995.
- J.-C. Lévy, M. Krawczyk, and H. Puzskarski. Magnons in Co dots. *J. Magn. Magn. Mat.*, 305:182, 2006.
- J.-L. Li, J.-F. Jia, X.-J. Liang, X. Liu, J.-Z. Wang, Q.-K. Xue, Z.-Q. Li, J.-S. Tse, Z. Zhang, and S.B. Zhang. Spontaneous Assembly of Perfectly Ordered Identical-Size Nanocluster Arrays. *Phys. Rev. Lett.*, 88:066101, 2002.

- M. Li, Y. Han, P.A. Thiel, and J.W. Evans. Formation of complex wedding-cake morphologies during homoepitaxial film growth of Ag on Ag(111): atomistic, step-dynamics, and continuum modeling. *J. Phys.: Condens. Matter*, 21:084216, 2009.
- A. Liscio, V. Palermo, and P. Samorí. Probing Local Surface Potential of Quasi-One-Dimensional Systems: A KPFM Study of P3HT Nanofibers. *Adv Funct. Mat.*, 18:907, 2008.
- G.-Y. Liu, S. Xu, and Y. Qian. Nanofabrication of Self-Assembled Monolayers Using Scanning Probe Lithography. *Acc. Chem. Res.*, 33:457, 2000.
- X. Liu, L. Fu, S. Hong, V.P. Dravid, and C.A. Mirkin. Arrays of Magnetic Nanoparticles Patterned via 'Dip-Pen' Nanolithography. *Adv. Mater.*, 14: 231, 2002.
- J.C. Love, L.E. Estroff, J.K. Kriebel, R.G. Nuzzo, and G.M. Whitesides. Self-Assembled Monolayers of Thiolates on Metals as a Form of Nanotechnology. *Chem. Rev.*, 105:1103, 2005.
- J. Lü, E. Delamarche, L. Eng, R. Bennewitz, E. Meyer, and H.-J. Güntherodt. Kelvin Probe Force Microscopy on Surfaces: Investigation of the Surface Potential of Self-Assembled Monolayers on Gold. *Langmuir*, 15:8184, 1999.
- X. Lu, M. Grobis, K.H. Khoo, S.G. Louie, and M.F. Crommie. Spatially Mapping the Spectral Density of a Single C₆₀ Molecule. *Phys. Rev. Lett.*, 90:096802, 2003.
- F. Luis, J. Bartolomé, F. Bartolomé, M.J. Martínez, L.M. García, F. Petroff, C. Deranlot, F. Wilhelm, and A. Rogalev. Enhancement of the magnetic anisotropy of Co clusters by Au capping. *J. Appl. Phys.*, 99:08G705, 2006.
- S. H. Ma, Z.Y. Jiao, and Z.X. Yang. Coverage effects on the adsorption of sulfur on Co(0001): A DFT study. *Surf. Sci.*, 604:817, 2010.
- S.H. Ma, X.T. Zu, Z.Y. Jiao, and H.Y. Xiao. Effect of S adsorption on magnetic Co(0001) surface: a DFT study. *Eur. Phys. J. B*, 61:319, 2008.
- X.-D Ma, D.I. Bazhanov, O. Fruchart, F. Yildiz, T. Yokoyama, M. Przybylski, V.S. Stepanyuk, W. Hergert, and J. Kirschner. Strain Relief Guided Growth of Atomic Nanowires in a Cu₃N – Cu(110) Molecular Network. *Phys. Rev. Lett.*, 102:205503, 2009.
- H.J. Mamin. Thermal writing using a heated atomic force microscope tip. *Appl. Phys. Lett.*, 69:433, 1996.

- T. Maruyama, Y. Shiota, T. Nozaki, K. Ohta, N. Toda, M. Mizuguchi, A.A. Tulapurkar, T. Shinjo, M. Shiraishi, S. Mizukami, Y. Ando, and Y. Suzuki. Large voltage-induced magnetic anisotropy change in a few atomic layers of iron. *Nat. Nanotechnol.*, 4:158, 2008.
- D. Matsumura, T. Yokoyama, K. Amemiya, S. Kitagawa, and T. Ohta. X-ray magnetic circular dichroism study of spin reorientation transitions of magnetic thin films induced by surface chemisorption. *Phys. Rev. B*, 66:024402, 2002.
- C.A. McDermott, M.T. McDermott, J.-B. Green, and M.D. Porter. Structural Origins of the Surface Depressions at Alkanethiolate Monolayers on Au(111): A Scanning Tunneling and Atomic Force Microscopic Investigation. *J. Phys. Chem.*, 99:13257, 1995.
- D. Mercier, J.-C.S. Lévy, G. Viau, F. Fiévet-Vincent, F. Fiévet, P. Toneguzzo, and O. Acher. Magnetic resonance in spherical Co-Ni and Fe-Co-Ni particles. *Phys. Rev. B*, 62:532, 2000.
- J.A. Meyer, I.D. Baikie, E. Kopatzki, and R.J. Behm. Preferential island nucleation at the elbows of the Au(111) herringbone reconstruction through place exchange. *Surf. Sci.*, 365:L647, 1996.
- W. Mizutani, T. Ishida, and H. Tokumoto. Nanoscale Reversible Molecular Extraction from a Self-Assembled Monolayer on Gold(111) by a Scanning Tunneling Microscope. *Langmuir*, 14:7197, 1998.
- N. Moreau. *Croissance, structure et magnétisme de nano-alliages (Co,Pt) supportés*. PhD thesis, Université Denis Diderot - Paris 7, 2010.
- W.J.M. Naber, S. Faez, and W.G. van der Wiel. Organic spintronics. *J. Phys. D: Appl. Phys.*, 40:205, 2007.
- Y. Nahas, V. Repain, C. Chacon, Y. Girard, J. Lagoute, G. Rodary, J. Klein, S. Rousset, H. Bulou, and C. Goyhenex. Dominant Role of the Epitaxial Strain in the Magnetism of Core-Shell Co/Au Self-Organized Nanodots. *Phys. Rev. Lett.*, 103:829, 2009.
- Y. Nahas, V. Repain, C. Chacon, Y. Girard, and S. Rousset. Interplay between ordered growth and intermixing of Pt on patterned Au surfaces. *Surf. Sci.*, 604, 2010.
- N. Nakajima, T. Koide, T. Shidara, H. Miyauchi, H. Fukutani, A. Fujimori, K. Iio, T. Katayama, M. Nývlt, and Y. Suzuki. Perpendicular Magnetic Anisotropy

- Caused by Interfacial Hybridization via Enhanced Orbital Moment in Co/Pt Multilayers: Magnetic Circular X-Ray Dichroism Study. *Phys. Rev. Lett.*, 81: 5229, 1998.
- S. Narasimhan and D. Vanderbilt. Elastic stress domains and the herringbone reconstruction on Au(111). *Phys. Rev. Lett.*, 69:1564, 1992.
- A.T. N'Diaye, T. Gerber, C. Busse, J. Mysliveček, J. Coraux, and T. Michely. A versatile fabrication method for cluster superlattices. *New J. Phys.*, 11: 103045, 2009.
- L. Néel. Théorie du traînage magnétique des ferromagnétiques en grains fins avec application aux terres cuites. *Ann. Géophys.*, 5:99, 1949.
- L. Néel. Anisotropie magnétique superficielle et surstructures d'orientation. *J. Phys. Rad.*, 15:225, 1954.
- S.G. Nelson, M.J.S. Spencer, I.K. Snook, and I. Yarovsky. Effect of S contamination on properties of Fe(100) surfaces. *Surf. Sci.*, 590:63, 2005.
- M. Nonnenmacher, M.P. O'Boyle, and H.K. Wickramasinghe. Kelvin probe force microscopy. *Appl. Phys. Lett.*, 58:2921, 1991.
- R.G. Nuzzo, E.M. Korenic, and L.H. Dubois. Studies of the temperature dependent phase behavior of long chain *n*-alkyl thiol monolayer on gold. *J. Chem. Phys.*, 93:767, 1990.
- S. Padovani, P. Molin -Mata, F. Scheurer, and J.P. Bucher. Variable temperature STM and Kerr studies of ultrathin films of Co on Au(111): from self-organized clusters to continuous films. *Appl. Phys. A*, 66:S1199, 1998.
- S. Padovani, I. Chado, F. Scheurer, and J.P. Bucher. Transition from zero-dimensional superparamagnetism to two-dimensional ferromagnetism of Co clusters on Au(111). *Phys. Rev. B*, 59:71815, 1999.
- S. Padovani, F. Scheurer, I. Chado, and J.P. Bucher. Anomalous magnetic anisotropy of ultrathin Co films grown at 30 K on Au(111). *Phys. Rev. B*, 61:72, 2000.
- V. Palermo, M. Palma, and P. Samor . Electronic Characterization of Organic Thin Films by Kelvin Probe Force Microscopy. *Adv. Mater.*, 18:145, 2006.
- P.M. Paulus, F. Luis, M. Kr ll, G. Schmid, and L.J. de Jongh. Low-temperature study of the magnetization reversal and magnetic anisotropy of Fe, Ni, and Co nanowires. *J. Magn. Magn. Mat.*, 224:180, 2001.

- M. Pedersen, S. Helveg, A. Ruban, I. Stensgaard, E. Laegsgaard, J.K. Norskov, and F. Besenbacher. How a gold substrate can increase the reactivity of a Pt overlayer. *Surf. Sci.*, 426:395, 1999.
- D. Peterka, A. Enders, G. Haas, and K. Kern. Adsorbate and thermally induced spin reorientation transition in low-temperature-grown Fe/Cu(001). *Phys. Rev. Lett.*, 66:2889, 2002.
- E.J. Peterson, B.L. Weeks, J.J. De Yoreo, and P.V. Schwartz. Effect of Environmental Conditions on Dip Pen Nanolithography of Mercaptohexadecanoic Acid. *J. Phys. Chem. B*, 108:15206, 2004.
- J.R. Petta, S.K. Slater, and D.C. Ralph. Spin-Dependent Transport in Molecular Tunnel Junctions. *Phys. Rev. Lett.*, 93:136601, 2004.
- U.H. Pi, M.S. Jeong, J.H. Kim, H.Y. Yu, C.W. Park, H. Lee, and S.-Y. Choi. Current flow through different phases of dodecanethiol self-assembled monolayer. *Surf. Sci.*, 583:88, 2005.
- R.D. Piner, J. Zhu, F. Xu, S.H. Hong, and C.A. Mirkin. 'Dip-Pen' Nanolithography. *Science*, 283:661, 1999.
- D. Pires, J.L. Hedrick, A. De Silva, J. Frommer, B. Gotsmann, H. Wolf, M. Despont, U. Duerig, and A.W. Knoll. Nanoscale Three-Dimensional Patterning of Molecular Resists by Scanning Probes. *Science*, 328:732, 2010.
- G.E. Poirier. Characterization of organosulfur molecular monolayers on Au (111) using scanning tunneling microscopy. *Chem. Rev.*, 97:1117, 1997a.
- G.E. Poirier. Mechanism of formation of Au vacancy islands in alkanethiol monolayers on Au(111). *Langmuir*, 13:2019, 1997b.
- G.E. Poirier. Coverage-dependent phases and phase stability of decanethiol on Au(111). *Langmuir*, 15:1167, 1999.
- G.E. Poirier and E.D. Pylant. The self-assembly mechanism of alkanethiols on Au(111). *Science*, 272:1145, 1996.
- G.E. Poirier, W.P. Fitts, and J.M. White. Two-Dimensional Phase Diagram of Decanethiol on Au(111). *Langmuir*, 17:1176, 2001.
- S. Pütter, H.F. Ding, Y.T. Millev, H.P. Oepen, and J. Kirschner. Magnetic susceptibility: An easy approach to the spin-reorientation transition. *Phys. Rev. B*, 64:92409, 2001.

- Z.Q. Qiu and S.D. Bader. Surface magneto-optic Kerr effect. *Rev. Sci. Instrum.*, 71:1243, 2000.
- V. Repain, J.M. Berroir, S. Rousset, and J. Lecoœur. Interaction between steps and reconstruction on Au(111). *Europhys. Lett.*, 47:435, 1999.
- V. Repain, G. Baudot, H. Ellmer, and S. Rousset. Two-dimensional long-range ordered growth of uniform cobalt nanostructures on Au(111) vicinal template. *Europhys. Lett.*, 58:730, 2002.
- V. Repain, S. Rohart, Y. Girard, A. Tejada, and S. Rousset. Building uniform and long-range ordered nanostructures on a surface by nucleation on a point defect array. *J. Phys.: Condens. Matter*, 18:S17, 2006.
- M. Respaud, M. Goiran, J.M. Broto, F.H. Yang, T. Ould Ely, C. Amiens, and B. Chaudret. High-frequency ferromagnetic resonance on ultrafine cobalt particles. *Phys. Rev. B*, 59:R3934, 1999.
- G. Rodary, V. Repain, R.L. Stamps, Y. Girard, S. Rohart, A. Tejada, and S. Rousset. Unpublished data.
- G. Rodary, V. Repain, R.L. Stamps, Y. Girard, S. Rohart, A. Tejada, and S. Rousset. Influence of grain boundaries on the magnetization reorientation transition in ultrathin films. *Phys. Rev. B*, 75:184415, 2007.
- H. Röder, E. Hahn, H. Brune, J.P. Bucher, and K. Kern. Building one- and two-dimensional nanostructures by diffusion-controlled aggregation at surfaces. *Nature*, 366:141, 1993.
- S. Rohart, G. Baudot, V. Repain, Y. Girard, S. Rousset, H. Bulou, C. Goyhenex, and L. Proville. Atomistic mechanisms for the ordered growth of Co nanodots on Au(788): a comparison between VT-STM experiments and multi-scaled calculations. *Surf. Sci.*, 559:47, 2004.
- S. Rohart, V. Repain, A. Tejada, P. Ohresser, F. Scheurer, P. Bencok, J. Ferré, and S. Rousset. Distribution of the magnetic anisotropy energy of an array of self-ordered Co nanodots deposited on vicinal Au(111): X-ray magnetic circular dichroism measurements and theory. *Phys. Rev. B*, 73:165412, 2006.
- S. Rohart, V. Repain, A. Thiaville, and S. Rousset. Limits of the macrospin model in cobalt nanodots with enhanced edge magnetic anisotropy. *Phys. Rev. B*, 76:104401, 2007.

- S. Rousset, V. Repain, G. Baudot, Y. Garreau, and J. Lecoer. Self-ordering of Au(111) vicinal surfaces and application to nanostructure organized growth. *J. Phys.: Condens. Matter*, 15:S3363, 2003.
- S. Rousset, B. Croset, Y. Girard, G. Prevôt, V. Repain, and S. Rohart. Self-organized epitaxial growth on spontaneously nano-patterned templates. *C. R. Physique*, 6:33, 2005.
- S. Rozhok, R.D. Piner, and C.A. Mirkin. Dip-Pen Nanolithography: What Controls Ink Transport? *J. Phys. Chem. B*, 107:751, 2003.
- S. Rusponi, T. Cren, N. Weiss, M. Epple, P. Bulushek, L. Claude, and H. Brune. The remarkable difference between surface and step atoms in the magnetic anisotropy of two-dimensional nanostructures. *Nature Mater.*, 2:546, 2003.
- P.C. Rusu and G. Brocks. Surface Dipoles and Work Functions of Alkylthiolates and Fluorinated Alkylthiolates on Au(111). *J. Phys. Chem. B*, 110:22628, 2006.
- K. Salaita, Y Y. Wang, J. Fragala, R.A. Vega, C. Liu, and C.A. Mirkin. Massively Parallel Dip-Pen Nanolithography with 55000-Pen Two-Dimensional Arrays. *Angew. Chem., Int. Ed.*, 45:7220, 2006.
- K. Salaita, Y. Wang, and C.A. Mirkin. Applications of dip-pen nanolithography. *Nat. Nanotechnol.*, 2:145, 2007.
- D. Sander. The magnetic anisotropy and spin reorientation of nanostructures and nanoscale films. *J. Phys.: Condens. Matter*, 16:R603, 2004.
- D. Sander, W. Pan, S. Ouazi, and J. Kirschner. Reversible H-Induced Switching of the Magnetic Easy Axis in Ni/Cu(001) Thin Films. *Phys. Rev. Lett.*, 93:247203, 2004.
- S. Sanvito. The rise of spinterface science. *Nature Phys.*, 6:562, 2010.
- O Schaff, A.K. Schmid, N.C. Bartelt, J. de la Figuera, and R.Q. Hwang. In-situ STM studies of strain-stabilized thin-film dislocation networks under applied stress. *Mater. Sci. Eng. A*, 319:914, 2001.
- A. Scheybal, T. Ramsvik, R. Bertschinger, M. Putero, F. Nolting, and T. A. Jung. Induced magnetic ordering in a molecular monolayer. *Chem. Phys. Lett.*, 41:214, 2005.
- M. Schmid, G. Kresse, A. Buchsbaum, E. Napetschnig, S. Gritschneider, M. Reichling, and P. Varga. Nanotemplate with Holes: Ultrathin Alumina on Ni₃Al(111). *Phys. Rev. Lett.*, 99:196104, 2007.

- C. Schönenberger, J. Jorritsma, J.A.M. Sondag-Huethorst, and L.G.J. Fokkink. Domain structure of self-assembled alkanethiol monolayers on gold. *J. Phys. Chem.*, 99:3259, 1995.
- F. Schreiber. Structure and growth of self-assembling monolayers. *Prog. Surf. Sci.*, 65:151, 2000.
- F. Schreiber, A. Eberhardt, T. Leung, P. Schwartz, S. Wetterer, D. Lavrich, L. Berman, P. Fenter, P. Eisenberger, and G. Scoles. Adsorption mechanisms, structures, and growth regimes of an archetypal self-assembling system: Decanethiol on Au(111). *Phys. Rev. B*, 57:12476, 1998.
- P.V. Schwartz. Molecular Transport from an Atomic Force Microscope Tip: A Comparative Study of Dip-Pen Nanolithography. *Langmuir*, 18:4041, 2002.
- A.K. Sinensky and A.M. Belcher. Label-free and high-resolution protein/DNA nanoarray analysis using Kelvin probe force microscopy. *Nat. Nanotechnol.*, 2:653, 2007.
- R. Skomski. *Simple Models of Magnetism*. Oxford University Press, 2008.
- R. Skomski, H. Oepen, and J. Kirschner. Micromagnetics of ultrathin films with perpendicular magnetic anisotropy. *Phys. Rev. B*, 58:3223, 1998.
- A.W. Stephenson, C.J. Baddeley, M.S. Tikhov, and R.M. Lambert. Nucleation and growth of catalytically active Pd islands on Au(111)- $22 \times \sqrt{3}$ studied by scanning tunnelling microscopy. *Surf. Sci.*, 398:172, 1998.
- J. Stöhr. Exploring the microscopic origin of magnetic anisotropies with X-ray magnetic circular dichroism (XMCD) spectroscopy. *J. Magn. Magn. Mat.*, 200:407, 1999.
- E.C. Stoner and E.P. Wohlfarth. A mechanism of magnetic hysteresis in heterogeneous alloys. *Philos T. Roy Soc. A*, 240:599, 1948.
- Y. Sugimoto, P. Pou, O. Custance, P. Jelinek, M. Abe, R. Perez, and S. Morita. Complex patterning by vertical interchange atom manipulation using atomic force microscopy. *Science*, 322:413, 2008.
- M. Suzuki, H. Muraoka, Y. Inaba, H. Miyagawa, N. Kawamura, T. Shimatsu, H. Maruyama, N. Ishimatsu, Y. Isohama, and Y. Sonobe. Depth profile of spin and orbital magnetic moments in a subnanometer Pt film on Co. *Phys. Rev. B*, 72:054430, 2005.

- G. Szulczewski, S. Sanvito, and M. Coey. A spin of their own. *Nature Mater.*, 8: 693, 2009.
- U. Tartaglino, E. Tosatti, D. Passerone, and F. Ercolessi. Bending strain-driven modification of surface reconstructions: Au(111). *Phys. Rev. B*, 65:241406, 2002.
- F. Terán Arce, M.E. Vela, R.C. Salvarezza, and A.J. Arvia. The dynamic behavior of butanethiol and dodecanethiol adsorbates on Au(111) terraces. *J. Chem. Phys.*, 109:5703, 1998.
- C. Tölkes, P. Zeppenfeld, M.A. Krzyzowski, R. David, and G. Comsa. Preparation of well-ordered cobalt nanostructures on Au(111). *Phys. Rev. B*, 55: 80178, 1997.
- E. Tronc, D. Fiorani, M. Noguès, A. M. Testa, F. Lucari, F. D’Orazio, J.M. Grenèche, W. Wernsdorfer, N. Galvez, C. Chanéac, D. Mailly, and J.P. Jolivet. Surface effects in noninteracting and interacting γ -Fe₂O₃ nanoparticles. *J. Magn. Magn. Mat.*, 262:6, 2003.
- K. Tsukagoshi, B. W. Alphenaar, and H. Ago. Coherent transport of electron spin in a ferromagnetically contacted carbon nanotube. *Nature*, 401:572, 1999.
- A. Ulman. Formation and structure of Self-Assembled Monolayers. *Chem. Rev.*, 96:1533, 1996.
- G. van der Laan, M. A. Hoyland, M. Surman, C. F. J. Flipse, and B. T. Thole. Surface orbital magnetic moment of ferromagnetic nickel studied by magnetic circular dichroism in Ni3*p* core level photoemission. *Phys. Rev. Lett.*, 69:3827, 1992.
- J. Venables. *Introduction to surface and thin film processes*. Cambridge University Press, 2000.
- J. Venables, G. Spiller, and M. Hanbücken. Nucleation and growth of thin films. *Rep. Prog. Phys.*, 47:399, 1984.
- P. Vettiger, G. Cross, M. Despont, U. Drechsler, U. Dürig, B. Gotsmann, W. Häberle, M.A. Lantz, H.E. Rothuizen, R. Stutz, and G.K. Binnig. The ‘Millipede’ Nanotechnology Entering Data Storage. *IEEE Trans. Nanotechnol.*, 1:39, 2002.

- B. Voigtländer, G. Meyer, and N.M. Amer. Epitaxial growth of thin magnetic cobalt films on Au(111) studied by scanning tunneling microscopy. *Phys. Rev. B*, 44:10354, 1991a.
- B. Voigtländer, G. Meyer, and N.M. Amer. Epitaxial growth of Fe on Au(111): a scanning tunneling microscopy investigation. *Surf. Sci.*, 225:L529, 1991b.
- R. Vollmer, T. Gutjahr-Löser, J. Kirschner, S. Van Dijken, and B. Poelsema. Spin-reorientation transition in Ni films on Cu (001): the influence of H₂ adsorption. *Phys. Rev. B*, 60:2895, 1999.
- C. Vouille, A. Thiaville, and J. Miltat. Thermally activated switching of nanoparticles: a numerical study. *J. Magn. Magn. Mat.*, 272-276:E1237, 2004.
- Š. Višňovský, M. Nývlt, V. Prosser, R. Lopusník, R. Urban, J. Ferré, G. Pénisard, D. Renard, and R. Krishnan. Polar magneto-optics in simple ultrathin-magnetic-film structures. *Phys. Rev. B*, 52:1090, 1995.
- O Šipr, S. Bornemann, J. Minár, S. Polesya, V. Popescu, A. Šimůnek, and H. Ebert. Magnetic moments, exchange coupling, and crossover temperatures of Co clusters on Pt(111) and Au(111). *J. Phys.: Condens. Matter*, 19:096203, 2007.
- D.W. Wang, F. Tian, and J.G. Lu. Characterization of self-assembled alkanethiol monolayers using a low-current scanning tunneling microscope. *J. Vac. Sci. Technol., B*, 20:60, 2001.
- L.G. Wang, E.Y. Tsymbal, and S.S. Jaswal. First-principles study of adsorption of methanethiol on Co(0001). *Phys. Rev. B*, 70:075410, 2004.
- L.G. Wang, E.Y. Tsymbal, and S.S. Jaswal. Structural and magnetic properties of clean and methylthiolate-adsorbed Co(0001) surfaces: a first-principles study. *J. Magn. Magn. Mat.*, 286:119, 2005.
- B.L. Weeks, A. Noy, A.E. Miller, and J.J. De Yoreo. Effect of Dissolution Kinetics on Feature Size in Dip-Pen Nanolithography. *Phys. Rev. Lett.*, 88:255505, 2002.
- H. Wende, M. Bernien, J. Luo and C. Sorg, N. Ponpandian, J. Kurde, J. Miguel, M. Piantek, X. Xu, P. Eckhold, W. Kuch, K. Baberschke, P. M. Panchmatia and B. Sanyal, P. M. Oppeneer, and O. Eriksson. Substrate-induced magnetic ordering and switching of iron porphyrin molecules. *Nature Mater.*, 6:516, 2007.

- W. Wernsdorfer. Classical and quantum magnetization reversal studied in nanometer-sized particles and clusters. *arXiv:cond-mat/0101104v1*, 2001.
- W. Wernsdorfer, E.B. Orozco, K. Hasselbach, A. Benoit, B. Barbara, N. Demoncey, A. Loiseau, H. Pascard, and D. Mailly. Experimental Evidence of the Néel-Brown Model of Magnetization Reversal. *Phys. Rev. Lett.*, 78:1791, 1997.
- C.A. Widrig, C.A. Alves, and M.D. Porter. Scanning tunneling microscopy of ethanethiolate and *n*-octadecanethiolate monolayers spontaneously absorbed at gold surfaces. *J. Am. Chem. Soc.*, 113:2805, 1991.
- R. Wiesendanger, H.-J. Güntherodt, G. Güntherodt, R.J. Gambino, and R. Ruf. Observation of vacuum tunneling of spin-polarized electrons with the scanning tunneling microscope. *Phys. Rev. Lett.*, 65:247, 1990.
- S. Wirth, A. Anane, and S. von Molnár. Thermally activated magnetization reversal in nanometer-size iron particles. *Phys. Rev. B*, 63:012402, 2000.
- C. Wöll, S. Chiang, R.J. Wilson, and P.H. Lippel. Determination of atom positions at stacking-fault dislocations on Au(111) by scanning tunneling microscopy. *Phys. Rev. B*, 39:7988, 1989.
- Z.H. Xiong, D. Wu, Z.V. Vardeny, and J. Shi. Giant magnetoresistance in organic spin-valves. *Nature*, 427:821, 2004.
- Y. Ye, W. Sun, Y. Wang, X. Shao, X. Xu, F. Cheng, J. Li, and K. Wu. A Unified Model: Self-Assembly of Trimesic Acid on Gold. *J. Phys. Chem. C*, 111:10138, 2007.
- T. Yokoyama, S. Yokoyama, T. Kamikado, Y. Okuno, and S. Mashiko. Selective assembly on a surface supramolecular aggregates with controlled size and shape. *Nature*, 413:619, 2001.
- A.M. Zagoskin. *Quantum theory of many-body systems*. Springer, 1998.
- J. Zak, E.R. Moog, C. Liu, and S.D. Bader. Fundamental magneto-optics. *J. Appl. Phys.*, 68:4203, 1990.
- U. Zerweck, C. Loppacher, T. Otto, S. Grafström, and L.M. Eng. Accuracy and resolution limits of Kelvin probe force microscopy. *Phys. Rev. B*, 71:125424, 2005.
- A. Zhao, Q. Li, L. Chen, H. Xiang, W. Wang, S. Pan, B. Wang, X. Xiao, J. Yang, J. G. Hou, and Q. Zhu. Controlling the Kondo effect of an adsorbed magnetic ion through its chemical bonding. *Science*, 309:1542, 2005.

- S. Zou, D. Maspoch, Y. Wang, C.A. Mirkin, and G.C. Schatz. Rings of Single-Walled Carbon Nanotubes: Molecular-Template Directed Assembly and Monte Carlo Modeling. *Nano Lett.*, 7:276, 2007.

Publications

Related publications

- P. Campiglio, M. Campione, A. Sassella. Kelvin probe force microscopy characterization of self-assembled monolayers on metals deposited with dip-pen nanolithography. *J. Phys. Chem. C*, 113:8329, 2009.
- S. Rohart, P. Campiglio, V. Repain, Y. Nahas, C. Chacon, Y. Girard, J. Lagoute, A. Thiaville, S. Rousset. Spin-wave assisted thermal reversal of epitaxial perpendicular magnetic nanodots. *Phys. Rev. Lett.*, 104:137202, 2010.
- P. Campiglio, V. Repain, C. Chacon, O. Fruchart, J. Lagoute, Y. Girard, S. Rousset. Quasi unidimensional growth of Co nanostructures on a strained Au(111) surface. *Submitted to Surf. Sci.*

Other publications

- A. Papagni, P. Campiglio, M. Campione, P. Del Buttero, A. Mani L. Miozzo, E. Tonelli. Synthesis and physical properties of polyfluoro-acridines bearing perfluoroalkyl chains. *J. Fluor. Chem.*, 129:294, 2008.
- M. Campione, L. Raimondo, M. Moret, P. Campiglio, E. Fumagalli, A. Sassella. Organic-organic heteroepitaxy of semiconductor crystals: α -quaterthiophene on rubrene. *Chem. Mater.*, 21:4859, 2009.
- P. Campiglio, M. Campione, F. Canepa, C. Canevali, M.R. Cimberle, C. Fanciulli, L. Miozzo, M. Moret, A. Papagni, S. Rizzato, A. Sassella. Magnetic behaviour of polyfluoroacridine-based organic materials. *Eur. Phys. J. B*, 73:495, 2010.
- D. Mastromatteo, G. Macchi, P. Campiglio, A. Sassella, F. Meinardi. Novel organic paramagnetic nanofibers and nanostructures: A spectroscopic investigation. *Chem. Phys. Lett.*, 498:129, 2010.

Acknowledgments

If a thesis work is usually a long road, mine has been also a quite winding one. However, as often happens, this permitted me to get a more panoramic view, to approach different thematics and techniques and to learn a lot. Many people came along this road and made my work possible. Thus, I would like to thank them here.

First of all I owe my deepest gratitude to my supervisors: Adele Sassella in Milan, Sylvie Rousset and Vincent Repain in Paris. I am indebted to the Prof. Sassella for her unwavering presence and support even from afar and for leaving me the freedom to drive my experience along different paths. Equally, I am thankful to Sylvie for the confidence granted and for carefully following me despite her busy schedule. I am profoundly grateful to Vincent for his precious guide since I joined his team: all the discussions we had gave to my whole work consistency and a higher scientific caliber, showing me how to pass from close-ups to wide perspectives.

In Milan I was also fruitfully directed by Marcello, who helped me a lot to develop from zero Dip Pen Nanolithography. I could take advantage of his scientific and non-scientific support to solve all the problems along the way. I apologize for the undisciplined use of the AFM and for all the broken tips. I'm beholden also to Profs. Papagni and Moret who permitted me to use freely their laboratories and for the constructive discussions I have had with them, and with Prof. Borghesi who always followed my work. Moreover, I would like to thank Luisa for her help in the OMBE lab, where she was capable to infuse vivacity and also reduce noises and Luciano for some chemical incursions and for his benevolent advices. With Enrico I shared for a short period the use of AFM while with Suree and Fabrizio the office and nearly the desk, I owe them one for this. I'm always grateful to the GCS folks for remaining united even if we're spreading out across europe.

Acknowledgments

In Paris, I was lucky to work in the STM team, where the delightful ambience boosted my energies even during the longest series of experiments. In particular I would like to express my intense gratitude to Cyril for his daily assistance, for teaching me the ultimate experimental tricks (from the first transfer to the last furnace repaired) and for his friendly advices about everything else. Also, I would like to thank Jérôme for his everlasting presence in the lab, being always available to check the strange images and to find out hidden short-circuits. I'm indebted also with Yann for his encouragement and good humor as well with Yves and Jean.

I had the pleasure to work with Nicolas (especially for platinum capping, but not only), I enjoyed his passionate verbal rides and learnt from his scrupulous data analysis. Romain joined the team during the very first experiments about thiols capping and worked with me extensively on this subject, for this reason I'm beholden to him. The festive air breathed was also due to the eastern wind: that's why I want to express my sincere appreciation to Shruti and Hong, especially for bringing this pleasant breeze also outside the lab. For this same reason I'm glad to thank Carole, as well as for her genuine enthusiasm. Thanks also to Leo for his gentle and quite mood and to Maxence for his exuberant spirit and for reminding me that my French is sometimes incomprehensible. I would like to thank Cynthia, Nicolas and Philippe for keeping alive my chemical past. I had a lot of fun with all the thésards and post-doc MPQ (especially Ludivine, Pauline, Sebastian, Simon, David, Mernoush, Quentin, Romain, Erwan, Juan, etc.), from the mölkky on the terrace to the lab afterhours.

A relevant part of my work would not have been possible without some collaborations. I'm particularly grateful with Olivier who grew the gold sample with linear reconstruction and to Stanislas and André who simulated magnetization dynamics. Thanks to them my thesis has acquired originality and impact. The discussions with them were scientifically enriching but also enjoyable events. Finally, it is an honor for me to thank Prof. H. Brune for refereeing this manuscript and my work.

*Grazie a tutti
Merci à tous
Thanks to everyone*